ABSTRACT

BAEK, CHEOL MIN. Investigation of Top-Down Cracking Mechanisms Using the Viscoelastic Continuum Damage Finite Element Program. (Under the direction of Y. Richard Kim.)

This dissertation presents an advanced analysis tool for predicting top-down cracking (TDC) of hot-mix asphalt (HMA) pavements in a realistic manner. TDC is known to involve a complicated set of interactive mechanisms, perhaps more so than other HMA distresses. Such complexity makes it difficult to predict TDC reliably using conventional material models and analysis tools. Over the years, the viscoelastoplastic continuum damage (VEPCD) model has been improved to better understand and predict the behavior of asphalt concrete materials. The ability of the VEPCD model to accurately capture various critical phenomena has been demonstrated. For fatigue cracking evaluation of pavement structures, the viscoelastic damage (VECD) model has been incorporated into a finite element code as VECD-FEP++. To use this code in the prediction of TDC requires the enhancement and incorporation of additional sub-models to account for the effects of aging, healing, thermal stress, viscoplasticity and mode of loading. Although some of these models are not fully refined due to incomplete knowledge of the underlying physics of the process, placeholder models are incorporated into the framework so that they can be easily replaced when more fundamental approaches are identified. Within this VECD-FEP++ framework, a systematic parametric study is performed to identify the role of various mechanisms in TDC under certain specific conditions. Analysis using the enhanced VECD-FEP++ is found to capture some intuitive and important phenomena of TDC. Finally, to assess the capability of the

VECD-FEP++ framework, the Federal Highway Administration Accelerated Load Facility (FHWA ALF) pavements are simulated and the results is found to agree well with the measured field performance. After proper calibration, this tool could provide quantitative predictions of the extent and severity of TDC.

Investigation of Top-Down Cracking Mechanisms Using the Viscoelastic Continuum Damage Finite Element Program

by
Cheol Min Baek

A dissertation submitted to the Graduate Faculty of
North Carolina State University
in partial fulfillment of the
requirements for the Degree of
Doctor of Philosophy

Civil Engineering

Raleigh, North Carolina

2010

APPROVED BY:

Murthy N. Guddati	Roy H. Borden
S. Ranji Ranjithan	Y. Richard Kim Chair of Advisory Committee

DEDICATION

To my family

BIOGRAPHY

Cheol Min Baek was born on August 7, 1973 in Jeju, Korea, a beautiful island off the southern tip of the Korean peninsula. In March 1992, he was admitted to Kyunghee University in Korea to earn his B.S. and M.S. in Civil Engineering. After graduation he worked as an engineer at Dohwa Consulting Engineers Company for three years. In August of 2005 he then moved to North Carolina State University to pursue his Ph.D. degree in Civil Engineering.

ACKNOWLEDGEMENTS

First, I would like to express the deep appreciation to my advisor, Dr. Y. Richard Kim, for his guidance in preparing this dissertation and his precious advice and support throughout my graduate study. I would also like to thank Dr. Murthy N. Guddati for his valuable advice on the numerical work. My appreciation also goes to Dr. Roy H. Borden and Dr. S. Ranji Ranjithan for serving on my committee.

I was lucky to be able to associate myself with the talented and hard working colleague, Shane Underwood. I also wish to thank Senganal Thirunavukkarasu who is smart enough to correct my silly requests and implement into finite element code. I would also like to thank the past and present mates, Jusang Lee, Sangyum Lee, Jaejun Lee, Taeyoung Yun, Andrew Lacroix, Yeongtae Choi, Jeonghyuk Im, Hongjoon Park, Jongsub Lee and all other members in Dr. Kim’s research group. I am also thankful to my office mates, Fadi Jadoun and Diane Gilmore, for their kind words and smile.

Finally, I owe my sincere thanks to my family. Their encouragement, faith, and support made it possible for me to achieve this work. I also wish to express very special thanks to my wife, Yeohyun Yoon, and my daughter, Eunjae Baek. With them, every night and Saturday was the happy time that I could recover energy for the next day. I love you two forever.

TABLE OF CONTENTS

LIST OF TABLES

LIST OF FIGURES

1. INTRODUCTION

Top-down cracking (TDC) has been proven to be one of the major distresses in hot-mix asphalt (HMA) pavements in the United States. Many field studies have shown that different patterns of TDC exist, including cracks that start from the pavement surface and propagate downward, cracks that start as a top-down crack and propagate horizontally at the layer interface, and cracks that start from both the top and bottom simultaneously, forming a conjoined cracking pattern. The complex state of stress that exists in HMA pavements with various layer materials and thicknesses makes it difficult to determine the location of crack initiation and to predict crack propagation. For example, a crack may initiate at the bottom of the HMA layer, but changes in the state of stress during the propagation of that crack may result in the initiation and propagation of another crack at the top of the HMA layer. These complex mechanisms involved in crack initiation and propagation make it difficult to reliably predict the service life of HMA pavements using conventional HMA performance prediction models and pavement response models.

With the goal of accurate pavement performance evaluation, researchers at North Carolina State University (NCSU) have been developing advanced models for HMA under complex loading conditions. Over the past decade, they have successfully developed material models that can accurately capture various critical phenomena, such as: microcrack-induced damage, which is critical in fatigue modeling; strain rate-temperature interdependence; and viscoplastic flow, which is critical in high temperature modeling. The resulting single model is termed the viscoelastoplastic continuum damage (VEPCD) model.

To extend the strengths of the VEPCD model to the fatigue cracking evaluation of pavement systems, the viscoelastic continuum damage (VECD) model has been incorporated into the public domain finite element code, FEP++ (10). The resulting product, the so-called VECD-FEP++, allows the accurate evaluation of boundary condition effects (e.g., layer thickness) on the material behavior. In the VECD-FEP++, the damage is calculated for each element based on its state of stress, temperature, loading rate, and boundary conditions. Therefore, it is not necessary to assume a priori the location of distress initiation, nor the path of distress evolution. Not having to make such assumptions is a feature of the VECD-FEP++ that is essential in modeling TDC in various HMA pavements. The flexible nature of the VECD-FEP++ modeling technique allows cracks to initiate and propagate wherever the fundamental material law suggests. As a result, much more realistic and accurate cracking simulations can be accomplished using the VECD-FEP++.

The capability of the VECD-FEP++ to predict the performance of the pavement structure has been validated using different pavement structures. One example uses the Federal Highway Administration Accelerated Load Facility (FHWA ALF) pavements and another example is the Korea Express Highway (KEC) test road in South Korea (16). In the FHWA ALF research, twelve asphalt pavement lanes (that use various binders) were constructed at the FHWA Turner-Fairbanks Highway Research Center to rapidly collect data on pavement performance under conditions in which axle loading and climatic conditions are controlled. The KEC test road was constructed in December 2002 to serve as the basis for Korea's new pavement design guide, giving consideration to actual traffic loads and environmental changes. This test road is a 7.7 km two-lane highway consisting of 25 Portland cement concrete (PCC) pavement sections and 15 asphalt concrete (AC) pavement sections as well as three bridges and two geotechnical structures. The variables considered in the Korean study for AC pavements are surface layer type, base layer type, base layer thickness, and sublayer properties. Field performance surveys have been performed since the test road was constructed and will be continued. Predictions made using the VECD-FEP++ for the KEC test road sections demonstrate field performance trends and also reveal a generally positive relationship between model predictions and field observations for all the sections.

The primary objective of this research is to identify and/or develop mechanistic-based models for predicting TDC in HMA layers for use in mechanistic-empirical procedures for the design and analysis of new and rehabilitated flexible pavements. This research introduces the VECD-FEP++ as a means of accomplishing this objective. In an attempt to demonstrate the ability of the VECD-FEP++ to integrate the effects of variables that are important in TDC behavior, several sub-models are refined from existing models and incorporated into the VECD-FEP++. These models account for aging, healing, thermal stress, viscoplasticity and mode-of-loading. The Enhanced Integrated Climatic Model (EICM) is also integrated into the framework. It must be noted that these sub-models are incorporated into the VECD-FEP++ framework as place-holders only. Their accuracy needs to be verified and calibrated with further testing using various mixtures and in-depth analysis of the results. However, the reasonableness of the VECD-FEP++ with these sub-models is demonstrated using sensitivity analysis and a parametric study. After all, FHWA ALF pavements are simulated to evaluate the ability of the enhanced VECD-FEP++ for predicting the performance of actual pavements. The comparison of the predicted and measured performance is found to agree very well.

2. BACKGROUND OF TOP-DOWN CRACKING

TDC is a flexible pavement distress defined by cracks that begin at the surface of the AC layer and propagate downward with time. Recently, much effort has been devoted to better understanding this type of distress, but much work remains before the reasonable prediction of TDC is possible. In this section, a general background of TDC is given by reviewing the literature, which includes field observations, causes that are commonly considered, and various mechanisms.

2.1 : TOP-DOWN CRACKING FIELD OBSERVATIONS

Despite the many observations by different researchers, various locations of TDC, and the age of the pavement, no single characterization of TDC has been identified. For example, TDC may be found either within the wheel path or out of it, and it may be initiated at the pavement surface or some distance below the surface. Moreover, its time of initiation has been reported to be 1 to 5 years in Japan, 3 to 5 years in France, 3 to 8 years in the State of Washington, USA, 5 to 10 years in Florida, USA, and 10 years in the United Kingdom (8). However, many researchers consider that most TDC instances initiate at the edge of the wheel-path and pavement surface, and that the initiation and progression of TDC follow three stages (34):

- The first stage of TDC consists of a single, short, longitudinal crack that appears just outside the wheel-path;

- Over time, TDC grows into a second stage in which the longitudinal short cracks grow longer and sister cracks develop parallel to and within 0.3 to 1 m of the original crack;
- Finally, TDC evolves into a third stage in which the parallel longitudinal cracks are connected via short transverse TDC.

Figure 2-1 (a) shows pavement sections that exhibit the third stage of TDC, and (b) shows close-up top and side views of a core obtained from a conventional flexible pavement section.

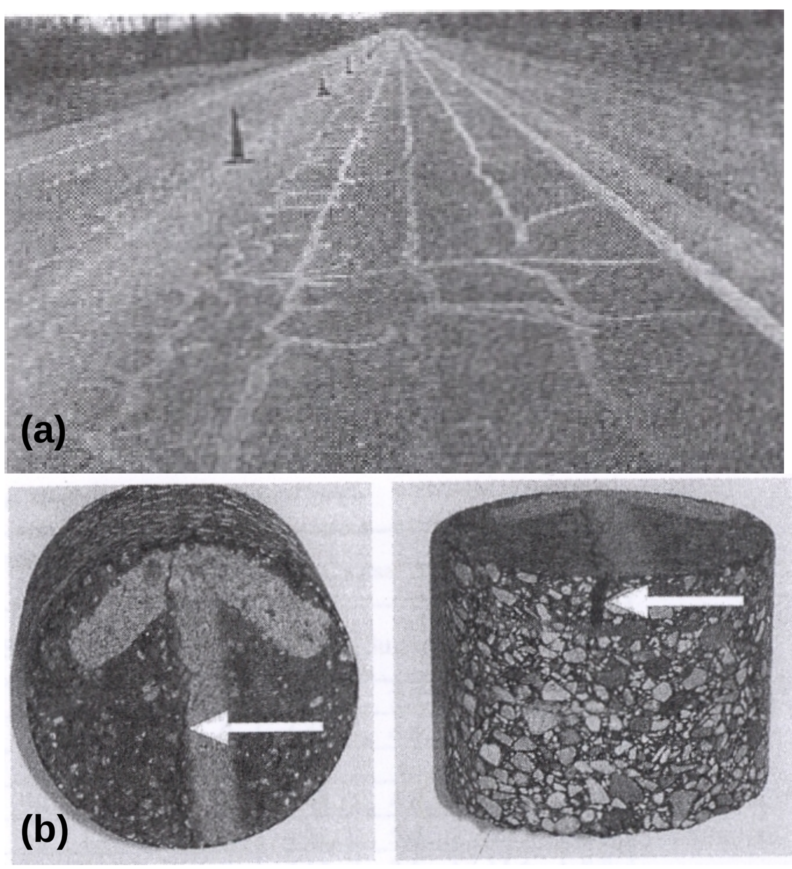

Figure 2-1. (a) The third stage of TDC; (b) a core obtained from a conventional flexible pavement section

Flexible composite pavements consist of an asphalt overlay layer over an existing concrete slab. According to field observations made by the Transport Research Foundation in the United Kingdom (24), reflection cracks initiate at the surface of the asphalt layer and propagate downwards, as shown in Figure 2-2. This observation is contrary to the general understanding that reflection cracks propagate upwards from an existing crack in the concrete. This field evidence also indicates that reflection cracks in as-laid composite roads are caused by thermally induced stresses rather than traffic induced stresses. The main factors that affect this behavior are:

- The thermal expansion coefficient of asphalt is much higher than that of concrete;
- Larger temperature changes occur in the asphalt layers;
- Age hardening causes the asphalt that is close to the surface to become the most brittle region of the asphalt layer.

Figure 2-2. Core from recently initiated reflection crack

Another uncommon field observation was made by Matsuno and Nishizawa (20) in Japan. They reported that cracks initiate at the pavement surface during the day when the asphalt is hot and relatively flexible. They also observed that cracks seldom form in the shadows under overpasses. They used mechanistic analysis to examine the effect of loads on various pavement structures and found that surface strain peaked for low stiffness at the edge of the tire.

2.2 : TOP-DOWN CRACKING MECHANISMS

So far, research in this field has focused mainly on stress analysis by applying different combinations of surface tractions and using the Finite Element Method (FEM) to identify causes that are most likely to induce tensile stress at the surface. Material heterogeneity was qualitatively recognized as a cause; however, no analytical and experimental methods have been developed to investigate how material heterogeneity would cause tensile stress and how significant the tensile stress would be (42). Recently, some researchers have tried to use alternative methods, such as micromechanics and doublet mechanics, to identify the TDC mechanisms that can account for the microstructure of the materials in more detail.

According to Matsuno and Nishizawa (20), high tensile contact stresses, generated on the road surface close to the tire edges, cause the appearance of small cracks. Before aging, some of these small cracks may disappear due to the kneading action of the tires and the healing effect that is inherent of asphalt, and while surface stiffness is low as a result of high temperatures. When the temperature decreases (daily or seasonally), the surface contracts and the remaining cracks set, thus becoming TDC. TDC progression relies on traffic stress distribution inside the pavement, which is significantly important at the crack tips when the temperature is high or the stiffness is low.

Some laboratory tests conducted by several researchers indicate that only a combination of high dissipation energy at the surface, shear stresses, temperature induced stresses and residual stresses could cause cracking at the surface. The latest studies indicate that the construction quality regarding gradation, segregation, compaction, and mixture spreading contributes considerably to the initiation of TDC (8).

According to the study by Myers (22), cracks propagate perpendicular to principal stresses. For short cracks, propagation is driven purely by tension, and such cracks progress straight down into the pavement. At intermediate depths, cracks change direction, because the state of stress in the asphalt layer changes with depth. Progression speed depends on crack length, asphalt layer thickness and grading. It increases with pavement thickness and with coarse grading.

On the other hand, Nesnas and Nunn (24) argue that crack propagation of surface cracks occur mainly in shear mode. Yielding due to shear stresses (with all principal stresses being compressive, although not of equal magnitude) could result in shearing cracks (yield planes), as a consequence of the introduction of secondary tensile stresses.

2.2.1 : The Causes of Top-Down Cracking

The main TDC mechanisms are the critical stresses and strains (tensile and shear) induced at the top of the pavement structure that stem from a combination of many factors, which are discussed in the following.

Critical stresses may result (43):

- at or near the pavement surface due to contact stresses between the tire and the pavement surface; if the stress exceeds the local tensile strength, it will provoke wheel path cracking;
- from a sudden change in the asphalt layer temperature gradient (especially at very low temperatures and extreme cooling rates where stress relaxation and material healing are significantly reduced at the same time); such change results in thermal shrinkage and provokes transversal cracks;
- from traffic loading at low temperatures when traffic-induced stresses are superposed by thermal stresses; thus, combined stresses may provoke early longitudinal cracking outside the wheel path at a distance between 400 and 900 mm from the load axis, with increased distance if the temperature decreases;
- from material-related factors, such as asphalt aging and particle segregation due to stripping of the binder;
- from early construction microcracks that are induced by the asphalt roller.

Six main factors have been reported to contribute to TDC initiation and propagation (9):

- Climatic conditions (e.g., temperature);
- Traffic conditions, including the load and inflation pressure of truck tires;
- Aging of the binder;
- Structural conditions, including layer thickness;
- Mixture properties, including binder type and aggregate gradation; and
- Construction quality, including segregation and compaction procedures.

The following subsections navigate the ways that each factor affects the initiation and propagation of TDC, and the interactions of each factor.

2.2.1.1 : Temperature

It is generally understood that TDC and rutting are not related to each other. Whereas TDC is related to low temperature, rutting is related to high temperature. Freitas et al. (9) conducted a laboratory test using a wheel-tracking device with 17 AC slabs at three temperatures (30°C, 40°C, and 50°C). It was observed that the number of wheel passes corresponding to the first crack decreased substantially with an increase in temperature. It should be noted, however, that this device does not realistically replicate the horizontal contact stresses applied by tires at the surface of a pavement. Furthermore, the laboratory testing results were supported by numerical simulation using a 3-D nonlinear viscoelastic finite element model. From this numerical simulation, normal stresses were found to be predictably similar for the three temperatures simulated, whereas shear stresses appeared to increase with temperature, and at 50°C shear stresses appeared to exceed normal stresses in the vicinity of the load.

Such results correspond to the conclusions drawn by Wang et al. (42) who utilized the micromechanics approach, which can account for the microstructure of the materials in more detail. From laboratory testing with beam specimens subjected to repeated loads at various temperatures, and from image analyses of the cut section, Wang et al. concluded that:

- TDC may not necessarily initiate only at the pavement surface. It may also initiate at some distance below the surface;

- Both tensile and shear cracking could initiate TDC;
- TDC most likely initiates when the mastic is weak or the pavement temperature is high, due to increased shear stress. These cracks may open up or propagate during other seasons and after additional loading cycles. Therefore, a mix that is sensitive to rutting may also be sensitive to cracking.

2.2.1.2 : Asphalt Aging

The hardening of asphalt after it has been subjected to heat or to the environment is referred to as aging. The three major contributors to asphalt aging are:

- Loss of oily components by volatility or adsorption;
- Changes in composition by reaction with atmospheric oxygen; and
- Molecular structuring that produces the steric hardening.

Aging affects the asphalt binder properties and typically occurs in two phases, short and long term. Short-term aging occurs as a loss of volatile components and oxidation in the binder during the mixing and placement of the AC. Long-term aging occurs as progressive oxidation of the asphalt binder after placement. It has been observed that aging increases the stiffness and brittleness of the binder with a corresponding effect on the AC mix. Because of increased exposure of the surface course to sunlight and oxygen, long-term aging mainly affects the AC surface course, whereas the lower courses may not be affected.

The aging of certain asphalts is strongly mitigated by some aggregates, but not by others. The extent of mitigation appears to be related to the strength of the chemical bonding (adhesion) between the asphalt and aggregate (3).

2.2.1.3 : Pavement Structure

The typical understanding of TDC is that it occurs mainly in thick AC pavement, which is a viewpoint supported by many research efforts. Uhlmeyer et al. (41) observed that TDC in Washington State occurs in and around the wheel paths in pavements 3 to 8 years old with AC thicknesses of more than 16 cm from the field. Hence, they concluded that pavement thickness has an effect on the initiation of TDC. On the other hand, Matsuno and Nishizawa (20) and Meyers et al. (21) concluded, also from field observations, that pavement structure has little effect on the surface tensile stress and strains.

2.2.1.4 : Segregation

According to Schorsch et al. (32), segregation typically occurs in two forms, temperature segregation and particle segregation. Both are specific to the manufacturing and placement of the asphalt. Temperature segregation occurs when the asphalt leaves the paver at a non-uniform temperature. Because asphalt cement is a temperature susceptible material that exhibits different engineering characteristics at different temperatures, a non-uniform temperature distribution can result in non-uniform compaction of the asphalt.

Particle segregation occurs when the coarse and fine aggregates are not uniformly distributed throughout the mix. Particle segregation may occur at any time during the mixing, transportation and construction operations. Various researchers have correlated the effects of segregation to underperformance of asphalt pavements. Brown et al. (4), in an investigation of segregation of asphalt mixtures in Georgia, showed that the tensile strength of the mixtures decreases with an increasing proportion of coarse particles. Thus, it can be seen that both temperature and particle segregation contribute to the shorter fatigue life and a high susceptibility to age hardening. Figure 2-3 shows a photograph of a site exhibiting TDC, with the cracks in the segregated areas.

Figure 2-3. TDC in segregated area

2.2.2 : Summary of Top-down Cracking Mechanisms

Based on the literature review, the flow chart of TDC mechanism is developed as shown in Figure 2-4. Repeated mechanical loading produces the tensile stress and shear stress, and repeated thermal loading produces the tensile stress at pavement surface. These stresses result in the damage in pavement and the damage is affected by a combination of healing and aging mechanisms. Such damage is accumulated with the time and then if the accumulated damage exceeds the strength of the material, the crack initiates at the surface of pavement. Occasionally, the significant tensile stress developed by acute temperature decrease or the significant shear stress by rutting at high temperature could result in the early crack initiation. Once crack is developed, the shear stress near the crack is increased and the crack propagates throughout the asphalt layers.

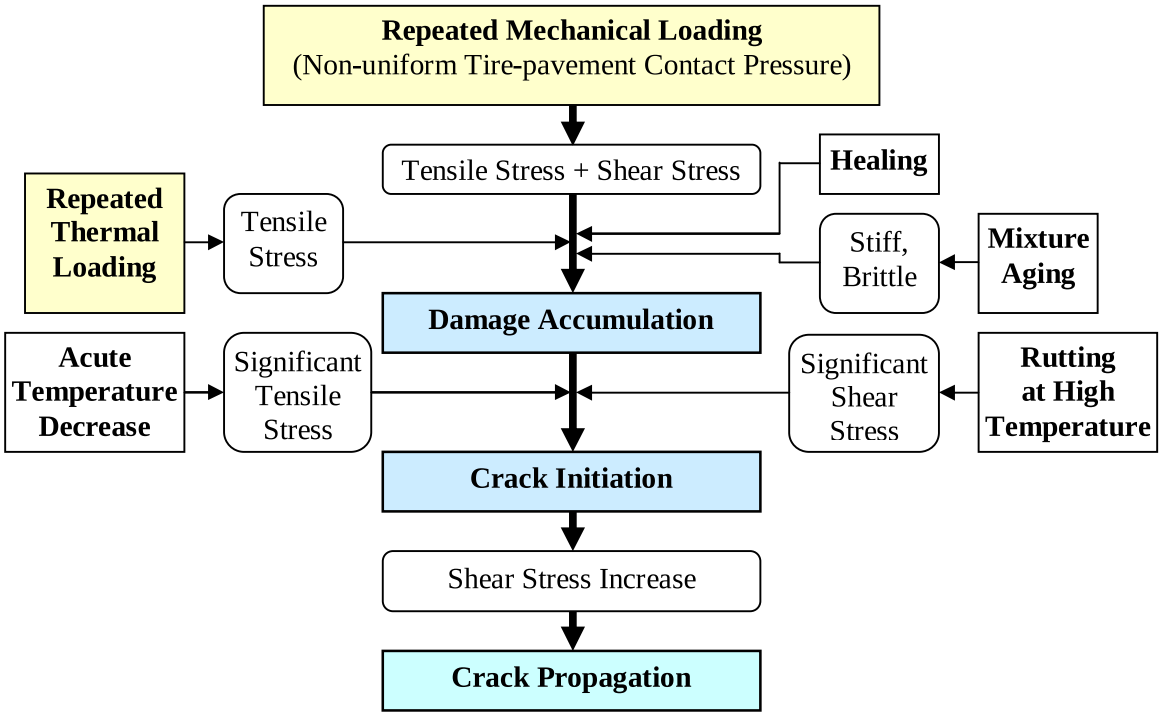

Figure 2-4. Flow chart of top-down cracking mechanisms

3. FRAMEWORK

The overall framework guiding the VECD-FEP++ analysis is shown in Figure 3-1. The analysis is divided into five sub-modules: the input module, the material properties sub-models, the analytical sub-models, the performance prediction module and the output module. These modules provide an analytical/computational method for identifying the location and time of crack initiation in the pavement structure. Each sub-model requires specific parameters to be obtained and/or determined. Table 3-1 summarizes the inputs for the VECD-FEP++ model along with the quantity of interest and test method for each input. A detailed description of the laboratory specimen fabrication and test method is given in Section 3.2.1.

Table 3-1. Inputs Required for the VECD-FEP++ Model

Input	Quantity of Interest	Test Method
LVE	Material coefficients (E_∞ , E_i , r_i)	Temperature/frequency sweep test
VECD	Material coefficients (a , b)	Monotonic direct tension test at 5°C, Constant crosshead cyclic test at 19°C
Aging	LVE and VECD with time	Same as above and long-term oven aging
Failure Criteria	Critical pseudo stiffness	Constant crosshead cyclic test
Healing	Change in pseudo stiffness with rest duration	Random loading and healing period cyclic tests
Viscoplasticity	Material coefficients (p , q , Y)	Monotonic direct tension test at 40°C
Thermal	Thermal expansion coefficient	Thermal expansion test, or from literature
EICM	Temperature distribution within a pavement structure	-
Structural Aging	Effective age of pavement materials with depth	Binder viscosity or $\lvert G^* \rvert$ (A and VTS)
Damage Factor	Viscoplastic sensitivity	-
Traffic	Number of Equivalent Single Axle Loads (ESAL count)	-
Extrapolation	Number of analysis segments	-

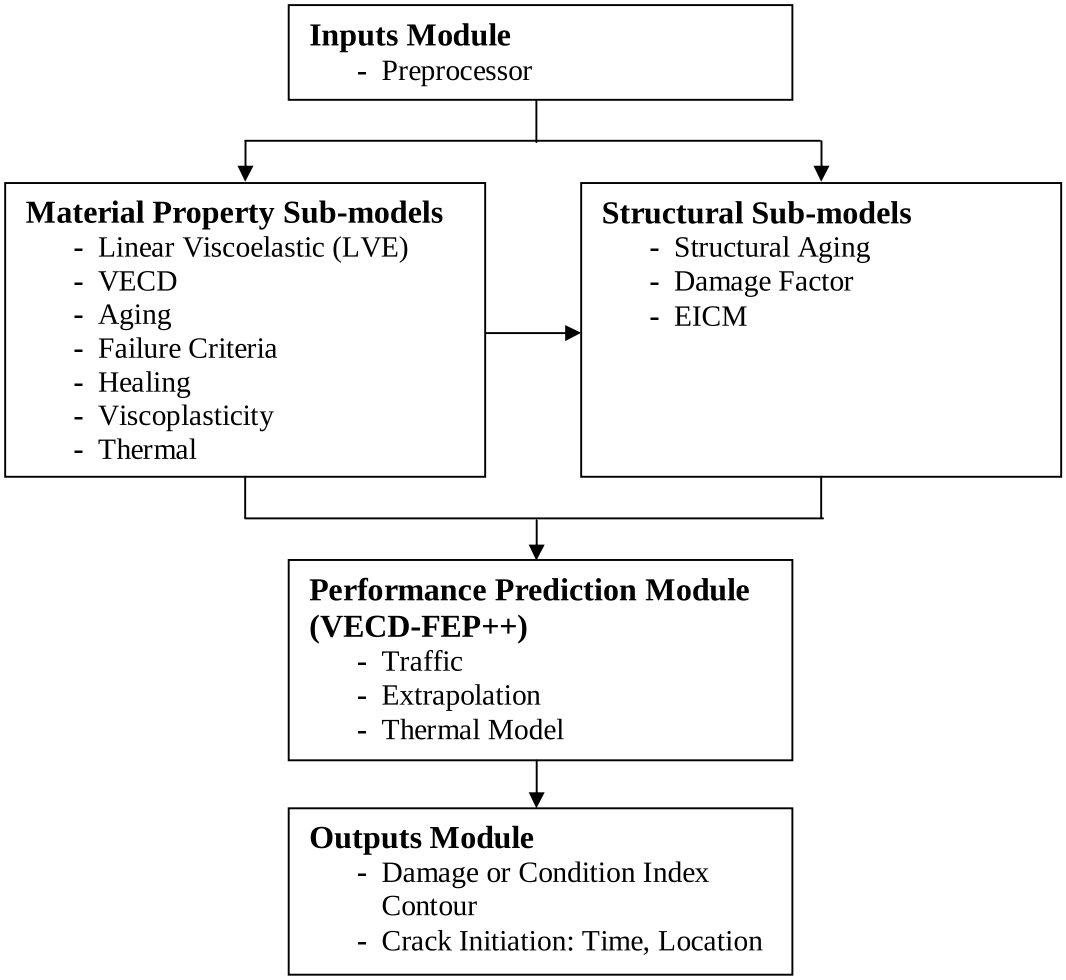

Figure 3-1. VECD-FEP++ model framework

3.1 : INPUTS MODULE

Preprocessors have been developed to facilitate easy and rapid analysis of pavement systems using the FEP++. Specifically, the preprocessor helps in the rapid development of input models for analysis and also helps in making consistent changes for repeated analysis. This tool is ANSI-compliant and developed with portable libraries, thus making it easy to transfer to other platforms.

The preprocessor provides:

- Graphical forms for user input;
- Pavement loading with support for multiple moving loads;
    - Material data with support for elastic, viscoelastic, and viscoelastic continuum damage (VECD) models; and
    - Analysis parameters and finite element (FE) mesh customization;
- Pavement temperature profiles generated from the EICM;
- Data validation and consistency checks;
- Visualization of the finite element model (FEM), consisting of:
    - Graphical view of the model and mesh;
    - Standard graphical operations, such as zoom, pan, rotate, etc.; and
    - Mesh information, such as node and cell numbers;
- Data persistence using a database for storing and retrieving input data; and
- One-click installer and user documentation.

3.2 : MATERIAL PROPERTY SUB-MODELS

3.2.1 : Laboratory Specimen Fabrication and Test Method

All specimens were compacted by the Servopac Superpave gyratory compactor, manufactured by IPC Global of Australia, to dimensions of 178 mm in height and 150 mm in diameter. To obtain specimens of uniform quality for testing, these samples were cored and cut to a height of 150 mm and a diameter of 75 mm.

After obtaining specimens of the appropriate dimensions, air void measurements were taken via the Core-Lok method, and specimens were stored until testing. It is noted that the air voids for all tests in this research are between 3.5% and 4.5%. During storage, specimens were sealed in bags and placed in an unlit cabinet to reduce the aging effects. Further, no test specimens were stored for longer than two weeks before testing.

Prior to all testing, the steel end plates were glued to the specimen using DEVCON steel putty. Extreme care was taken to completely clean both the end plates and the specimen ends before each application to prevent failure at the glued area. To ensure the specimens were properly aligned, a special gluing jig was employed so that the end plates were parallel, thus minimizing any eccentricity that might occur during the test.

Measurements of axial deformations were taken during testing at 90° intervals over the middle 100 mm of the specimen using loose-core linear variable displacement transducers (LVDTs). Load, crosshead movement and specimen deformation data were acquired using a 16-bit National Instruments data acquisition board and collected using LabVIEW software. The data acquisition rate varied depending on the nature of the test so that the appropriate amount of data could be acquired for analysis. A MTS closed-loop servo-hydraulic loading frame was used for all the tests. Depending on the nature of the test, either an 8.9 kN or 22 kN load cell was used. An environmental chamber, equipped with liquid nitrogen coolant and a feedback system, was used to control and maintain the test temperature. Figure 3-2 shows the gluing jig for the tension specimen and the MTS machine.

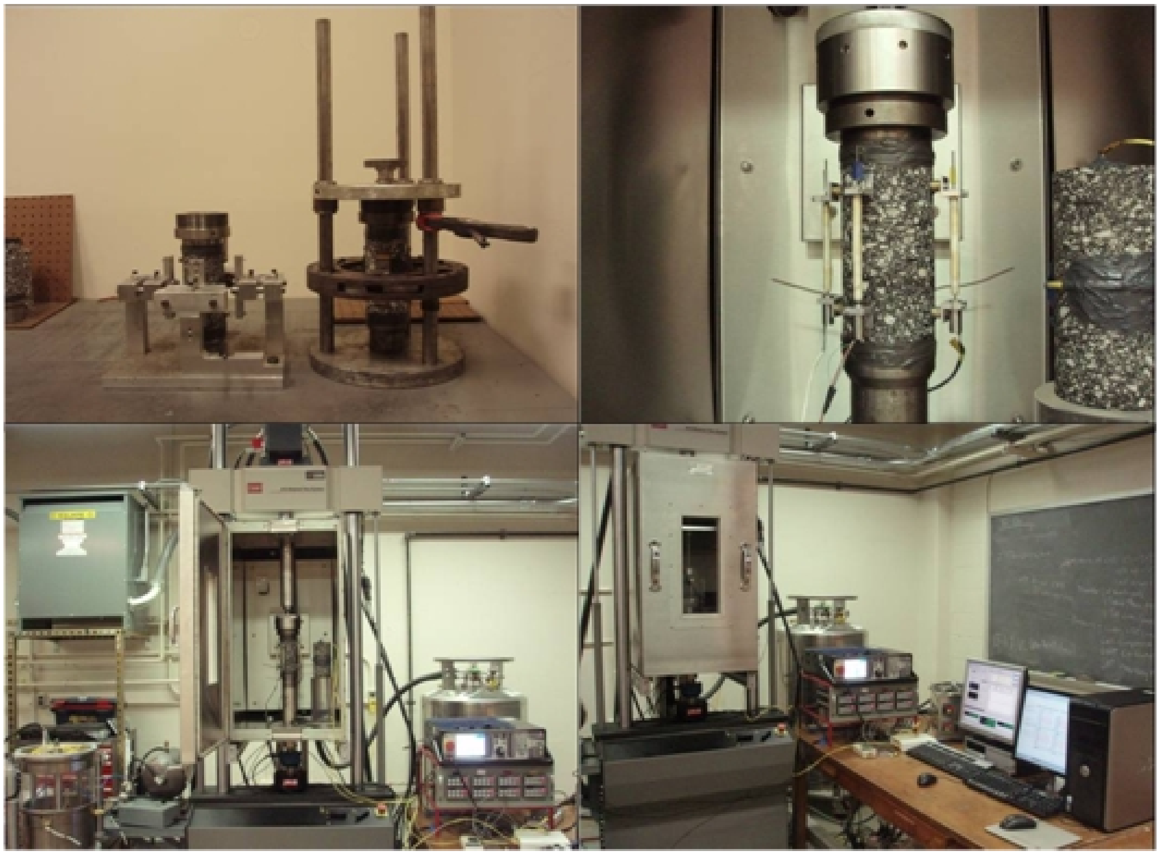

Figure 3-2. Gluing jig and MTS machine

Three different types of laboratory testing were performed for the aging study: the complex modulus test, constant crosshead rate test, and cyclic fatigue test. The complex modulus test and constant crosshead rate test were carried out with the aim of capturing the aging effects in the current VECD model. For a more direct investigation of aging effects, cyclic fatigue tests were performed in controlled crosshead (CX) and controlled stress (CS) modes.

The complex modulus test was performed in stress-controlled uniaxial tension-compression mode. The test was performed at frequencies of 25, 10, 5, 1, 0.5, and 0.1 Hz and temperatures of -10°, 5°, 20°, 40°, and 54°C. The load level was adjusted for each condition to produce total strain amplitudes of about 50 to 75 microstrains, which is in the linear viscoelastic (LVE) range. The constant crosshead rate test was conducted in uniaxial tension mode at different on-specimen LVDT strain rates at both 5°C and 40°C until failure. Instead of testing several replicates at a limited set of rates and temperatures, tests were conducted at three different rates with one replicate per rate.

Both types of cyclic fatigue tests, CX and CS, were conducted only in tension mode with a haversine loading at a fixed level. Because a true controlled strain test using cylindrical specimens is difficult to run and can damage equipment if improperly performed, the CX test was utilized. Such a test results in a mixed mode of loading that is neither controlled stress nor controlled strain.

3.2.2 : Linear Viscoelastic (LVE) Model

3.2.2.1 : Linear Viscoelasticity

Viscoelastic materials exhibit time and temperature dependence, meaning that the material response is not only a function of the current input, but the entire input history. By contrast, the response of an elastic material is dependent only on the current input. For the uniaxial loading considered in this research, the non-aging, LVE constitutive relationships are expressed in the convolution integral form, as shown in Equations (3-1) and (3-2):

$$s = \int_0^t E(t-t)\frac{de}{dt}dt \quad \text{and} \qquad (3\text{-}1)$$

$$e = \int_0^t D(t-t)\frac{ds}{dt}dt \ , \tag{3-2}$$

where $E(t)$ and $D(t)$ are the relaxation modulus and creep compliance, respectively (the t term is the integration variable). The relaxation modulus and creep compliance are important material properties, along with the complex modulus, in LVE theory. Because these two properties are the responses for respective unit inputs, they are called unit response functions. These unit response functions can be obtained either by experimental tests performed in the LVE range or by converting another unit response function, as suggested by Park and Schapery (25).

3.2.2.2 : Unit Response Functions and Their Interrelationships

The unit response functions presented in Equations (3-1) and (3-2) are often measured in the frequency domain via the complex modulus test, because it is often difficult to obtain unit response functions in the time domain due to the limitations of the machine capacity or testing time. The complex modulus provides the constitutive relationship between the stress and strain of a material loaded in a steady-state sinusoidal manner, e.g., in the frequency domain. The storage modulus can be determined from the complex modulus and it can be converted to a time-dependent property, such as $E(t)$ and $D(t)$, through LVE theory. When the storage modulus is expressed in terms of reduced angular frequency, w_R, as shown in Equation (3-3), it can be expressed using the Prony series representation given in Equation (3-4) (25, 29).

$$E'(w_R) = \left|E^*(w_R)\right| * \sin\left(f\left(w_R\right)\right) \text{ and} \tag{3-3}$$

$$E'(w_R) = E_\infty + \sum_{i=1}^{m} \frac{{w_R}^2 r_i E_i}{{w_R}^2 {r_i}^2 + 1}, \tag{3-4}$$

where

E_∞ = the elastic modulus,
w_R = the angular frequency ($= 2p\ f_R \Delta t$),
Δt = the time lag between the stress and strain,
E_i = the modulus of the i^th Maxwell element (fitting coefficient), and
r_i = the relaxation time (fitting coefficient).

The coefficients determined from this process are then used with Equation (3-5) to find the relaxation modulus.

$$E(t) = E_\infty + \sum_{i=1}^{m} E_i e^{-t/r_i} \tag{3-5}$$

Using the theory of viscoelasticity, the exact relationship between the creep compliance and the relaxation modulus is given by Equation (3-6).

$$\int_0^t E(t-t)\frac{dD(t)}{dt}\,dt = 1 \tag{3-6}$$

If the creep compliance can be written in terms of the Prony representation (Equation (3-7)), substituted into Equation (3-6) along with Equation (3-5) and simplified, the result can be expressed as a linear algebraic equation, Equation (3-8). The coefficients, $\{D\}$ in this equation, are solved by any proper numerical method.

$$D(t) = D_g + \sum_{j=1}^{n} D_j\left(1 - e^{-t/t_j}\right) \text{ and} \tag{3-7}$$

$$[A]\{D\}=[B], \tag{3-8}$$

where

$$[A]=\sum_{j=1}^{M}\left[\sum_{m=1}^{N}\frac{r_m E_m}{r_m - t_j}\left(e^{\frac{-t}{r_m}}-e^{\frac{-t}{t_j}}\right)+E_{\infty}\left(1-e^{-\frac{t}{t_j}}\right)\right];$$

$\{D\}=D_j$; and

$$[B]=1-\frac{1}{E_{\infty}+\sum_{m=1}^{N}E_m}\left(E_{\infty}+\sum_{m=1}^{N}E_m e^{\frac{-t}{r_m}}\right).$$

Once the coefficients, D_j, are determined, they are substituted into Equation (3-7) to find the creep compliance.

3.2.2.3 : Time-Temperature Superposition Principle for Linear Viscoelastic Material

The effects of time and temperature on viscoelastic material behavior can be combined into a single parameter, called *reduced time*, through the time-temperature superposition principle. Viscoelastic properties obtained in the LVE range at different temperatures can be superposed to develop a single mastercurve by shifting them horizontally to a certain reference temperature. The horizontal distance required to superpose a curve to a reference curve in logarithmic space is the log of the time-temperature shift factor (a_T). A material that exhibits a single mastercurve by this method is called *thermorheologically simple*. Equation (3-9) represents the general mathematical definition of reduced time.

$$x(t) = \int_0^t \frac{1}{a_T(t)} dt \quad , \tag{3-9}$$

where

a_T = the time-temperature shift factor.

When the temperature is constant, for example in a relaxation modulus experiment, Equation (3-9) simplifies to the more common form shown in Equation (3-10). For frequency domain conditions, such as when measurements are taken in a dynamic modulus test, the reduced frequency is similarly computed using Equation (3-11).

$$x = \frac{t}{a_T} \tag{3-10}$$

$$f_{red} = f * a_T \tag{3-11}$$

3.2.3 : Viscoelastic Continuum Damage Model (VECD)

3.2.3.1 : Continuum Damage

On the simplest level, continuum damage mechanics considers a damaged body with some stiffness as an undamaged body with a reduced stiffness. Continuum damage theories thus attempt to quantify two values: damage and effective stiffness. Further, these theories ignore specific microscale behaviors and, instead, characterize a material using macroscale observations, i.e., the net effect of microstructural changes on observable properties. In the macroscale, the most convenient method to assess the effective stiffness is to use the instantaneous secant modulus. As discussed in the subsequent sections, direct use of the stress-strain secant modulus in asphalt concrete (AC) is complicated by time dependence.

Damage is oftentimes more difficult to quantify and generally relies on macroscale measurements combined with rigorous theoretical considerations. For the VECD model, Schapery's work potential theory, which is based on thermodynamic principles, is appropriate for the purpose of quantifying damage. Within Schapery's theory, damage is quantified by an internal state variable (S) that accounts for microstructural changes in the material.

3.2.3.2 : Correspondence Principle

The correspondence principle states that viscoelastic problems can be solved with elastic solutions when physical strain is replaced by pseudo strain.

$$e^{R} = \frac{1}{E_R}\int_{0}^{t} E\left(t-t\right)\frac{de}{dt}\,dt \ , \tag{3-12}$$

where E_R is a particular reference modulus included for dimensional compatibility and typically taken as one. Using pseudo strain in place of physical strain, the constitutive relationship presented in Equation (3-1) can be rewritten as

$$s = E_R e^{R} . \tag{3-13}$$

It is seen from Equation (3-13) that a form corresponding to that of a linear elastic material (Hooke's Law) is used when strain is replaced by pseudo strain. In a practical sense, pseudo strain is simply the LVE stress response to a particular strain input. The most important effect of pseudo strain is seen when plotting stress, because any time effects are removed from the resulting graph. This property of the stress-pseudo strain relationship is used in the modeling approach presented here.

The basic consideration of the continuum damage theory is that any reduction in stiffness is related to damage. Graphically, this phenomenon is seen in a reduction of the stress-strain modulus; recall that continuum damage theories typically use a secant modulus to quantify the effect of damage. For viscoelastic materials, a reduction in the secant modulus is also related to the time effects. However, in stress-pseudo strain space the time effects are removed, and any reduction in the pseudo secant modulus (the secant modulus in the stress-pseudo strain space) is a direct consequence of damage.

3.2.3.3 : Viscoelastic Continuum Damage Theory

Continuum damage theory states that the stiffness reduction is defined by the pseudo secant modulus (pseudo stiffness). This quantity is typically normalized for specimen-to-specimen variability by the factor, I , and denoted as C (Equation (3-14)).

$$C = \frac{s}{e^{R} \times I} \tag{3-14}$$

The LVE relationship represented by the pseudo strain in Equation (3-13) can be modified to Equation (3-15) when the microcracking damage grows (30). Then, by substituting Equation (3-15) into Equation (3-2), the nonlinear constitutive relationship for strain is given in Equation (3-16).

$$s = C(S)e^{R} \tag{3-15}$$

$$e_{ve} = E_R \int_{0}^{t} D(t-t) \frac{d\left(\frac{s}{C(S)}\right)}{dt} dt \tag{3-16}$$

Equations (3-15) and (3-16) require the determination of an internal state variable, S. This internal state variable quantifies any microstructural changes that result in observed stiffness reduction. The relationship between damage (S) and the normalized pseudo secant modulus (C) is known as the damage characteristic relationship and is a material property that is independent of loading conditions.

3.2.4 : Aging Model

The effect of aging in asphalt binders on the performance of asphalt-aggregate mixtures is well recognized. Traditionally, the effects of binder aging on mixture performance have been investigated using two approaches. The first is to subject different asphalt binders to various aging conditions and measure the resultant changes in physical properties to assess the aging potential of the different binders. However, this approach does not account for the effect of aggregate particles and does not yield accurate and realistic information about the performance of the mixtures. The other approach is to subject the asphalt-aggregate mixtures to various aging conditions and then measure the physical properties of the aged mixtures. Although this method is more realistic because the aging process is conducted directly on the mixtures, little work has been done to determine the best method for incorporating these changes in mixture properties due to aging into the framework of constitutive modeling or fatigue performance modeling (7).

The original VECD uniaxial constitutive model is based on the assumption that the material is a non-aging system. This study focuses on establishing an analytical/experimental methodology for incorporating the effects of aging in the current constitutive model.

3.2.4.1 : Aging Method for Laboratory Mixtures

The NCHRP 9-23 project has found that the Strategic Highway Research Program (SHRP) protocol is not sufficient to simulate field-aging behavior in the laboratory because of its inability to account for variables such as field-aging conditions and mix properties (27). Nevertheless, the SHRP method has some advantages to be considered for this study: 1) it is simple to implement; 2) it provides a general relationship between laboratory and field-aging behavior; and 3) it has been used successfully for previous studies conducted at NCSU (7). In addition, because this part of the study focuses on developing a place-holder relationship for the aging effects in the current VECD model rather than on matching the laboratory aging to that of the field, it was decided to use the SHRP aging method in this study. Four levels of asphalt mixture aging were simulated, as follows (3):

- Short-term aging (STA): The loose, uncompacted mixture is conditioned at 135°C for 4 hours and then compacted. Specimens are cored and cut for testing.
- Long-term aging, Level 1 (LTA1): The aging procedure is the same as for STA, except the specimens are conditioned at 85°C for 2 days before testing after coring and cutting.
- Long-term aging, Level 2 (LTA2): The aging procedure is the same as for STA, except the specimens are conditioned at 85°C for 4 days before testing after coring and cutting.

- Long-term aging, Level 3 (LTA3): The aging procedure is the same as for STA, except the specimens are conditioned at 85°C for 8 days before testing after coring and cutting.

These aging processes for asphalt mixtures follow the AASHTO R30 specification (2), with the exception that three different long-term aging times are used. To minimize slump in the specimens during the oven aging procedure, the method suggested by the NCHRP 9-23 project (13) was adopted whereby the specimens are wrapped in wire mesh, and the mesh is held in place by three steel clamps. All specimens were measured according to diameter, height, weight, and air void percentage before and after oven aging. The differences in the dimensions are negligible; the dry weights were reduced by 0 to 0.5 g, and the air voids (%) increased by 0 to 0.5%, depending on the level of aging. It is noted that the maximum specific gravity (G_{mm}) value may also change with aging; however, a single G_{mm} value for the STA mixture was used for all the aged specimens. Therefore, it was concluded that there was no apparent damage due to aging.

3.2.4.2 : Materials for Laboratory Testing

Two different mixtures were used for the aging study. The first mix, the A mix, is one of the most common mixture types used in North Carolina. The granite aggregate was obtained from the Martin-Marietta quarry in Garner, NC, and the aggregate structure is a fine 9.5 mm nominal maximum aggregate size (NMAS) mixture comprised of 36% #78M stone, 25% dry screenings, 38% washed screenings, and 1% baghouse fines. The blended gradation is shown in Figure 3-3. An unmodified asphalt binder (PG 64-22) from Citgo in

Wilmington, NC was also used for this study. The asphalt content for the A mix is 5.7% by weight of the total mix.

After a series of laboratory tests, the results of which are shown below, it was determined that this mix was insensitive to aging and thus did not meet the study goals. A trend was found between the VECD characterization parameters and the aging times, but the strength of this trend was weak. As a result, a second mix, designated as the AL mix, was selected because it was known to be prone to aging.

This second mix, the AL mix, consisted of AAD-1 asphalt binder and local limestone aggregate. The AAD-1 binder (PG 58-28) was obtained from the Materials Reference Library (MRL), and the local limestone aggregate was obtained from the Martin-Marietta Castle Hayne quarry. The aggregate structure is a fine 9.5 mm Superpave mixture comprised of 50% # 78M stone, 33% 2S-sand, 14.5% dry screenings, and 2.5% baghouse fines. The blended gradation is shown in Figure 3-3. A Superpave mix design procedure was performed, and an optimal asphalt content of 6.2% by weight of total mix was chosen. The mixing temperature and compaction temperature used for the study are 147°C and 135°C, respectively.

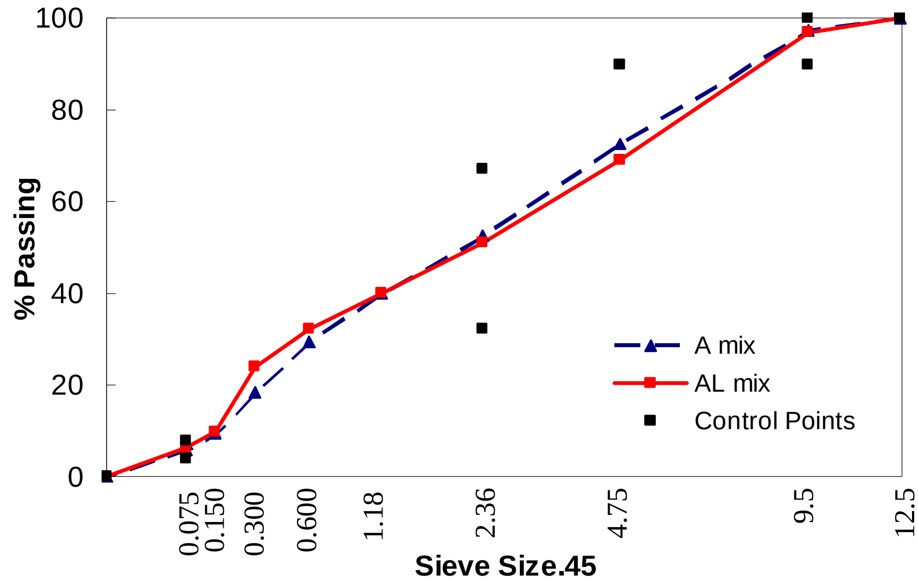

Figure 3-3. Mixture gradation chart

3.2.4.3 : VECD Characterization of Aged Mixtures

<u>The A Mix</u>

The material characteristics of primary importance in VECD modeling are the LVE and damage characteristics. Figure 3-4 (a) and (b) present the replicate averaged dynamic modulus ($|E^*|$) master curves for four different aging levels of the A mix in both semi-log and log-log scales. It is observed that, in general, the stiffness increases with aging time, but that the stiffness increases are small. This finding suggests that the short-time aging kinetics are more active than the long-time aging kinetics. It is also observed from Figure 3-4 (a) and (b) that the STA mixture exhibits similar stiffness characteristics at higher reduced frequencies (physically representing cooler temperatures and/or faster loading frequencies) than the LTA mixtures, but deviates from the LTA mixtures at approximately 1 Hz. Below this reduced frequency, the STA mixture shows lower modulus values than the LTA mixtures. Such a trend is expected because it is known that as temperature increases or frequency reduces that the modulus gradient between the asphalt binder and aggregate particles becomes larger. As a result, the effect of the asphalt binder properties on the total mixture behavior may become more noticeable. Similar trends can also be seen in the phase angle master curve graph, shown in Figure 3-5; that is, the three LTA mixtures exhibit similar phase angle values for all frequencies, but the STA mixture shows a different phase angle in the lower frequency range.

With regard to the damage characteristics, Figure 3-6 indicates that the LTA3 mixture exhibits the most favorable damage characteristic curve, followed next by the LTA2 and LTA1 mixtures and, finally, by the STA mixture. The differences among the aged mixtures are not significant, and cannot be used directly to assess fatigue performance, because Figure 3-6 does not account for stiffness effects, boundary conditions, or failure characteristics.

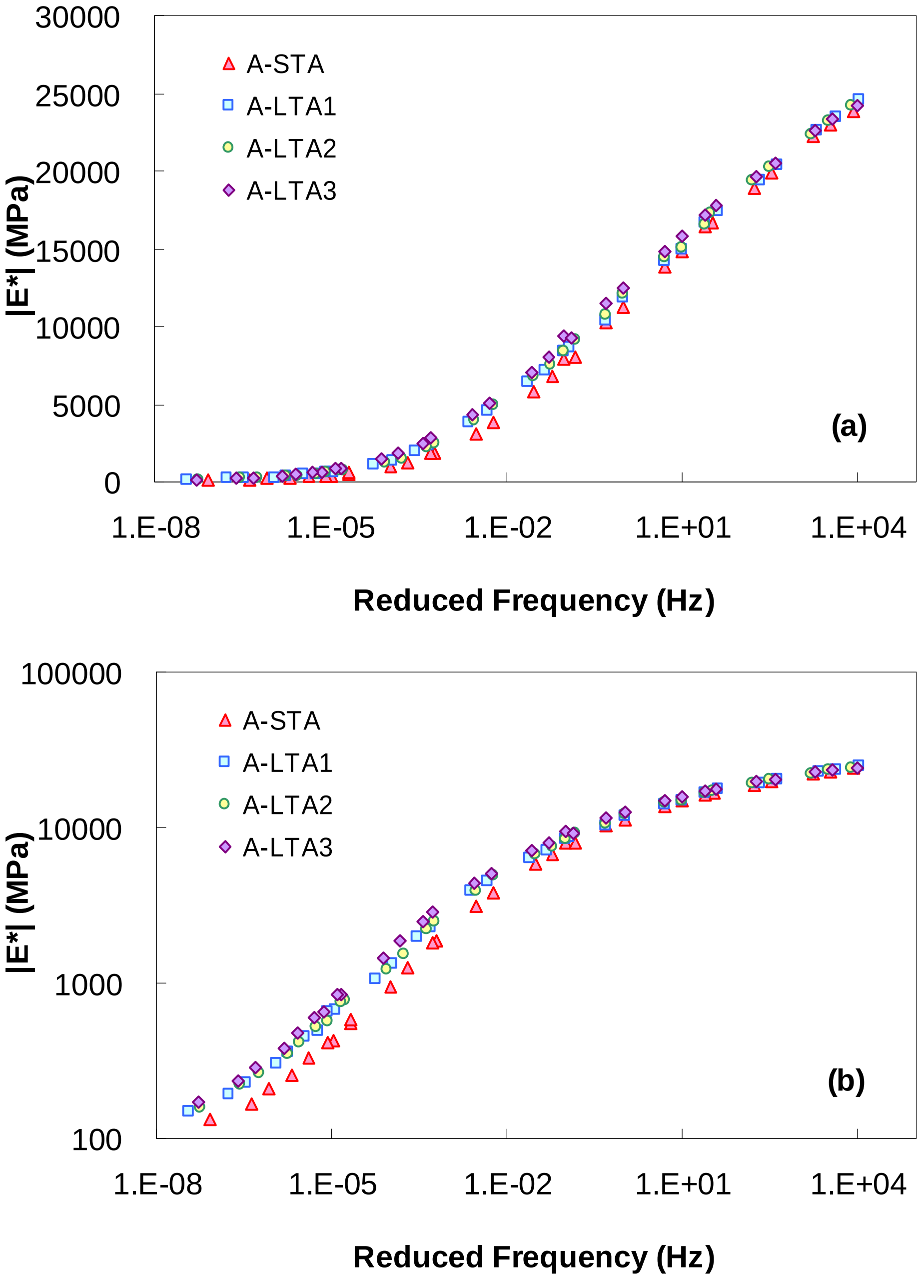

Figure 3-4. Dynamic modulus mastercurves for STA, LTA1, LTA2, and LTA3 aged mixtures of the A mix in: (a) semi-log space, and (b) log-log space

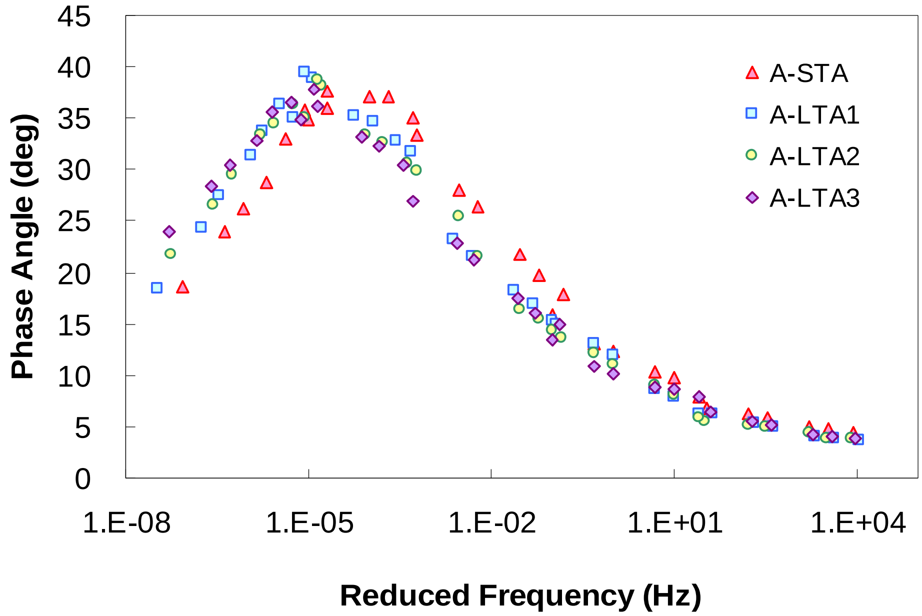

Figure 3-5. Phase angle mastercurves for STA, LTA1, LTA2, and LTA3 aged mixtures of the A mix

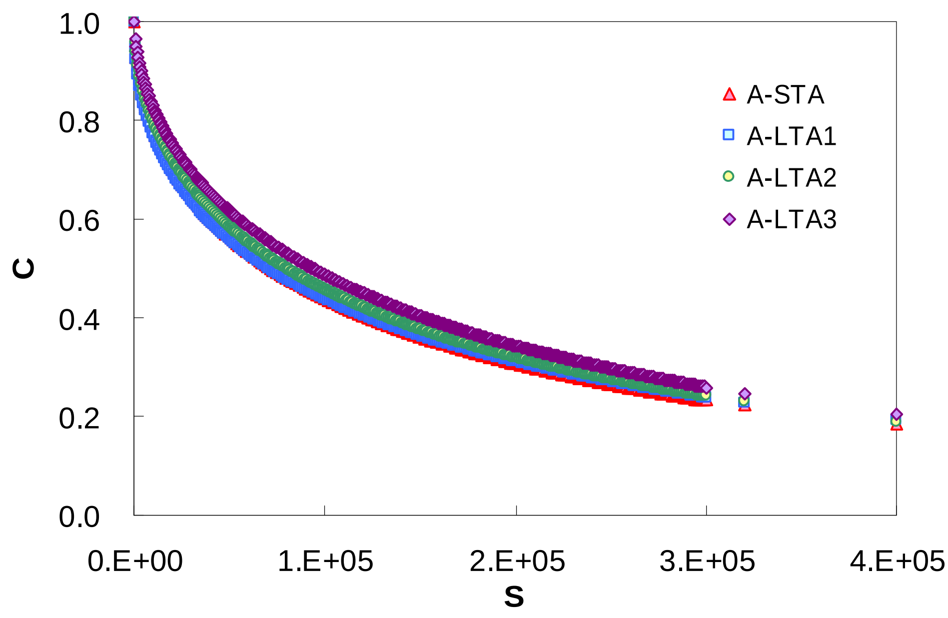

Figure 3-6. Damage characteristic curves for STA, LTA1, LTA2, and LTA3 aged mixtures of the A mix

The AL Mix

Figure 3-7 presents the averaged dynamic modulus mastercurves for the four different levels of aging of the AL mix in both semi-log and log-log scales. It is observed that, compared to the A mix, the effect of aging on the dynamic modulus mastercurves is more significant over all of the frequency ranges. Moreover, a clearer trend with regard to aging time is observed with the AL mix when compared to the A mix. A similar trend can be seen in the phase angle mastercurves graph, shown in Figure 3-8.

To evaluate the statistical differences among the mastercurves for the various aging levels, all replicates results have been analyzed by the step-down bootstrap method. Details of the analysis and results are presented in Section 3.2.4.4. The results reveal that test data for the four aging levels are overall statistically different, except under the most extreme reduced frequencies.

With regard to the damage characteristics, the trend is the same as for the A mix where the damage characteristic curve for the LTA3 mixture is positioned the highest of all, followed next by that of the LTA2 and LTA1 mixtures and, finally, by the STA mixture, as shown in Figure 3-9. However, the differences among the aged mixtures are more significant than those of the A mix.

Care should be taken in concluding from these observations that aging affects the mixture properties relative to performance. The aging effects must be quantified by considering both resistance to deformation (stiffness) and resistance to damage. Hence, the aging effects on pavement performance should be evaluated by conducting the simulations on pavement structure and therefore, both resistances can be simultaneously interacted and as a result, affect the stress-strain redistribution in pavement structure.

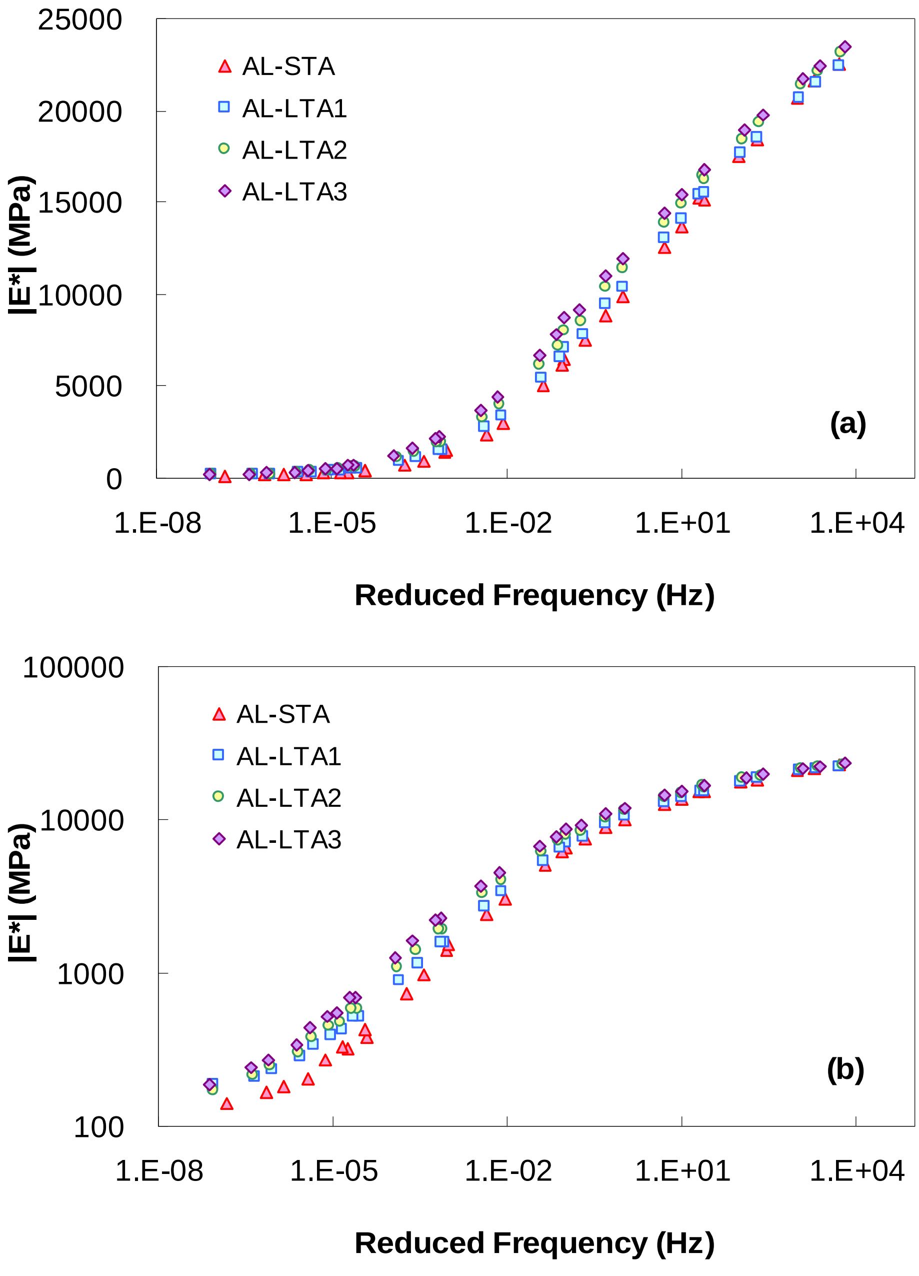

Figure 3-7. Dynamic modulus mastercurves for STA, LTA1, LTA2, and LTA3 aged mixtures of the AL mix in: (a) semi-log space, and (b) log-log space

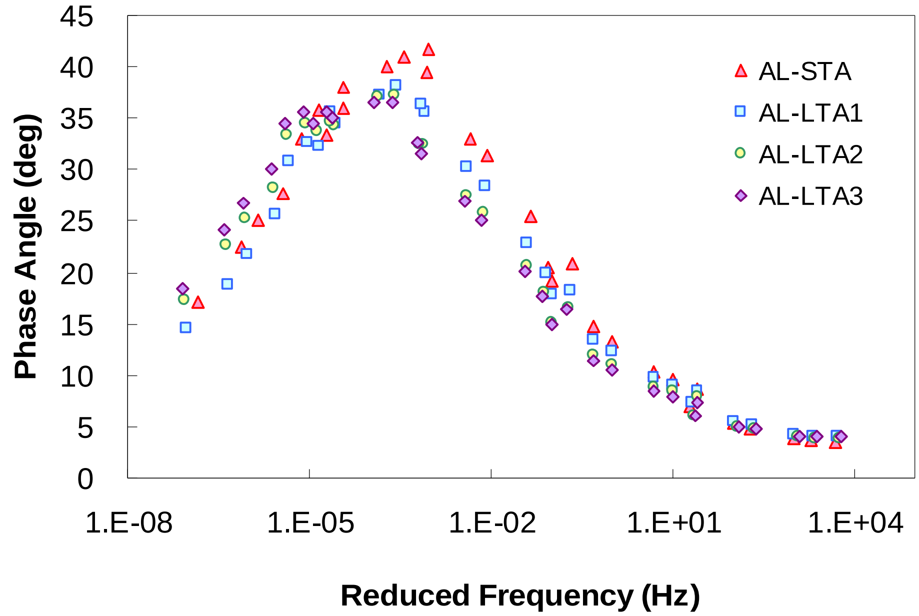

Figure 3-8. Phase angle mastercurves for STA, LTA1, LTA2, and LTA3 aged mixtures of the AL mix

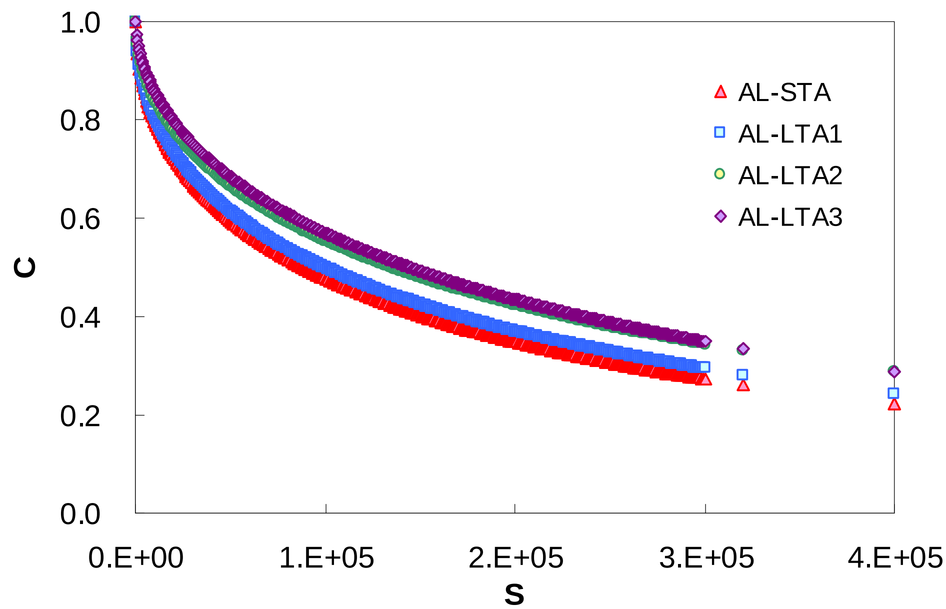

Figure 3-9. Damage characteristic curves for STA, LTA1, LTA2, and LTA3 aged mixtures of the AL mix

3.2.4.4 : Statistical Analysis for Dynamic Modulus Test Results of the AL Mix

A statistical analysis of the dynamic modulus ($|E^*|$) data at different aging levels for the AL mixture has been performed to determine the significance of the graphical observations. Because all the tests were not conducted under exactly the same conditions, each replicate was first processed using interpolation to build a data set for precisely the same temperature and frequency conditions. The specific temperatures and frequency combinations that were compiled are: -10, 5, 20, 40, and 54°C and 25, 10, 5, 1, 0.5, and 0.1 Hz, respectively.

As a first cut analysis, the average dynamic modulus value from each long-term aging level (LTA1, LTA2, and LTA3) is plotted against STA dynamic modulus values at a consistent temperature and frequency condition, as shown in Figure 3-10 (a) and (b). Error bars are shown in these figures and represent a single standard deviation from the mean. The analysis of these figures clearly shows that the test results, i.e., the means plus a single standard deviation, of the LTA specimens are higher overall than those from the STA specimens.

Although this graphical technique may conclude that the differences between the STA and LTA samples are significant, a more comprehensive statistical analysis of these values using the step-down bootstrap method has also been performed. This method is used in lieu of multiple paired t-tests due to the effect of experiment-wise error rates, which can result in incorrect conclusions when making multiple comparisons. Failing to account for this error rate increases the probability of finding significance when none is present. The statistical analysis results are shown by temperature and frequency in Table 3-2. Note that in this table, the conditions under which the means are statistically similar (based on a 95% significance level) are highlighted.

From Table 3-2 the first comparisons to review are those between adjacent aging level test results, i.e., STA versus LTA1, LTA1 versus LTA2, and LTA2 versus LTA3. Overall, statistically different values are found between each adjacent aging level except at the extreme conditions, i.e., a fast frequency at a low temperature and a slow frequency at a high temperature. Based on the standard deviation values shown in Figure 3-10, this finding may be explained by the higher degree of replicate variation under extreme conditions as compared to that under less extreme conditions. A comparison of the two extreme aging conditions, STA versus LTA3, shows that significant differences exist for almost all the conditions except 0.1 Hz at 54°C. Because this condition has the highest amount of variability and is also the most likely to contain experimental errors due to accumulated permanent strain, it is reasonable to conclude that overall a statistically significant effect on the dynamic modulus exists due to the laboratory aging procedures.

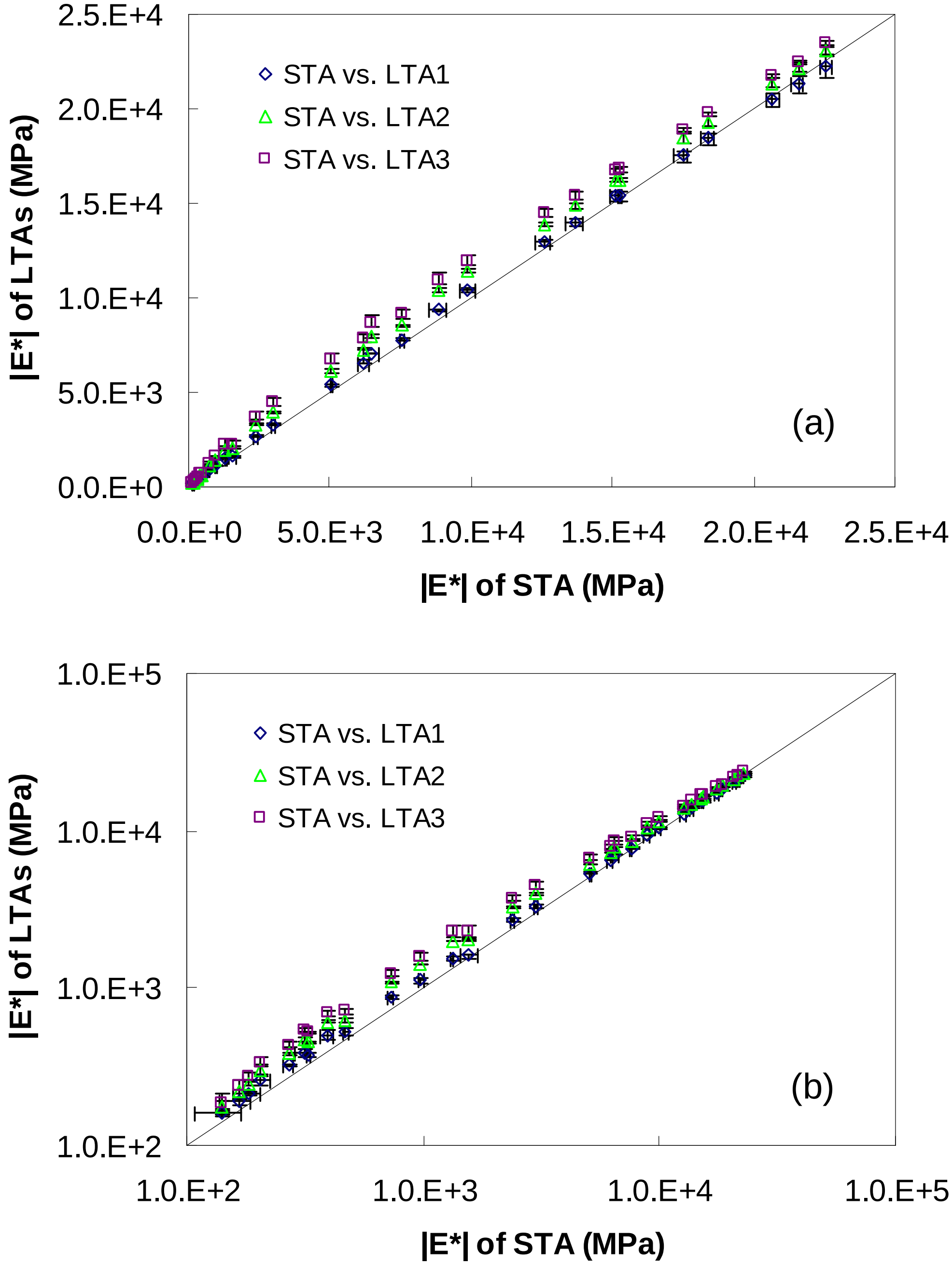

Figure 3-10. Comparison of dynamic modulus of long-term aging levels against the short-term aging level in (a) arithmetic scale and (b) logarithmic scale

Table 3-2. Statistical Analysis Summary of Dynamic Modulus of AL Mix

Temperature (°C)	Frequency (Hz)	p-value					
		STA vs. LTA1	LTA1 vs. LTA2	LTA2 vs. LTA3	STA vs. LTA2	LTA1 vs. LTA3	STA vs. LTA3
-10	25	0.486	0.070	0.100	0.045	0.019	0.019
-10	10	0.589	0.071	0.105	0.044	0.016	0.005
-10	5	0.694	0.047	0.087	0.040	0.014	0.004
-10	1	0.855	0.038	0.034	0.023	0.005	0.005
-10	0.5	0.730	0.035	0.033	0.022	0.006	0.003
-10	0.1	0.460	0.005	0.015	0.001	0.003	0.001
5	25	0.241	0.008	0.031	0.004	0.009	0.009
5	10	0.194	0.012	0.026	0.005	0.010	0.006
5	5	0.142	0.010	0.025	0.004	0.003	0.005
5	1	0.029	0.002	0.040	0.002	0.003	0.006
5	0.5	0.021	0.001	0.033	0.003	0.002	0.008
5	0.1	0.012	0.001	0.024	0.003	0.006	0.011
20	25	0.031	0.004	0.011	0.004	0.006	0.006
20	10	0.047	0.003	0.008	0.006	0.003	0.008
20	5	0.009	0.002	0.012	0.001	0.005	0.005
20	1	0.019	0.002	0.013	0.001	0.003	0.003
20	0.5	0.014	0.003	0.013	0.001	0.003	0.004
20	0.1	0.002	0.000	0.029	0.001	0.008	0.006
40	25	0.429	0.003	0.026	0.006	0.007	0.020
40	10	0.015	0.002	0.011	0.003	0.003	0.001
40	5	0.020	0.001	0.008	0.001	0.003	0.001
40	1	0.023	0.006	0.011	0.002	0.010	0.025
40	0.5	0.025	0.006	0.008	0.001	0.004	0.001
40	0.1	0.054	0.066	0.048	0.017	0.022	0.006
54	25	0.022	0.013	0.021	0.002	0.013	0.002
54	10	0.009	0.001	0.002	0.001	0.003	0.001
54	5	0.022	0.007	0.029	0.002	0.006	0.005
54	1	0.074	0.022	0.140	0.016	0.009	0.016
54	0.5	0.151	0.038	0.132	0.032	0.014	0.023
54	0.1	0.419	0.265	0.507	0.199	0.147	0.132

3.2.4.5 : Incorporation of Aging Effects into the VECD Model

To incorporate the effects of aging into the VECD model, two major parameters must be evaluated: the viscoelastic property and damage characteristics. It is analytically possible to include the effects of aging in the formulation of the current constitutive model using another time variable that accounts for the aging time, as shown in Equations (3-17) and (3-18). The major advantage of this approach is that the interaction between loading and aging can be modeled realistically, thus allowing a more accurate evaluation of the effects of aged binders on mixture properties and the performance of the mixtures. Accounting for the effects of aging on the damage growth of asphalt-aggregate mixtures using fundamental damage mechanics principles is probably the best approach to realistically simulate the interaction between damage and aging that occurs simultaneously in actual pavements.

The pseudo strain of an aged material under uniaxial conditions is represented by the hereditary integral (Equation (3-17)).

$$e^{R} = \frac{1}{E_R}\int_0^x E\left(t,x\right)\frac{de}{dx}dx \tag{3-17}$$

Two time variables are used in this integral: the aging time, t, and the loading time, x. The variable, t, is the time that has elapsed since the specimen was fabricated. From this equation, the relaxation modulus accounts for the aging effects. The relaxation modulus is a function of aging time, loading time, and temperature, and is given as

$$E = E(t, t-t, T) = E(t,x)\ , \tag{3-18}$$

where $x = (t-t)/a_T$, and a_T is the time-temperature (t-T) shift factor. Theoretically, Equation (3-18) results in the mastercurves of different aging times at a specific reference temperature. However, the relaxation mastercurves of the different aged mixtures could not simply be shifted horizontally or vertically to construct a single mastercurve that includes the effects of aging. Moreover, solving Equation (3-17) with the two-dimensional relaxation modulus, Equation (3-18), is analytically difficult. Thus, an alternative, quasi-static approach was followed that takes advantage of the relatively long time scale of aging as compared to the time of loading.

As a result of an analytical investigation, it was found that the coefficients for the dynamic modulus mastercurve and damage characteristic curve, shown in Equations (3-19) to (3-22), generally vary as a power law or exponential model with aging time. To develop a final set of relationships between these coefficients and in-service aging time, the lab aging-to-field aging times suggested by SHRP (3) were selected. This relationship is as follows: 1 year for the STA mix, 4 years for the LTA1 mix, 7.5 years for the LTA2 mix, and 18 years for the LTA3 mix.

The relationships between aging time and the LVE and VECD model coefficients are summarized in Equations (3-23) to (3-26). From these equations it can be observed that the models have been formulated by using the ratio of aged values to original (un-aged) values. This normalized formulation was chosen so that the final function could be applied universally to other mixtures to simulate the aging effects. The model considers ways that the LVE and damage characteristics of a material vary with age. As expected, the model suggests that AC becomes stiffer and less time-dependent with age.

The graphical relationships between aging time and the LVE and VECD model coefficients are shown in Figure 3-11 to Figure 3-13. Generally, the sigmoidal coefficients, shift factor coefficients, and the damage evolution rate (a) vary as a function of aging time in power relationships. The damage coefficients change with aging time by following the sigmoidal type of function shown in Figure 3-13. The best fit relationship between the experimental results and the sigmoidal function was selected to represent the VECD model and, as a result, the relationship appears to be somewhat arbitrary. It cannot be stated definitively that the rapid transition the model suggests should occur between years 7 and 12 may or may not occur in reality. However, a more thorough investigation into the correlation between the oven aging and field aging times for damage characteristics is beyond the scope of the current research.

$$\log|E^*| = a + \frac{b}{1+\frac{1}{e^{d+g\log(f_R)}}} \tag{3-19}$$

$$\log(a_T) = a_1T^2 + a_2T + a_3 \tag{3-20}$$

$$a = 1+\frac{1}{m} \tag{3-21}$$

$$C = e^{mS^n} \tag{3-22}$$

$$\frac{a_{t_e}}{a_{t_0}} = t_e^{a1}, \qquad \frac{b_{t_e}}{b_{t_0}} = t_e^{a2}, \qquad \frac{d_{t_e}}{d_{t_0}} = t_e^{a3}, \qquad \frac{g_{t_e}}{g_{t_0}} = t_e^{a4} \tag{3-23}$$

$$\frac{a1_{t_e}}{a1_{t_0}} = t_e^{a12}, \qquad \frac{a2_{t_e}}{a2_{t_0}} = t_e^{a22}, \qquad \frac{a3_{t_e}}{a3_{t_0}} = t_e^{a32} \tag{3-24}$$

$$\frac{a_{t_e}}{a_{t_0}} = \frac{a_{\max}}{(1+(\frac{k1}{t_e})^{k2})^{k3}} \tag{3-25}$$

$$\frac{m_{t_e}}{m_{t_0}} = \frac{1}{m1+\frac{m2}{1+e^{(m3+m4*t_e)}}}, \qquad \frac{n_{t_e}}{n_{t_0}} = \frac{1}{n1+\frac{n2}{1+e^{(n3+n4*t_e)}}} \tag{3-26}$$

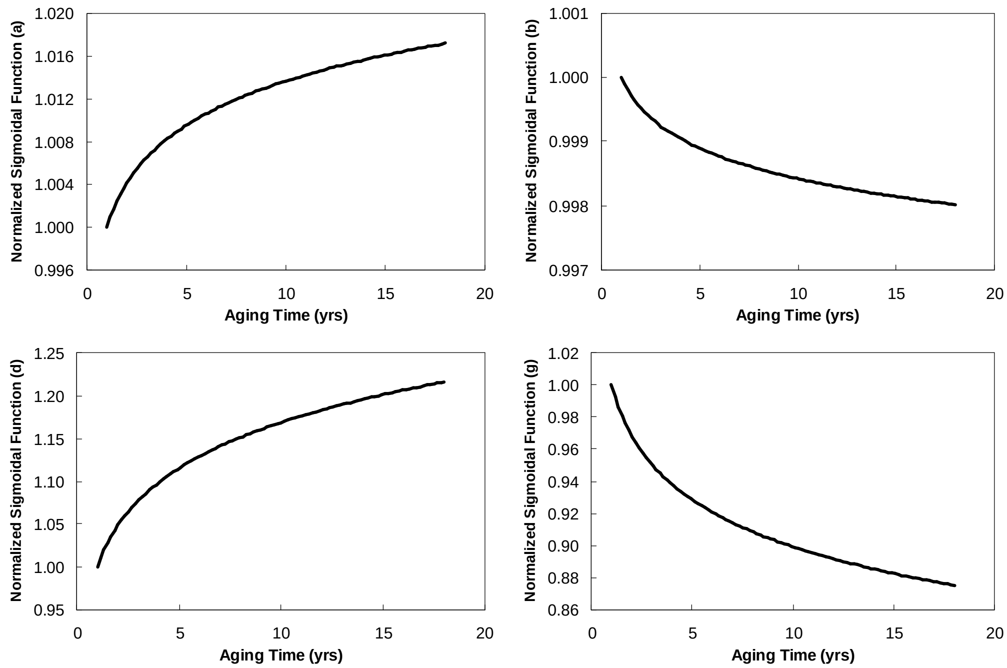

Figure 3-11. Relationship of sigmoidal function coefficients to aging time

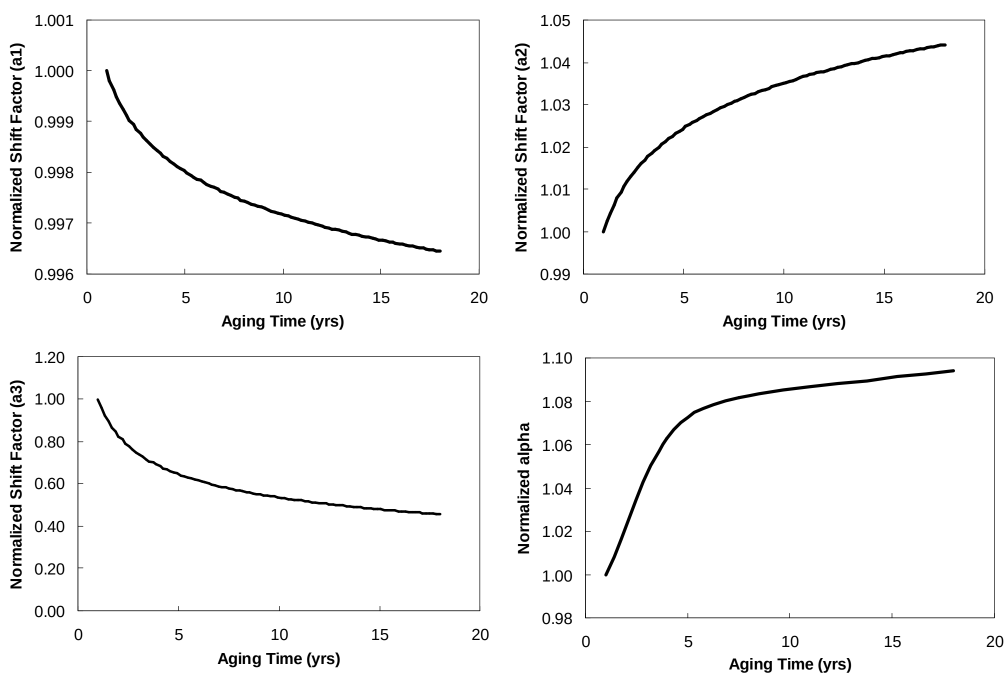

Figure 3-12. Relationship of shift factor coefficients and alpha to aging time

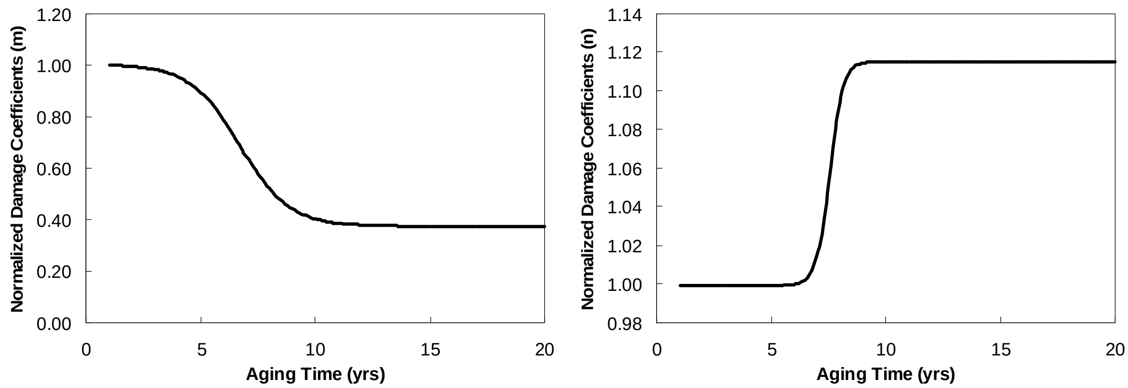

Figure 3-13. Relationship of damage coefficients to aging time

3.2.5 : Failure Criteria as Functions of Aging and Temperature

Aging effects on the performance of asphalt mixtures must be evaluated in terms of the combined effects of stiffness, damage, and failure criteria. A series of cyclic fatigue tests has been conducted to investigate the effects of aging on these characteristics directly and closely. One important finding from this experimental work is that the failure of the specimen occurs at different degrees of damage, depending on the aging level of the mixture and the testing temperature. This section presents comparisons of the fatigue performance for mixtures aged at different levels, then presents a new method to analyze cyclic fatigue tests, and finally, presents the failure criteria used to interpret the FEP++ results.

3.2.5.1 : Cyclic Fatigue Tests

Cyclic fatigue tests using the AL mix were conducted for all four aged mixtures under controlled stress (CS) and controlled crosshead (CX) cyclic conditions. Two amplitudes, high and low, were applied at two temperatures, 5°C and 19°C. The test conditions and some important results, especially the number of cycles to failure (N_f), are summarized in Table 3-3.

To define the number of cycles to failure, the phase angle criterion suggested by Reese (28) is utilized because it seems to work well under both CX and CS test conditions. The phase angle quickly drops in the CX tests and suddenly increases in the CS tests once the specimen fails. One example from the test results for the AL-STA mixture is shown in Figure 3-14. Overall, the dynamic modulus decreases and the phase angle increases according to the number of cycles until the specimen fails, which is when the localization of on-specimen strain starts.

Using the cyclic test results, comparisons can be made with regard to four conditions: 1) magnitude of the input, 2) testing mode, 3) temperature, and 4) aging level. However, care must be taken in comparing these results, because the conditions to be compared are not always the same; e.g., there may be a difference in on-specimen strain for each aged mixture. Nonetheless, the comparisons led to the following conclusions:

- Regardless of testing mode, temperature, and aging level, fatigue resistance decreases as the magnitude of the input increases;
- From the CX test results, and comparing at a similar initial strain magnitude, as the temperature decreases or the aging time increases, the resulting initial stress magnitude increases and the number of cycles to failure (N_f) decreases; and

- From the CS test results, and comparing at a similar initial stress magnitude, as the temperature decreases or the aging time increases, the resulting initial strain magnitude decreases and the number of cycles to failure (N_f) increases.

Overall, the different testing modes result in the opposite fatigue performance; e.g., the STA mix shows better performance in the CX tests, but the LTA3 mix shows better performance in the CS tests. It is known, based on energy principles, that stiff materials tend to perform better in CS test protocols, whereas soft materials yield better performance in CX tests, all other factors being equal. In this case, however, all the factors are not equal because aging has occurred, which has somewhat embrittled the LTA mixes. The experimental data suggest that this embrittlement may not be as significant for the CS tests. As noted above, soft materials should perform better in the CX test protocols, and because the softest mixture is also the least embrittled, i.e., the STA, the CX test results cannot be used reliably to determine the exact effects of this embrittlement process.

However, it should be noted that these cyclic test results correspond to the findings from other researchers. Kutay et al. (17) reported that, depending on the mode of loading (i.e., stress- or strain-controlled), the ranking of the mixtures can be quite different. Kutay et al. also concluded that stress-controlled push-pull tests reveal a reverse trend when compared to field fatigue data obtained from the FHWA Accelerated Load Facility (ALF). On the other hand, strain-controlled tests provide the correct trend even though the degree of correlation with the field results is poorer than that of stress-controlled tests.

Table 3-3. Cyclic Fatigue Test Summary (Frequency of 10 Hz)

Mix ID	Specimen ID	Test Designation	Initial Stress Amplitude in Tension (kPa)	Initial Peak-to-Peak Strain (Microstrain)	N_f
AL-STA	AL229	19[a]-CX[b]-H[c]	1,700	582	3,091
	AL232	19-CX-H	1,400	415	8,908
	AL231	19-CX-L	610	162	> 150,000
	AL246	19-CS-H	750	152	1,610
	AL238	19-CS-L	250	50	46,200
	AL233	5-CX-H	2,870	274	3,498
	AL239	5-CX-L	980	87	> 280,000
	AL248	5-CS-H	1,500	120	4,000
	AL247	5-CS-L	900	76	44,700
AL-LTA1	AL228	19-CX-H	1,790	466	3,613
	AL242	5-CX-H	2,900	259	3,100
	AL244	5-CX-L	920	74	> 280,000
	AL243	5-CS-H	1,500	107	4,590
	AL245	5-CS-L	900	66	77,000
AL-LTA2	AL225	19-CX-H	2,020	483	2,753
	AL250	5-CX-H	3,210	264	713
	AL241	5-CX-L	1,180	84	> 280,000
	AL249	5-CS-H	1,500	99	4,200
	AL240	5-CS-L	900	64	97,200
AL-LTA3	AL220	19-CX-H	2,030	419	1,383
	AL234	5-CX-H	3,220	253	800
	AL235	5-CX-L	1,810	134	> 280,000
	AL237	5-CS-H	1,500	95	8,900
	AL236	5-CS-L	900	52	167,000

[a] Test temperature in degrees Celsius; [b] Test mode; [c] Relative magnitude: H=high, L=low

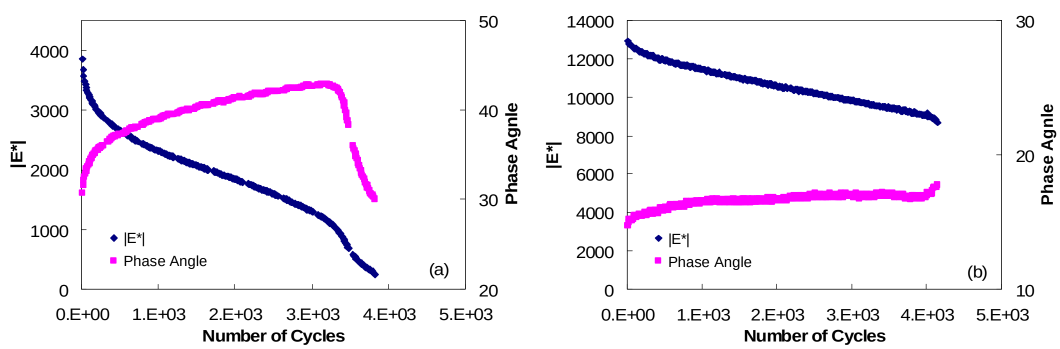

Figure 3-14. Changes in dynamic modulus and phase angle as the cyclic loading continues (AL-STA mix): (a) the CX test (AL229), and (b) the CS test (AL248)

3.2.5.2 : VECD Analysis of Cyclic Test Results

Simplified VECD Model

Recently, a new simplified model for the analysis and prediction of cyclic data has been developed using the current VECD model constitutive functions. The major difference between this simplified VECD (S-VECD) model and the more rigorous VECD model is the use of a simplified pseudo strain calculation methodology for the cyclic portion, as shown in Equation (3-27). The overall effect of such a simplification on the value of pseudo strain is found to be small, but the simplification is found to save a great deal of computational time without causing a large error in the calculations. In addition, the resulting formulation unifies the results of the CS, CX, and monotonic testing and supports earlier findings that the damage characteristic curve is a material property independent of temperature and test type. The simplified model formulations are shown in the following equations with descriptions of the variables (38).

$$e^R = \begin{cases} e^R = \dfrac{1}{E_R}\displaystyle\int_0^x E(x-t)\dfrac{d(e)}{dt}dt & x \le x_p \\ \left(e^R_{0.ta}\right)_i = \dfrac{b+1}{2}\left(\left(e_{0,pp}\right)_i * \left|E^*\right|_{LVE}\right) & x > x_p \end{cases} \tag{3-27}$$

$$dS = \begin{cases} \left(dS_{Transient}\right)_{timestep\ j} = \left(-\dfrac{1}{2}\left(e^R\right)_j^2 \Delta C_j\right)^{a/1+a} \times \left(\Delta x\right)_j^{1/1+a} & x \le x_p \\ \left(dS_{cyclic}\right)_{cycle\ i} = \left(-\dfrac{I}{2}\left(e^R_{0.ta}\right)_i^2 \Delta C^*_i\right)^{a/1+a} \times \left(\Delta x_p\right)_i^{1/1+a} \times \left(R\right)^{1/1+a} & x > x_p \end{cases} \tag{3-28}$$

$$C = \begin{cases} C = \dfrac{S}{e^R I} & x \le x_p \\ C^* = \dfrac{S_{0,ta}}{e^R_{0,ta} I} & x > x_p \end{cases} \tag{3-29}$$

$$b_i = \frac{\left(s_{peak}\right)_i + \left(s_{valley}\right)_i}{\left|s_{peak}\right|_i + \left|s_{valley}\right|_i} \tag{3-30}$$

$$R = \frac{1}{x_f - x_i} * \int_{x_i}^{x_f} \left(f(x) \right)^{2a} * dx \tag{3-31}$$

where x_p = reduced pulse time of the loading pulse,

e_0^R = cyclic pseudo strain amplitude,

$|E^*|_{LVE}$ = linear viscoelastic dynamic modulus of the material at the particular temperature and frequency of the test,

C^* = cyclic pseudo stiffness,

e_0 = cyclic strain amplitude (only tension amplitude if loading is in tension and compression),

b = a factor that allows direct quantification of the duration that a given stress history is tensile,

R = form adjustment factor,

x_i = reduced time within loading cycle when tensile loading begins,

x_f = reduced time within loading cycle when tensile loading ends, and

$f(x)$ = normalized time function found from loading type assumption.

The transient portion of the loading history, i.e., the first half of the first cycle, is important because it is used to define the specimen-to-specimen correction factor, I, and because damage growth in this first loading path can be significant. The a in the simplified model formulations is defined as $1/m+1$ for the constant rate and CX tests, and as $1/m$ for the CS tests. This definition of a is based on theoretical arguments and has been verified using short-term aged (STA) materials only. Its universality with regard to materials tested at other aging conditions was not verified in the original work (38).

Because the CS and CX tests fail in different patterns, two different criteria are necessary. From the study by Underwood et al. (38), two criteria have been adopted to define the cycle in which data can be used in the VECD characterization process: 1) the phase angle criterion, and 2) the threshold criterion. The phase angle criterion is the same as that used in defining the number of cycles to failure (N_f) suggested by Reese (28). The concept of the threshold criterion is that when processes other than damage mechanisms, such as viscoplasticity, begin to have a significant effect, then a test no longer can be used directly for characterization. It is believed that the onset of other mechanisms is closely related to the total amount of permanent strain experienced by the specimen. From experience with the constant crosshead rate tests at 5°C, it is known that for any given mixture, tests performed at certain rates show similar strain levels at the peak stress, as shown in Figure 3-15 (a). In this figure, the straight lines represent the averaged strain levels for each aged mixture, and these strain levels are clearly ranked according to aging level. These mixture-dependent strain levels represent a known level below which VECD mechanisms dominate. The cycle in the fatigue tests at which the permanent strain (backcalculated from the measured permanent pseudo strain) exceeds this threshold is taken as the point after which the data cannot be used for VECD characterization. Figure 3-15 (b) shows the cut-off point schematic for the AL-STA mix. As can be seen, the cut-off criterion is applied only to the CS tests.

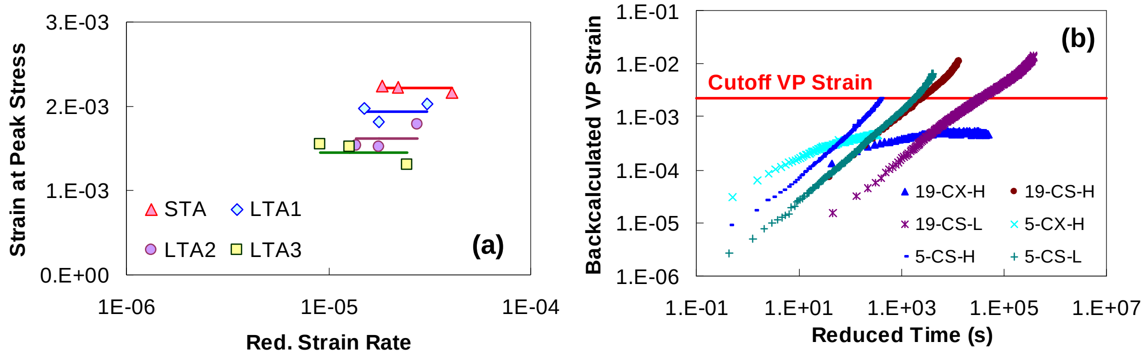

Figure 3-15. (a) Strain at peak stress for AL mix and (b) Cut-off viscoplastic strain level for AL-STA mix

Damage Characteristics from Cyclic Tests

From the work by Underwood et al. (38), it is known that the damage characteristic curves obtained from CS, CX, and monotonic testing collapse into a single curve, indicating that the property represented by these curves is fundamental and independent of temperature and test type. Initially, the cyclic data for the aged mixtures were analyzed following the method by Underwood et al. (38), but the damage characteristic curves obtained from the different modes of testing did not collapse well, although the collapse in each test mode was acceptable. This analysis showed that the samples conditioned for the LTA mixes produced poorer results than those conditioned only for the STA mix. Thus, some trials were conducted, and the resultant damage characteristic curves collapsed reasonably using two options taken from the originally suggested analysis method: 1) the a function is defined as $1/m+1$ for the monotonic test and $1/m$ for the CX and CS tests, and 2) the correction factor, I, is set to one for all the cyclic tests. It should be noted that these differences in the current and earlier work for analyzing cyclic test results still need to be investigated. Because the definition of a in the original model is based on theoretical arguments and has been verified using STA materials only, its universality with regard to materials tested at other aging conditions was not verified in the original work (38). Figure 3-16 shows the damage characteristic curves of the AL-STA mixture obtained from the monotonic, CX, and CS tests. All the cyclic test data are included in this plot and collapse well with each other. The damage characteristic curves for all four aged mixtures are shown together in Figure 3-17 for only the tests that have been performed under the same testing condition, i.e., 19-CX-H. The collapses are good except for the discrepancy between the monotonic and cyclic results of the LTA1 mixture.

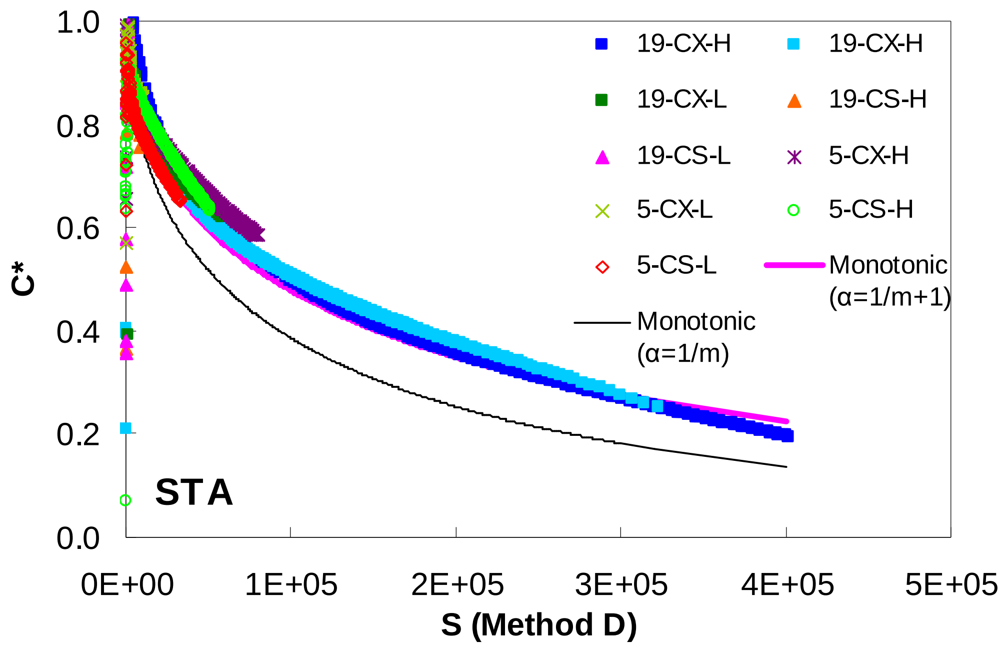

Figure 3-16. Damage characteristic curves of AL-STA mix (all cyclic test data included)

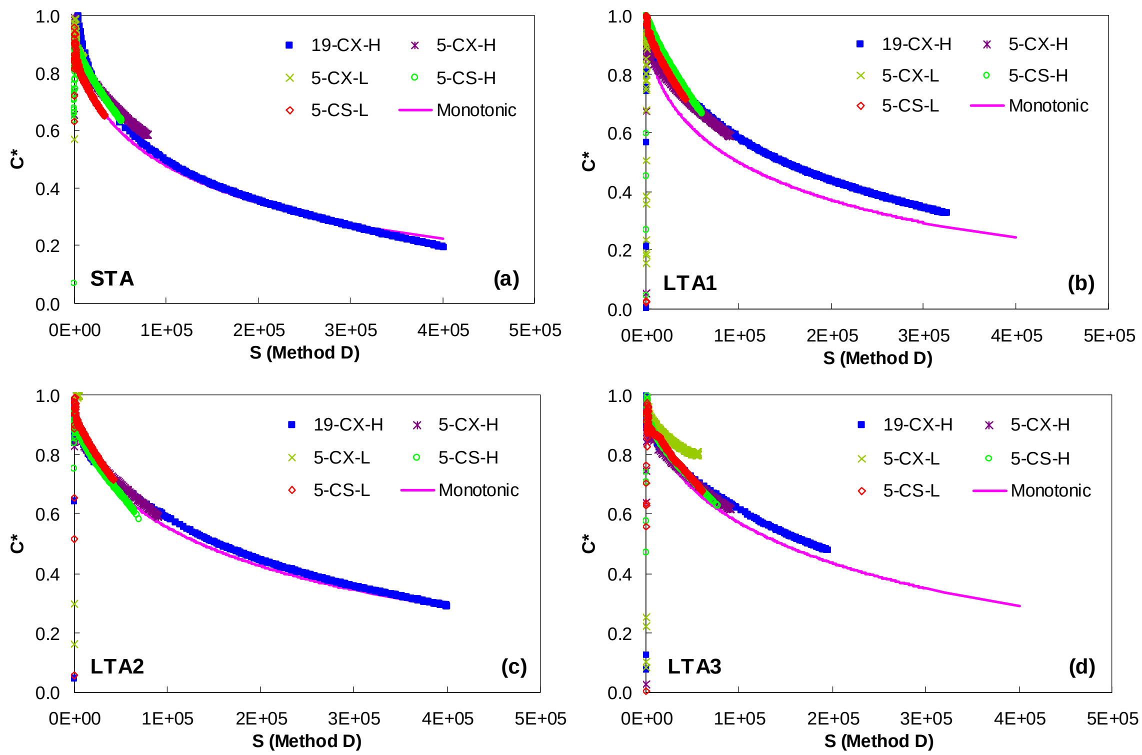

Figure 3-17. Damage characteristic curves of: (a) STA, (b) LTA1, (c) LTA2, and (d) LTA3 aged mixtures of AL mix

3.2.5.3 : Failure Criterion

The general failure criterion developed in previous work (12) is based on reduced frequency and does not include the aging effect on the failure. Because the failure criterion does not include aging time and because the reduced frequency basis approach is not amenable for use with the VECD-FEP++, a temperature-only based failure criterion has been developed that includes the aging effect in the failure definition.

In Figure 3-18, the pseudo stiffness (C) values at failure are plotted against the test temperatures for the CX tests for all aged mixtures. It is observed that the C values at failure decrease as the temperature increases for all aging levels. It is also found that the aging effect on failure is most noticeable at 19°C. Such a trend can be expected because of the aforementioned tendency of AC to embrittle with age. On the other hand, all the aging mixes failed at similar C values at 5°C. This result is due mainly to the fact that AC is brittle enough at low temperatures that the aging effect is not significant.

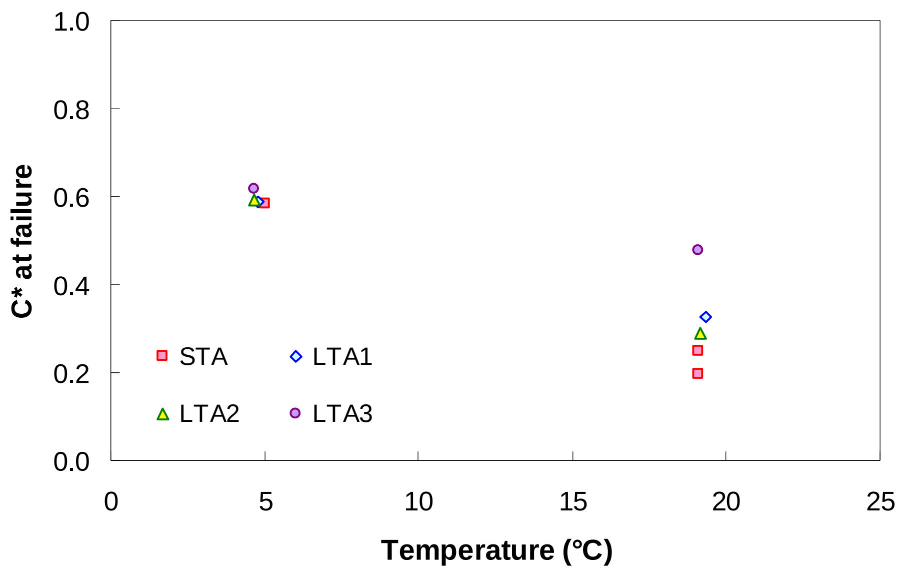

Figure 3-18. Variation of C at failure from cyclic fatigue tests

Because of limited test data, it is assumed that the failure criterion varies linearly between 5°C and 19°C and is constant beyond this range. It is also noted that all data at 5°C are averaged, and that the LTA1 and LTA2 data are averaged because they show similar values, as shown in Figure 3-19. Therefore, the piecewise function is used for the failure criterion, as shown in Equation (3-32). Like the aging model, the failure criterion is formulated by the ratio of the aged value to the original (un-aged) value so that it can be universally applied to other mixtures according to the aging effect.

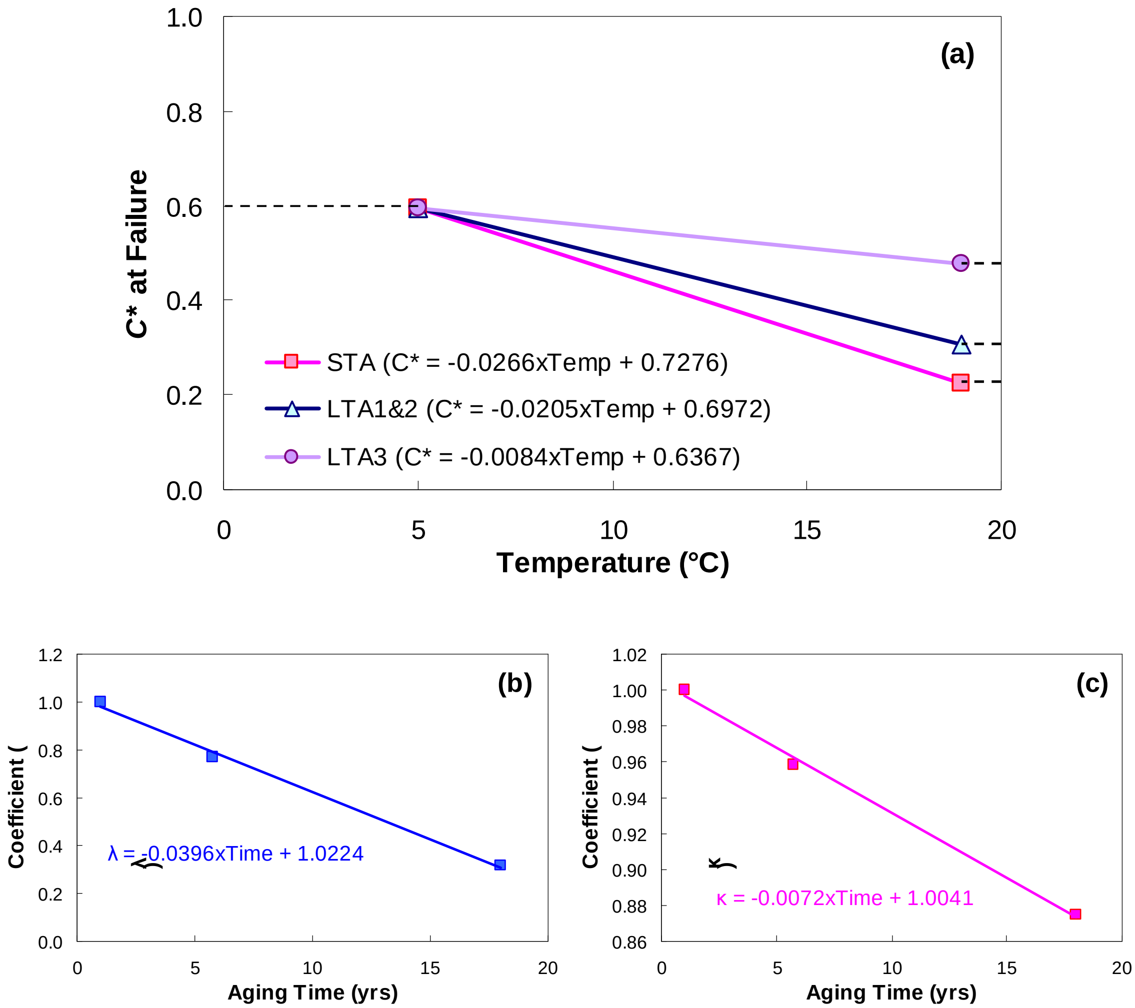

Figure 3-19. (a) Failure criterion; (b) and (c) variation of coefficients λ and κ as functions of temperature and aging, respectively

$$C_f = \begin{cases} (\frac{l_{t_e}}{l_{t_0}})*5 + (\frac{k_{t_e}}{k_{t_0}}) & T \le 5°C \\ (\frac{l_{t_e}}{l_{t_0}})*T + (\frac{k_{t_e}}{k_{t_0}}) & 5°C < T < 19°C \\ (\frac{l_{t_e}}{l_{t_0}})*19 + (\frac{k_{t_e}}{k_{t_0}}) & T \ge 19°C \end{cases} \qquad (3\text{-}32)$$

where $\frac{l_{t_e}}{l_{t_0}} = l1 * t_e + l2$, $\frac{k_{t_e}}{k_{t_0}} = k1 * t_e + k2$, and $l1,\ l2,\ k1,\ k2$ = constant.

3.2.6 : Healing Model

As a place-holder for a fully mechanistic, potentially micromechanically motivated healing model, a simplified version of the phenomenological mechanical model, which was derived, characterized and verified by Lee and Kim (18), has been applied into the model framework. A simplified version of this model is used here in light of the fact that the previous formulation, of which the healing model is a part, has certain shortcomings in its rigor, and the fact that modifying the material model for the FEP++ would require significant time. The primary disadvantage of this model is the lack of characterization and verification data under various conditions that are needed for the FEP++ simulations. For this reason, an empirical adjustment has been made to improve the engineering reasonableness of the simplified model. This section presents the development and evaluation of the simplified healing model by Underwood (39).

3.2.6.1 : Previous Formulation

The healing model formulation is encapsulated in the general framework of the VECD model, as it is coded in the FEP++. However, the healing model includes two additional damage parameters (S_2 and S_3) and pseudo stiffnesses (C_2 and C_3) that the current model does not include. Recall that the VECD model, shown in Equation (3-33), includes only a single damage parameter, S_1, and material integrity term, C_1. The additional terms are included mathematically in the healing function shown in Equation (3-34) where they are shown to physically represent the increase in pseudo stiffness during the rest periods, $C_2(S_2)$, and the reduction in pseudo stiffness as the healed material is redamaged, $C_3(S_3)$. These material functions are independent of the amount of damage in the virgin material, i.e., $C_1(S_1)$.

$$s = C_1\left(S_1\right)e^R \tag{3-33}$$

$$s = \left[C_1 + H\right]e^R \tag{3-34}$$

where

$$H = \left[S_{B,i}^R + C_2\left(S_{2,i}\right)\right]C_3\left(S_{3,i}\right) - C_1\left(S_1\right) - \sum_{j=1}^{i-1} S_{B,j}^R - S_{C,j}^R \,,$$

if both the healed and virgin materials are damaged (see Region 1 in Figure 3-20); or

$$H = \sum_{j=1}^{i-1} S_{B,j}^R - S_{C,j}^R \,,$$

if only the virgin material is damaged (see Region II in Figure 3-20).

The meaning of the pseudo stiffness term, $S^R{}_n$, is given in Figure 3-20 where the model behavior for a single rest and reloading period is shown schematically. The evolution laws for the S_2 and S_3 damage parameters are given in Equations (3-35) and (3-36), respectively. The relationships between these damage parameters and their respective material integrity parameters are given by Equations (3-37) and (3-38). The coefficients for these equations, as characterized by Lee and Kim (18), are summarized in Table 3-4.

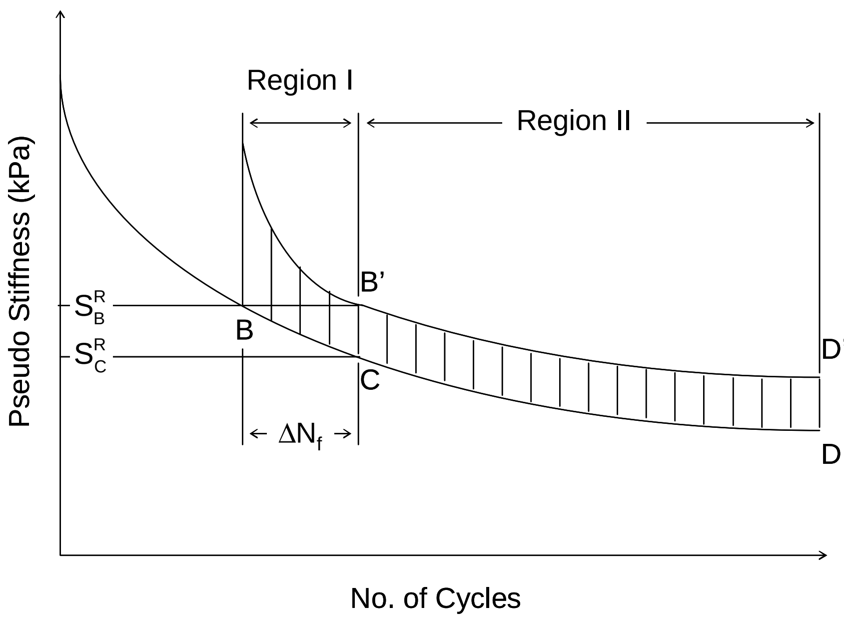

Figure 3-20. Effect of rest period on pseudo stiffness

$$S_2 = \int_0^{t_{rp}} \left[\frac{1}{2} \left(e^R \right)^2 \frac{\partial C_2}{\partial S_2} \right]^{a_2} dt \tag{3-35}$$

$$\dot{S}_3 = \left[-\frac{S_A^R}{2} \left(e^R \right)^2 \frac{\partial C_3}{\partial S_3} \right]^{a_3} \tag{3-36}$$

$$C_2\left(S_2\right) = C_{20} + C_{21}\left(S_2\right)^{C_{22}} \tag{3-37}$$

$$C_3(S_3) = C_{30} - C_{31}(S_3)^{C_{32}} \quad (3\text{-}38)$$

Table 3-4. Previous Healing Model Formulation Coefficients

Coefficient	AAM Value	AAD Value
Function C_1		
C_{10}	0.9900	1.1000
C_{11}	0.0065	0.0764
C_{12}	0.4400	0.2000
α_1	2.6950	2.7860
Function C_2		
C_{20}	-0.3750	0.0015
C_{21}	0.0941	0.0004
C_{22}	0.2000	0.6200
α_2	1.7000	1.5000
Function C_3		
C_{30}	1.0100	1.0100
C_{31}	0.0019	0.0114
C_{32}	0.5500	0.3000
α_3	2.1000	2.0000
t-T Shift Factor		
α_1	0.0009	0.0012
α_2	-0.1602	-0.1843
α_3	3.3709	3.9471
T_R	25	25

3.2.6.2 : Simplified Formulation

The basic trends found in the above formulation and numerous experimental studies (7, 14, 15) are shown in Figure 3-21. In short, the more time that elapses between load applications, then the more the pseudo stiffness will recover, and hence, the longer the fatigue life will be extended. The amount of recovery is most sensitive to the rest period duration, but the model also suggests that recovery is a function of the previous load intensity and the total cumulative amount of damage that exists in the material. The previous formulation includes these factors by including multiple parameters and damage functions. For the simplified model, an attempt is made to use only a single material function, $C_1(S_1)$, to accomplish the same objective. A closer examination of the previous formulation shows that it is not possible to directly quantify the increase in pseudo stiffness with a single function because, as shown in Figure 3-20, the healed material is more sensitive to loading than the virgin material.

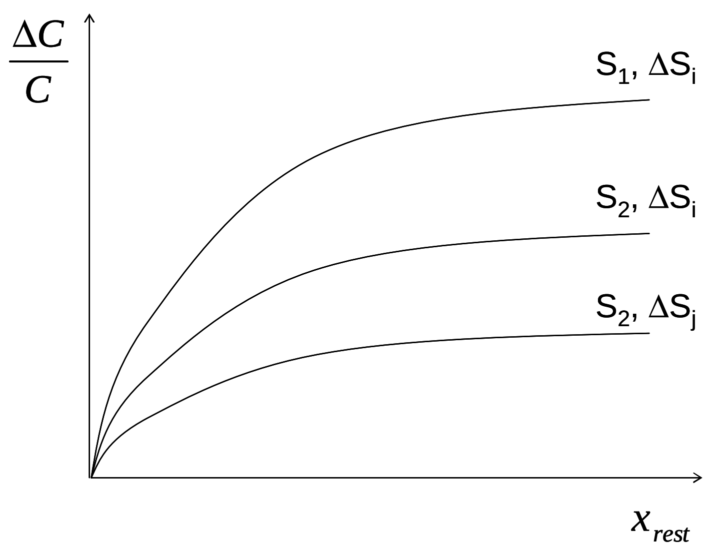

Figure 3-21. Effect of rest period on material healing

The basic concept of the simplified model is diagrammed schematically in Figure 3-22 where damage characteristic curves are shown for the first three cycles of loading. The points evenly labeled (0, 2, and 4) represent the pseudo stiffness values at the beginning of load pulses 1, 2 and 3. The points labeled with the odd numbers (1, 3, and 5) represent the pseudo stiffness values at the end of load pulses 1, 2 and 3. The single damage parameter model will predict that during the first cycle, damage will grow from point 0 to point 1. The simplified model would then suggest that during some rest period the material would heal back (i.e., recover) to point 2. Then, when loading begins for the second cycle, the damage would grow to point 3. Upon resting after the end of the second cycle, healing would increase the pseudo stiffness to point 4. Finally, after the third loading cycle, the damage would grow to point 5. In total, then, there are three different segments where damage is assumed to occur in the virgin material: from point 0 to point 1; from point 1 to point 3 (second cycle); and finally from point 3 to point 5 (third cycle). Similarly, there are only two segments where damage is assumed to occur in the healed material: from point 2 to point 1 (second cycle) and from point 4 to point 3 (third cycle). Between each of these points, though, a single damage function, $C_1(S_1)$, is used to compute the damage.

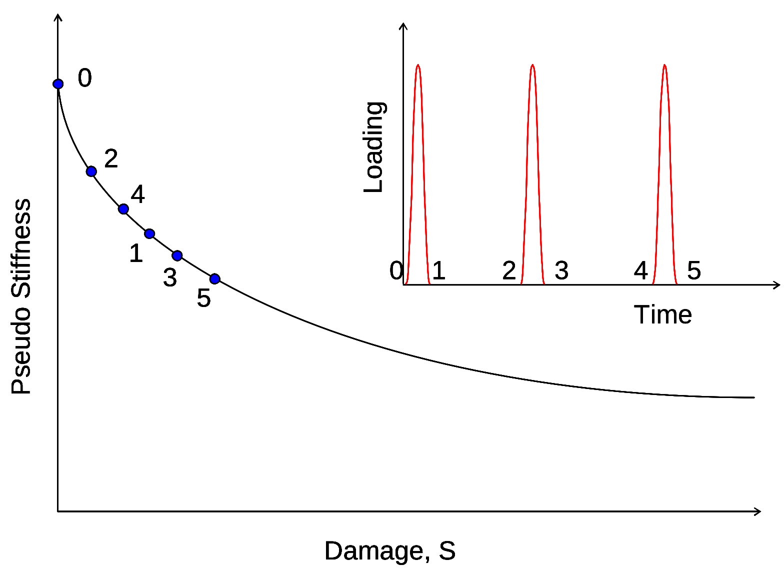

Figure 3-22. Conceptual schematic diagram for the simplified model

In order to use the previous formulation, a systematic factorial data set was created for the different rest periods (x 7), damage levels (x 9), and energy inputs, DS (x 7), which have values that could be expected in any given FEP++ simulation. For each of these combinations, the previous formulation was used to predict the pseudo stiffness at the end of the cycle after the rest period, i.e., point 3. Then, S_H in Equation (3-39) was determined through optimization to give the same pseudo stiffness value after a load pulse; e.g., damage was found at point 2, so when calculating damage growth, the resulting pseudo stiffness was equal to that at point 3. The pseudo stiffness at this healed damage level was then calculated using Equation (3-40), and finally used to compute the value of the change in pseudo stiffness (DC), which is the difference between the pseudo stiffness values at point 1 and point 2. In order to apply the outcomes universally, the damage level, *S*, and energy input, DS, were normalized to the damage level at failure, S_f, and the change in pseudo stiffness was normalized to the pseudo stiffness level.

$$S_{i+1} = S_H + \left(-\frac{1}{2} \left(e^R \right)^2 \frac{\partial C}{\partial S} \right)^{a_1} \tag{3-39}$$

$$C_H \left(S_H \right) = C_{10} - C_{11} \left(S_H \right)^{C_{12}} \tag{3-40}$$

After calculating the change in pseudo stiffness for the multiple conditions, a regression model was characterized for easy use. The basic model is shown in Equation (3-41) where the coefficients are found to depend on the damage level and energy input, as seen in Equations (3-42) to (3-50). Note that the model is presented in terms of reduced rest time, x_{rest}, which is defined in Equation (3-51) by combining the physical rest period, t_{rest} and the t-T shift factor function, which is a second order polynomial, at some reference temperature, T_R (25°C).

$$\frac{\Delta C_{Heal}}{C} = \frac{k}{\left(1+\left(\frac{b}{x_{rest}}\right)^{g}\right)^{d/g}} \tag{3-41}$$

$$k = k_1\left(\frac{\Delta S}{S_f}\right)^{k_2} \tag{3-42}$$

$$k_1 = ae^{b*\left(S/S_f\right)} \tag{3-43}$$

$$k_2 = -c\left(S/S_f\right)^{d} \tag{3-44}$$

$$b = b_1\left(\frac{\Delta S}{S_f}\right)^{b_2} \tag{3-45}$$

$$b_1 = fe^{g*\left(S/S_f\right)^{h}+i*\left(S/S_f\right)} \tag{3-46}$$

$$b_2 = -je^{k*\left(S/S_f\right)} \tag{3-47}$$

$$g = g_1 \tag{3-48}$$

$$g_1 = le^{m*\left(S/S_f\right)} \tag{3-49}$$

$$d = n+\left(\frac{o}{1+e^{p+q\log\left(S/S_f\right)}}\right)\left(\frac{\Delta S}{S_f}\right)^{d_2} \tag{3-50}$$

$$x_{rest} = \frac{t_{rest}}{a_T} = \frac{t_{rest}}{10^{a_1\left(T^2 - T_R^2\right) + a_2\left(T - T_R\right)}} \tag{3-51}$$

The coefficients for this model are summarized in Table 3-5 for Lee and Kim's AAD and AAM mixtures (18). These two mixtures represent, respectively, a light healing and a heavy healing material. Because the model is normalized, i.e., it predicts the ratio of change in pseudo stiffness to current pseudo stiffness, DC/C, it can be applied universally to other mixtures to simulate heavy healing and light healing. The strength of the characterized model is shown for the AAD mixture in Figure 3-23.

Table 3-5. Simplified Healing Model Coefficients: Summary of AAD and AAM Mixtures

Coefficient	AAM Value	AAD Value
Function α		
a	0.1679	0.1657
b	2.2695	2.8865
c	0.0548	0.0261
d	0.2572	0.2379
Function β		
f	27.3913	1.5144
g	-1.5887	-4.7659
h	30.1058	5.0763
i	-5.8228	-3.3953
j	0.5070	0.5290
k	-8.1700	-3.0063
Function γ		
l	1.4707	1.2448
m	-1.6387	-1.6425
Function δ		
n	-0.3593	1.0526
o	30.1626	7.2289
p	2.8853	1.7666
q	-0.2850	-2.0453
r	-0.0843	-0.1597

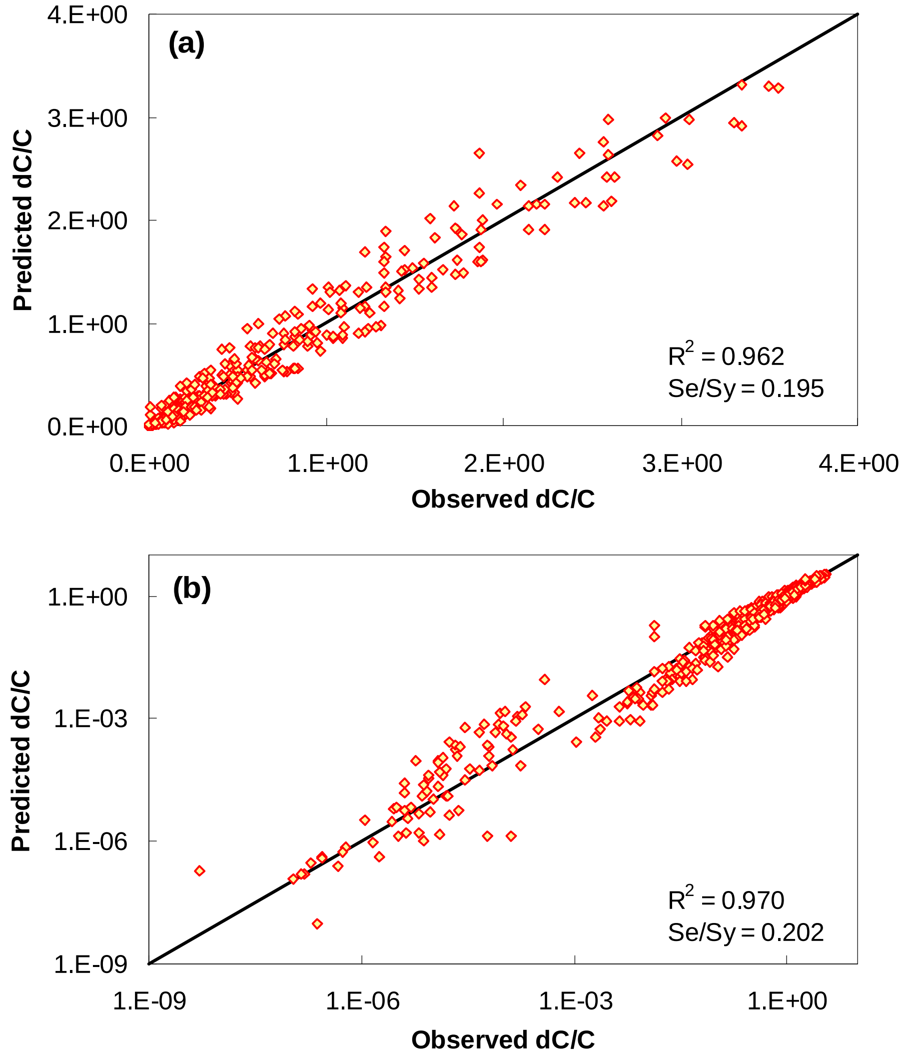

Figure 3-23. Strength of simplified model for AAD mixture in: (a) arithmetic and (b) logarithmic scales

3.2.6.3 : Healing Potential Factors

One shortcoming of the simplified model, which has transferred from the previous formulation, is its handling of rest periods that are introduced before the healed material has been entirely redamaged, e.g., the rest periods in Region I. This issue is represented schematically in Figure 3-24, but was not encountered during the development of the more robust healing model because Lee and Kim (18) never performed experiments in which the subsequent healing and redamaging occurred in Region I of the previous healing cycle. This situation is important in the context of FEP++ simulations because each load pulse is followed by a rest period, and only a single load pulse is applied after each rest period. It is believed that the behavior suggested by the previous formulation, and shown in Figure 3-24, is unrealistic, because the repeated redamaging of the healed material should actually limit the healing potential; thus, the response schematically depicted in Figure 3-25 is deemed more appropriate than that shown in Figure 3-24 (previous formulation).

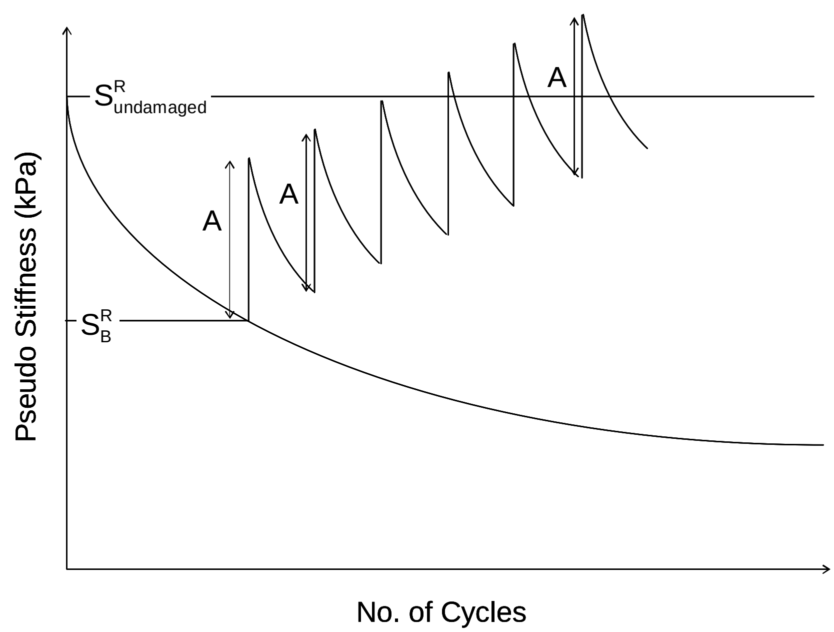

Figure 3-24. Effect of damage and healing in Region I using previous formulation

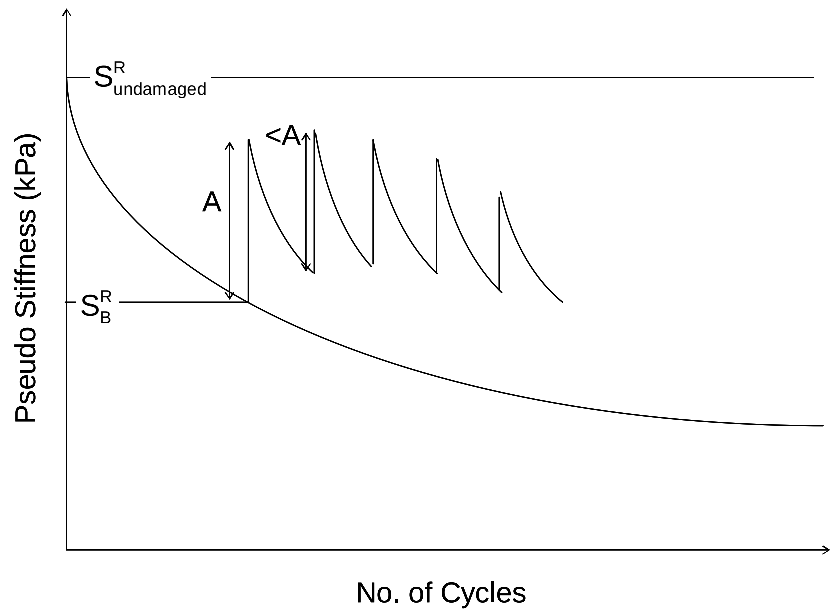

Figure 3-25. Engineering reasonableness representation of expected material behavior

Because not all damage occurs in the healed material, a correction factor was formulated to be a function of the total summed damage that occurs in the material. This correction factor is hereafter referred to as *healing potential factor-C*. Damage related to the redamage of healed material is considered to be negative damage, and the damage related to virgin material is considered to be positive damage. Referring to Figure 3-22, the damage that occurs from point 0 to point 1, point 1 to point 3 (second cycle), and finally point 3 to point 5 (third cycle) is calculated as a positive value. Then, the damage that occurs from point 2 to point 1 (second cycle) and from point 4 to point 3 (third cycle) is calculated as a negative value. If there is a net positive value, then the full healing potential suggested by Equation (3-41) is achieved. If, however, there is a net negative value, then the full healing potential is not reached, and the *healing potential factor-C* is less than one. The exact mathematical function used is shown in Equation (3-53).

Another correction factor, *healing potential factor-O*, is applied with the consideration that the healing potential generally reduces as the material becomes more damaged. In other words, even when the healing in a cycle occurs at newly damaged sites, i.e., when the total net damage is positive, the healing potential should nonetheless decrease as the damage grows. This situation is believed to be related to the fact that high damage levels represent both an increase in crack density as well as an increase in the average size of the cracks. As the size of the cracks increases, the overall potential for healing should be adjusted. The mathematical formulation for this healing potential factor is shown in Equation (3-54). The state variable used to track the value of *healing potential factor-O* is the maximum damage level (S) in the history and, thus, *healing potential factor-O* always suggests an overall drop in healing potential in damaged materials regardless of the type of damage, new or rehealed.

Figure 3-26 schematically shows the healing potential factors, and Figure 3-27 represents each healing potential factor that actually will be used in the FEP++ simulation. The *healing potential factor-C* and *healing potential factor-O* are more important, respectively, in a single cycle and in overall periods within the simulation; therefore, both factors should be considered together, as shown in Equation (3-55).

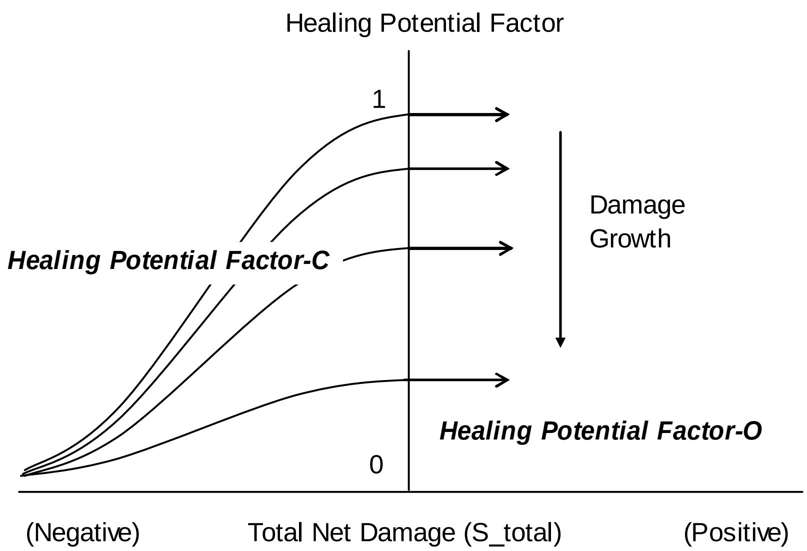

Figure 3-26. Effect of net damage growth on healing potential factors

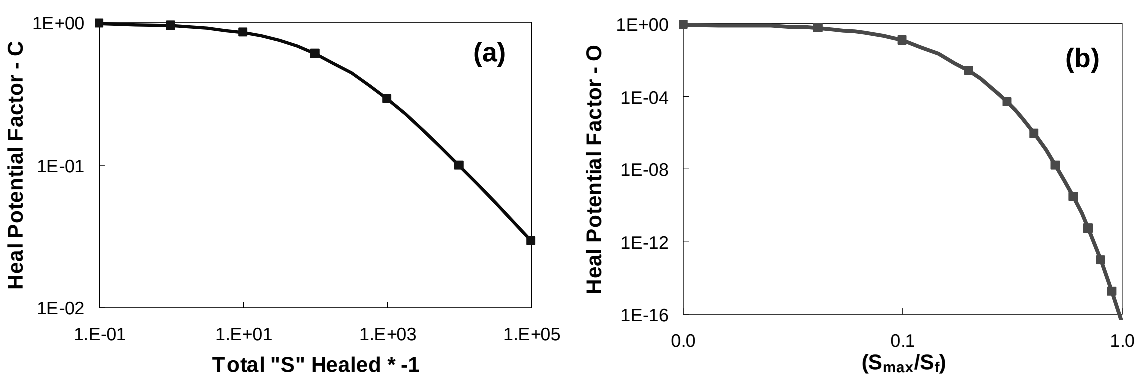

Figure 3-27. Healing potential factors

$$\Delta C_{Adjusted} = \Delta C_{Heal} * Healing\ Potential\ Factor \tag{3-52}$$

$$Healing\ Potential\ Factor - C = \begin{cases} 1 & S_t \geq 0 \\ \dfrac{1}{1+e^{y1+z1*\log(-1*S_t)}} & S_t < 0 \end{cases} \tag{3-53}$$

$$Healing\ Potential\ Factor - O = \frac{1}{1+e^{y2+z2*(S_{max}/S_f)}} \tag{3-54}$$

$$Healing\ Potential\ Factor = \begin{cases} \dfrac{1}{1+e^{y2+z2*(S_{max}/S_f)}} & S_t \geq 0 \\ \dfrac{1}{1+e^{y1+z1*\log(-1*S_t)}} * \dfrac{1}{1+e^{y2+z2*(S_{max}/S_f)}} & S_t < 0 \end{cases} \tag{3-55}$$

where

$S_{\max}$ = maximum S in history,
S_f = S at failure,
S_t = total net damage, and
$y1,\ y2,\ z1,\ z2$ = constant.

3.2.7 : Viscoplasticity

Viscoplasticity is commonly considered to be a material level factor related to rutting distress. However, as results from the NCHRP 9-30A project suggest, viscoplasticity may interact with the pavement structure to change the distribution of stress and strain within the pavement. Modifications to these distributions may drastically alter the potential for bottom-up cracking because these structural viscoplastic effects have been shown to be the most drastic near the pavement base.

To develop and implement a rigorous viscoplastic model into the FEP++ code would require substantial effort beyond the scope of this research. Therefore, viscoplasticity is considered in terms of the sensitivity ratio to viscoplasticity of the given material and structure, the so-called *damage factor* (DF). The DF is calculated by using a simple strain-hardening viscoplastic material model and pavement responses predicted using the FEP++ without damage for the pavement structure under evaluation.

To model the viscoplastic behavior of AC under tensile loading Uzan et al. (40) and Schapery (31) suggest a simple relationship, evidenced by Equation (3-56), which assumes that viscosity obeys a power law in viscoplasticity. Several researchers (5, 36) have shown that the model is applicable to monotonic behavior in tension.

$$\dot{e}_{vp} = \frac{g(s)}{h(e_{vp})}, \tag{3-56}$$

where

$g(s)$	=	stress function and
h	=	viscosity.

Assuming that h is a power law in the viscoplastic strain, Equation (3-57) becomes

$$\dot{e}_{vp} = \frac{g(s)}{Ae_{vp}^{\ p}}, \tag{3-57}$$

Where A and p are model coefficients. Rearranging and integrating yield

$$e_{vp}^{p} de_{vp} = \frac{g(s)\,dt}{A} \quad \text{and} \tag{3-58}$$

$$e_{vp}^{p+1} = \frac{p+1}{A}\int_0^t g(s)\,dt\,. \tag{3-59}$$

Raising both sides of Equation (3-59) to the $1/(p+1)$ power yields

$$e_{vp} = \left(\frac{p+1}{A}\right)^{\frac{1}{p+1}} \left(\int_0^t g(s)\,dt\right)^{\frac{1}{p+1}}. \tag{3-60}$$

Letting $g(s) = Bs^{q}$, and coupling coefficients A and B into coefficient Y, Equation (3-60) becomes

$$e_{vp} = \left(\frac{p+1}{Y} \right)^{\frac{1}{p+1}} \left(\int_0^t s^q dt \right)^{\frac{1}{p+1}}. \tag{3-61}$$

In the current work, the coefficients, p, q and Y, are pressure-dependent quantities.

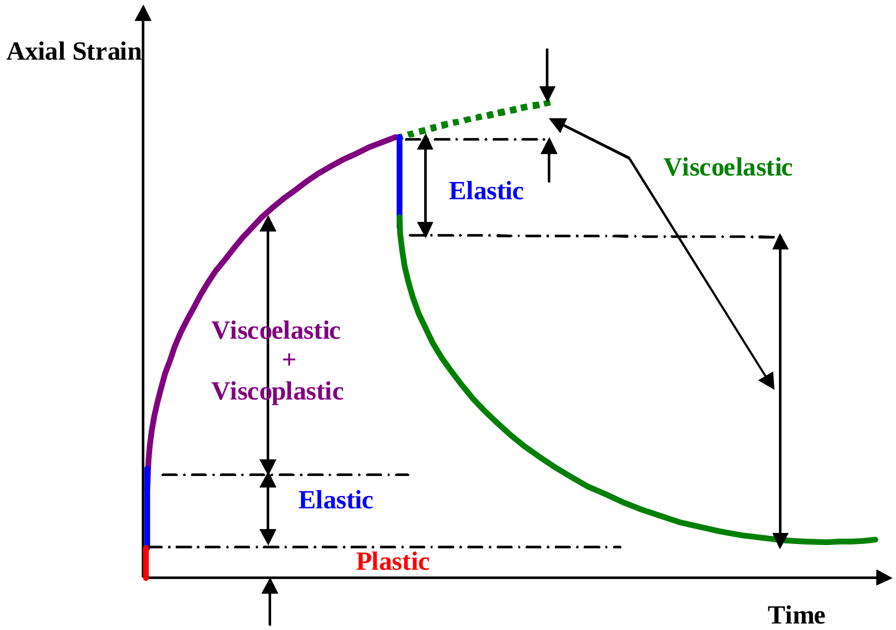

Figure 3-28. Strain decomposition from creep and recovery testing

Typically, viscoplastic models are characterized using creep and recovery tests. These tests allow relatively easy separation of the viscoplastic and viscoelastic components, as shown in Figure 3-28. However, it is difficult (if not impossible using some machines) to maintain zero load during the recovery period of the creep and recovery test in tension. Therefore, in tension, viscoplastic characterization uses constant rate tests in which the VECD model is used first to predict the viscoelastic strain. This viscoelastic strain is then subtracted from the measured strain to provide the viscoplastic strain that is needed for curve fitting to Equation (3-61).

3.2.8 : Thermal Stress

Another main source of TDC in asphalt pavements is thermal stress. Thermal stress can contribute to TDC in two ways: 1) through thermal fatigue, expressed by repeated, thermally-induced tensile stress at the pavement surface, which can gradually damage the pavement and contribute to surface-induced cracking; and 2) through acute thermal cracking, where very low temperatures cause sudden fracture of the pavement surface.

In evaluating thermal cracking and traditional bottom-up cracking, failure is determined when the maximum tensile stress exceeds the tensile strength of the asphalt concrete. However, the situation is more complicated in TDC analysis, because the stress induced at the surface of the pavement involves both normal and shear components.

The ability of the viscoelastoplastic continuum damage (VEPCD) model to accurately characterize the tensile behavior of AC under thermally induced loading has been confirmed by Chehab and Kim (6). Measured responses and fracture parameters from thermal strain-restrained specimen tensile (TSRST) strength tests were compared with those predicted using the VEPCD, VECD, and LVE models. Excellent agreement between the measured and predicted responses was found, especially in the VEPCD and VECD models, as explained in the next paragraph.

The stress histories predicted for the three cooling rates via the three models are plotted in Figure 3-29 as a function of time. Also plotted are the average measured stress values from all replicates tested at each rate. As is apparent from visual inspection, the stress predicted using the LVE model is greater than the measured stress, with the difference increasing as time increases and the cooling rate decreases. This discrepancy is due to the fact that the LVE model does not account for stress relaxation due to microcracking. The error between the VECD-predicted stress and the measured stress is much smaller than that for the LVE case for all cooling rates. Moreover, the error lessens with an increase in time and a decrease in cooling rate. The VEPCD-predicted stress matches the measured stress very well, with discrepancies being greatest at the slowest cooling rate. From a comparison of the predicted stresses among each other, it is evident that the VEPCD model yields the most accurate predictions, slightly better than the VECD model. Another important observation is that the rate of increase in VECD-predicted stress with time deviates from stress that corresponds to the measured and other predictions.

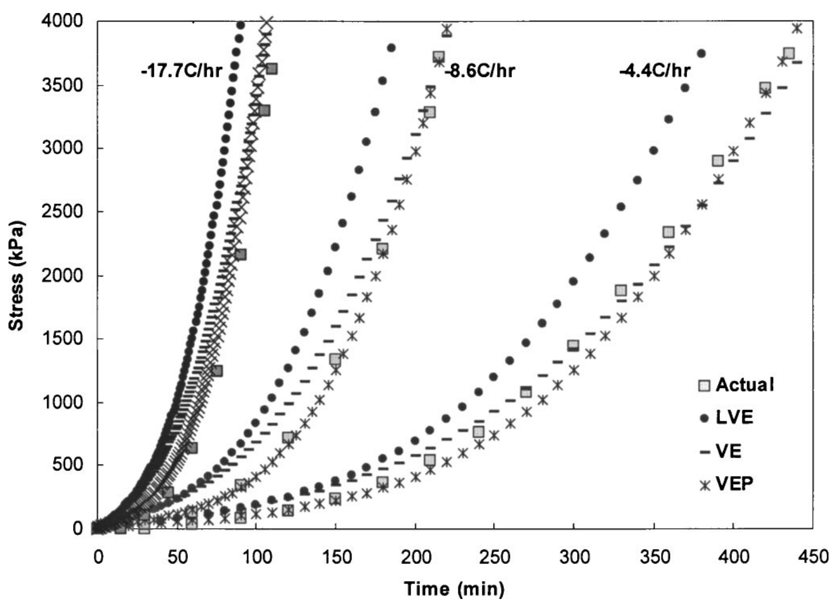

Figure 3-29. Average measured and predicted stress histories for different material models and cooling rates

3.3 : STRUCTURAL SUB-MODELS

To predict the pavement performance, the material sub-models must be converted to, or implemented into, structural models to consider the different structures, boundary conditions, climate conditions, etc. Consequently, three structural sub-models have been developed: 1) structural aging model, 2) damage factor (DF), and 3) temperature variation.

3.3.1 : Structural Aging Model

Details of the development of a material level aging model are provided in Section 3.2.4. The time scale used for the material level aging model corresponds physically only to that used for the top layer of a real pavement cross-section. To apply this model to different depths, the age of each sub-layer relative to that of the surface must be found. This goal is achieved by coupling the principles of the Global Aging System (GAS), first proposed by Mirza and Witczak (23), with an effective time concept. A ten-year-old pavement can serve as an example of the effective time concept whereby after ten years of service, the surface layer has aged ten years, but the material at a depth of three inches may behave as the surface layer behaved when the pavement was only four years old. In this example then, the effective time of the sub-layer three inches from the surface ten years after construction is four years. To compute the material properties of this sub-layer at year ten, material aging models described in Section 3.2.4.5 (from Figure 3-11 to Figure 3-13) can be used to find the value of the coefficients at four years.

Due to the time and resource limitations of this study, the GAS model is used to determine the effective time of a given pavement structure. The GAS model predicts the viscosity of the asphalt binder as a function of depth, mean annual air temperature (MAAT) representing the effect of geographical location, and rolling thin film oven (RTFO) binder viscosity. The effective time is determined by finding, for some physical time and depth, the time that gives the same viscosity for the binder at the pavement surface. A flow chart of the structural aging model, including the equiviscosity concept as well as the plot of effective time versus depth for a typical simulation, is shown in Figure 3-30.

As the GAS model is a function of the MAAT, the effective time varies for different climatic regions. To represent the wide range of conditions encountered in the United States, five regions are included in the study. These regions were selected based on the AASHTO climatic classification (1) and include: wet, freeze-thaw cycling (Washington, D.C.); wet, hard freeze, spring thaw (Chicago, Illinois); wet, no freeze (Tallahassee, Florida); dry, freeze-thaw cycling (Dallas, Texas); and dry, hard freeze, spring thaw (Laramie, Wyoming). Figure 3-31 is the plot of effective time at 20 years versus pavement depth for the five regions. The temperature in the legend is the MAAT for each region. It can be observed that the higher the MAAT, the higher the effective time at the same depth, which indicates that the aging effect is more significant for a higher MAAT region.

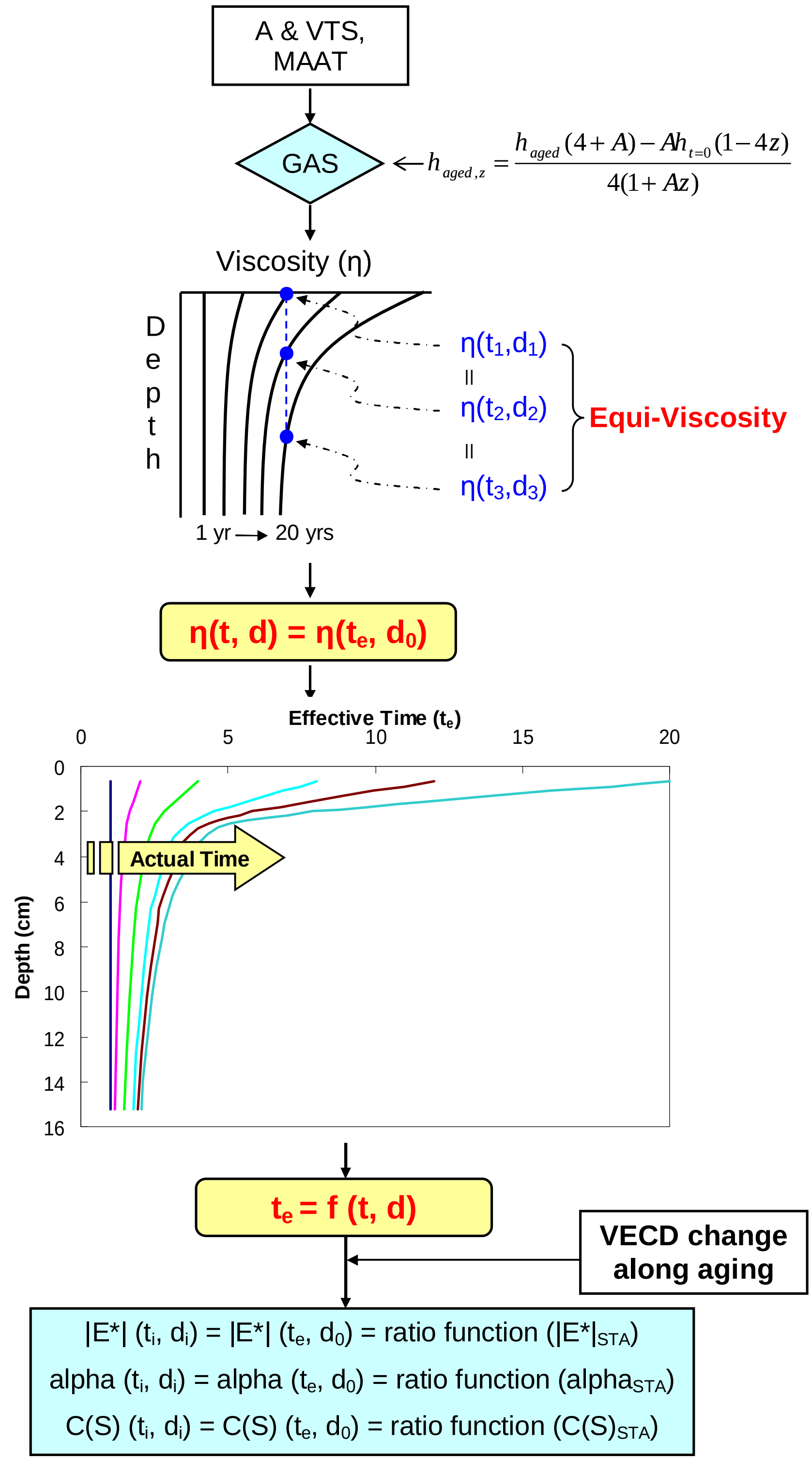

Figure 3-30. Structural aging model conceptual map

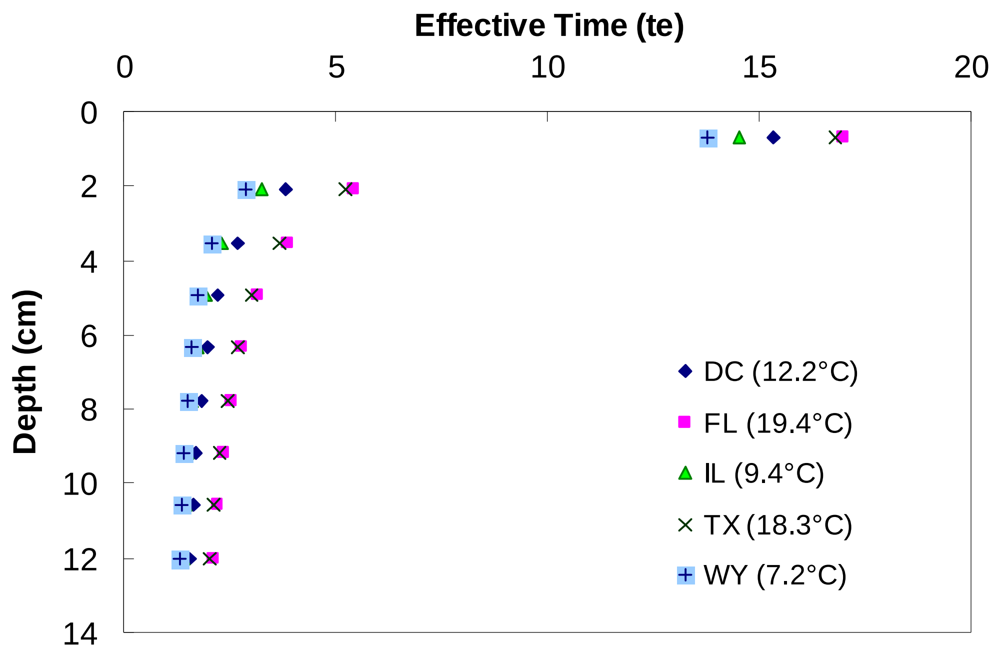

Figure 3-31. Effective time contours for various regions

3.3.2 : Damage Factor (DF)

The current framework uses the VECD material model and thus does not account for viscoplasticity. Ignoring the viscoplastic strain, however, results in an overprediction of stress, which in turn results in a spurious increase in damage, and therefore, an unrealistically rapid deterioration of the pavement. An approximated scheme used in the current framework to handle this problem is discussed next.

The viscoplasticity of a given material and structure is considered by applying the damage factor (DF). The DF is calculated by combining the simple strain-hardening viscoplastic material model discussed in Section 3.2.7 with the LVE stress and strain responses of the pavement under consideration. These responses are predicted by using the

FEP++ software and turning off the damage functionality. The linear strain responses are adjusted to account for viscoplasticity, and then these adjusted strain responses are used to find an effective viscoelastoplastic modulus. A second run of the FEP++ was performed using the effective modulus. Comparisons made between the responses of the first and second FEP++ runs reveal the sensitivity of the given pavement structure and materials to variations in viscoplastic strain. This sensitivity is reflected by a damage factor, which varies from 0 to 1. A value of 0 reflects a condition where the material is either very sensitive to structural viscoplastic effects and/or materially sensitive. Conversely, a value of 1 reflects a condition where the viscoplastic effects, both structural and material, are not very important. This latter condition may exist, for example, during winter.

The idea behind this scheme is that a pavement simulation is neither in control stress nor control strain mode but somewhere in between. In a stress-controlled situation, the strain computed in the simulation corresponds to the viscoelastic strain and fully contributes to damage. However, in a strain-controlled situation, the viscoelastic strain that contributes to damage is significantly weaker than the strain computed in the simulation. Thus, depending on which end of the spectrum the analysis lies, the amount of strain that contributes to damage varies significantly. To account for this unpredictability, the DF has been introduced and is defined as

$$DF = (1-b)\left(\frac{e_{ve}^{dmg}}{e_{fem}}\right) + b \ , \qquad (3\text{-}62)$$

where

e_{fem} = the strain computed by an FEP++ simulation,

e_{ve}^{dmg} = the strain contributing to damage, and
b = a factor that is 0 for control strain and 1 for control stress.

Thus, the problem of significant damage due to total strain can be handled by using the DF to scale the strain used in the damage calculation. The method used to calculate the DF is as follows.

As a first step, the stress and strain in the pavement are computed using viscoelastic analysis. Because the main interest is vertical cracking, the radial stress and strain are used in this analysis and denoted as s_{ve} and e_{ve}, respectively. Now, the viscoplastic strain, e_{vp}, can be approximated using the simple strain-hardening material model, Equation (3-61), and the viscoelastic stress computed in the previous step. Then, to approximate the structural effects of this viscoplastic strain, an effective viscoelastoplastic relaxation modulus is computed by scaling the Prony coefficients in Equation (3-5) using Equation (3-63), where E_i^{eff} are the effective modulus.

$$E_i^{eff} = \left(\frac{e_{ve}}{e_{ve} + e_{vp}} \right) E_i \tag{3-63}$$

A second analysis was performed, but instead of using the viscoelastic Prony coefficients, the effective viscoelastoplastic Prony coefficients were used. The stress and strain obtained from this analysis are referred to as the effective stress and strain and denoted as s_{ve}^{eff} and e_{ve}^{eff}, respectively.

The mode-of-loading factor b is then obtained by comparing the effective stress and strain (s_{ve}^{eff} and e_{ve}^{eff}) to the original stress and strain (s_{ve} and e_{ve}):

$$
\begin{aligned}
s_{eff} &= (1-b)\frac{E_{eff}}{E_{ve}} s_{ve} + b\, s_{ve} \\
e_{eff} &= (1-b)\frac{E_{eff}}{E_{ve}} e_{ve} + b e_{ve}
\end{aligned}
\quad , \tag{3-64}
$$

where b is a factor that is 0 for control strain and 1 for control stress. Equation (3-64) gives two values of b, and hence their average is taken as the degree of control stress:

$$
b_{avg} = 0.5\left(\left(1.0 - \frac{\dfrac{s_{ve}}{s_{ve}^{eff}} - 1.0}{\dfrac{E_i}{E_i^{eff}} - 1.0}\right) + \frac{\dfrac{e_{ve}^{eff}}{e_{ve}} - 1.0}{\dfrac{E_i}{E_i^{eff}} - 1.0}\right). \tag{3-65}
$$

Finally, the DF is given by

$$
DF = 0.5\left(\frac{\dfrac{s_{ve}}{s_{ve}^{eff}} - 1.0}{\dfrac{E_i}{E_i^{eff}} - 1.0} + \left(1.0 - \frac{\dfrac{e_{ve}^{eff}}{e_{ve}} - 1.0}{\dfrac{E_i}{E_i^{eff}} - 1.0}\right)\right). \tag{3-66}
$$

Overall flow chart of DF calculation using VE-FEP++ is shown in Figure 3-32. Note that because the strain-hardening viscoplastic model is valid only for tension, the DF is taken to be 1 for the region in which the radial stress is compressive.

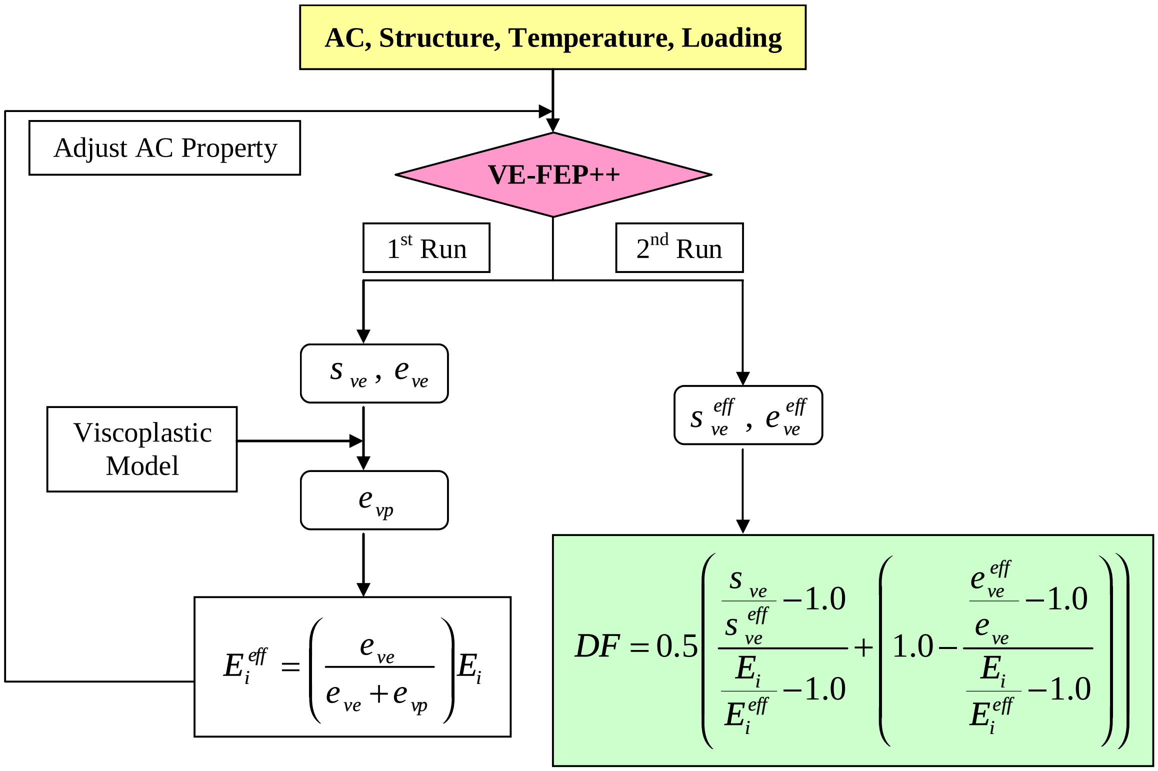

Figure 3-32. Flow chart of damage factor calculation

3.3.3 : Temperature Variation

The variation of temperature in a pavement has two effects: a change in stiffness of the AC and a change in the thermal stress due to thermal expansion of the material. Thermal stress is generated in the pavement depending on the boundary conditions. These two effects of temperature have been implemented in the FEP++.

The actual temperature variation that is used for the pavement performance prediction is generated from the EICM. Temperature profiles generated from the EICM are input directly into the FEP++ preprocessor.

3.3.3.1 : Temperature Profile

Five regions have been selected based on the six climatic zones identified by AASHTO (1) to represent the wide range of temperature variation in the United States. The regions selected for this analysis are the same as those used in evaluating aging. They are: wet, freeze-thaw cycling (Washington, D.C.); wet, hard freeze, spring thaw (Chicago, Illinois); wet, no freeze (Tallahassee, Florida); dry, freeze-thaw cycling (Dallas, Texas); and dry, hard freeze, spring thaw (Laramie, Wyoming). Figure 3-33 and Figure 3-34 show the variation of temperature and temperature rates in 2001 for each of the five regions; the numbers in the legend signify the month. It should be noted that each month's data are the averaged data for that month at 0.7 cm below the surface of the pavement. Although a detailed method for the pavement performance prediction is explained later, it has been determined that analysis on a monthly basis with three segments of a day might be appropriate for long term simulations, such as 20 years. Based on temperature and rate profiles, three segments of a day are indicated by vertical divisions in the plots, as follows: 5:00 AM – 1:00 PM (5:00 – 13:00) for the heating cycle; 1:00 PM – 9:00 PM (13:00 – 21:00) for the cooling cycle; and 9:00 PM – 5:00 AM (21:00 – 5:00) for the constant cycle. Temperature profiles according to depth can also be obtained for the same time segments and will be input for the simulation. Further, these segments generally follow daily traffic distributions.

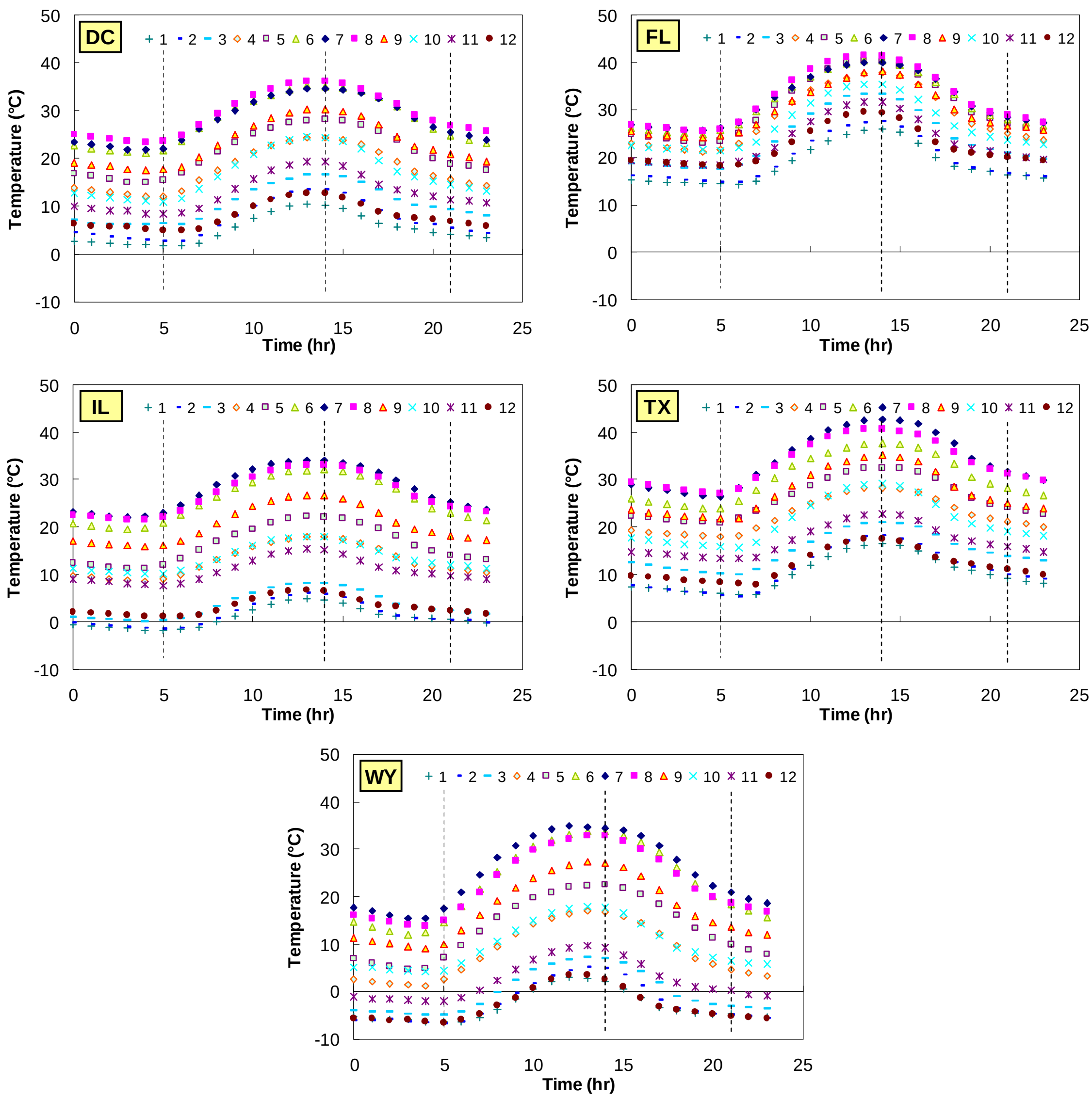

Figure 3-33. Temperature variation at 0.7 cm below pavement surface for 5 study regions

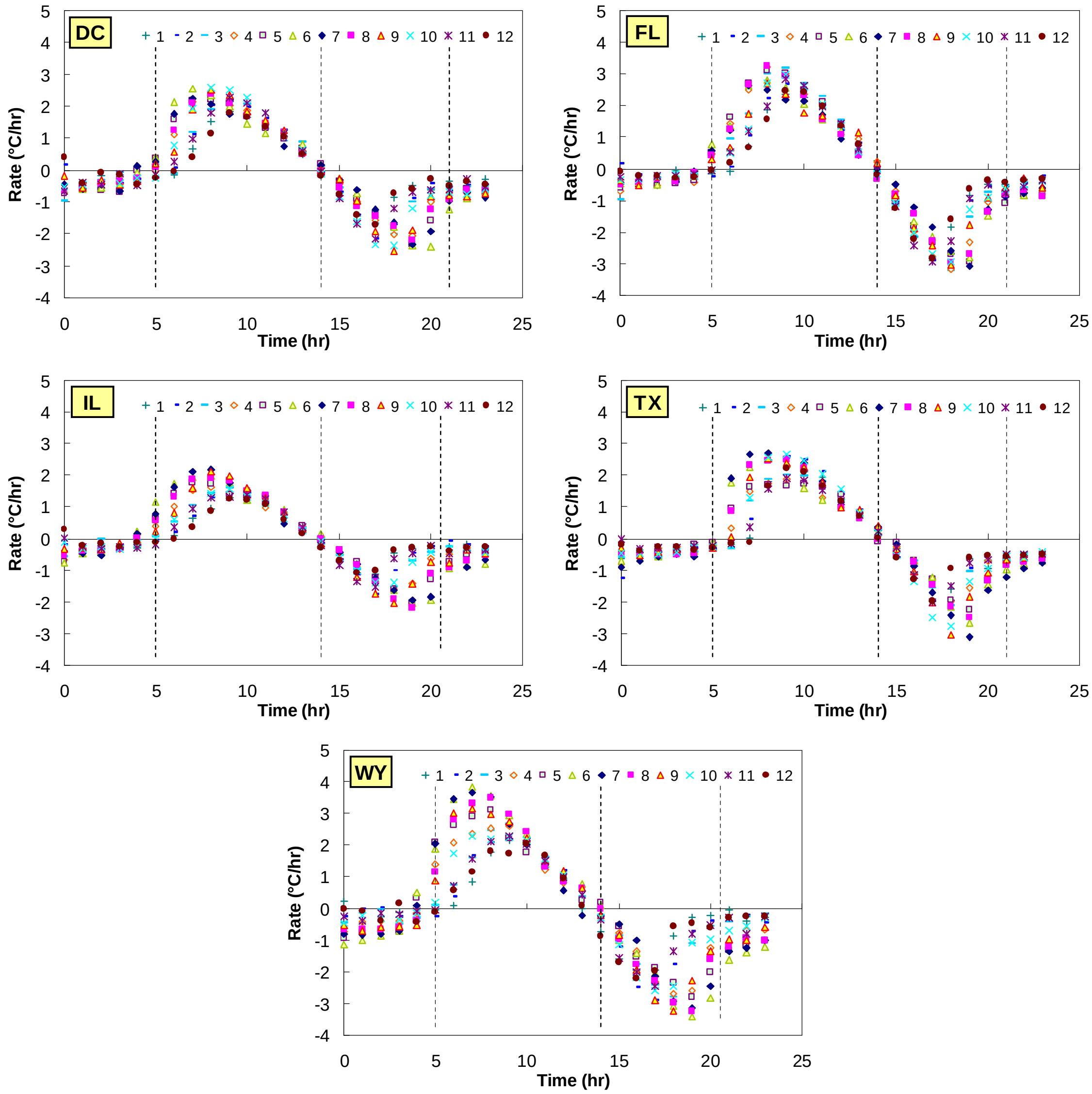

Figure 3-34. Temperature rate variation at 0.7 cm below pavement surface for 5 study regions

3.3.3.2 : Stiffness Change as a Function of Temperature

For material level modeling, the change in stiffness in AC due to temperature is taken into account using the concept of reduced time, which is discussed with regard to Equation

(3-9). The t-T shift factor is obtained from the characterization of the relaxation modulus of the material using dynamic modulus tests at different frequencies and temperatures. The reduced time is calculated with respect to a reference temperature and captures the history of temperature variations in the material.

In the computational implementation, all analyses were performed in terms of physical time, but the relaxation modulus was adjusted to the temperature of interest. This adjustment approach is similar in concept to the reduced time approach and is possible due to the use of a state variable formulation for stress and strain (36), and can be performed efficiently by adjusting the relaxation times in Equation (3-5) by

$$\hat{r}_i(t) = \frac{r_i}{a_T(t)}. \tag{3-67}$$

3.3.3.3 : Thermal Stress

Thermal stress in the material is incorporated by defining the mechanical strain, $e_m(t)$, as follows:

$$\{e_m(t)\} = \{e(t)\} - \{a\}(T - T_0), \tag{3-68}$$

where

$\{e_m(t)\}$	=	the strain in the material,
$\{a\}$	=	the coefficient of isotropic thermal expansion for the material in three dimensions,
T	=	the current temperature, and
T_0	=	the reference temperature at which there is no initial stress.

The constitutive law for a viscoelastic material undergoing damage is given as

$$\{s\} = [D]\{e_R^m\}, \tag{3-69}$$

where

$\{s\}$	=	the stress vector,
$[D]$	=	the stiffness matrix that is a function of damage, and
$\{e_R^m\}$	=	the vector of mechanical pseudo strain, computed using the state variable solution to Equation (3-12) (36).

3.4 : PERFORMANCE PREDICTION MODULE

The performance of a pavement can be characterized by predicting the damage accumulation in a pavement under the realistic conditions. In this research, the VECD-FEP++ which was originally coded by Guddati et al. (10) was utilized as a mean of predicting the pavement performance. To integrate the effects of variables that are important in TDC behavior, the sub-models presented in Section 3.2 and 3.3 have been incorporated into the existing VECD-FEP++, which was implemented by Thirunavukkarasu (35) with the development of extrapolation method.

3.4.1 : VECD FEP++

The VECD FEP++ is a finite element implementation of the VECD model proposed by Schapery and implemented in Hinterhoelzl and Schapery (11). The model assumes that a material is isotropic when undamaged and that damage growth under loading leads to local transverse isotropy; i.e., the material has a local axis of symmetry oriented along the maximum principal stress direction, which is perpendicular to the crack direction. This model is currently used in modeling tensile damage and has been found to adequately predict damage growth and experimental results until localization for uniaxial monotonic tensile loading. It offers the following modeling capabilities:

- It provides the damage progression in a viscoelastic material;
- It provides the three-dimensional state of stress and strain;
- It accounts for the effects of anisotropy in the material as a result of cracking in one direction.

The current framework of the VECD FEP++ is formulated for the axisymmetric case but can be extended easily to three dimensions. The finite element model (FEM) implementation enables the redistribution of stress in pavements that are being damaged, which is an important phenomenon, to be captured. The FEM implementation is also useful in studying the effects of layers with different stiffness values. By running the FEM simulation of a pavement for numerous cycles of fatigue loading, the progression of damage in the pavement over time may be observed, and critical points in the pavement that show early degradation can be noted. Using a suitable failure criterion that relates the damage parameter to the onset of cracking in a uniaxial test, the crack initiation points in the pavement under fatigue cracking can be predicted, and the life of the pavement can be better understood. Additionally, the program can be used in ranking the performance of pavements constructed from different asphalt mixtures.

The performance of a pavement can be characterized by predicting the damage accumulation and using a failure criterion to judge the state of the pavement. This evaluation can be achieved by using an FEM simulation with the VECD model over the period of interest. However, when the period of interest is in the order of years, it becomes computationally impossible to simulate the pavement performance. In these cases, approximate schemes are introduced so that the simulations run in a more time-efficient manner.

The FEP++ uses an extrapolation scheme that can significantly reduce the running time while still capturing the essential characteristics. The current scheme computes the damage caused by load and thermal variations at representative times in a day. These data are then extrapolated using a nonlinear scheme to obtain the total damage accumulation in a given month. This damage is then applied to the pavement as the initial condition for the next month's simulation. This process is continued for the entire simulation period. The extrapolation scheme presented in Section 3.4.3 was derived and implemented into VECD-FEP++ by Thirunavukkarasu (35)

3.4.2 : Traffic

Traffic loading is a complicated characteristic to quantify and include in pavement simulations. Complexities arise due to the statistical distribution of the numerous different axle types that are available, each with its own load level distribution. Predicting the exact distribution of these various vehicle loadings and their accompanying load level distributions is an imprecise science at best, and predicting the order of the loadings is impossible. Furthermore, predicting the sequential effects of different loading configurations becomes computationally time consuming. So, although it is true that, at any instant in time, the exact traffic history will determine the pavement performance, over time an averaging effect occurs, so the exact sequence of loading is not that critical. In light of this statistical effect and in order to simulate pavement performance in a reasonable amount of time, the concept of equivalent single axle loads (ESALs) is utilized.

For all of the subsequent pavement simulations, loading consists of ten million ESALs for the think pavement (12 in thickness of AC layers) and one million ESALs for the thin pavement (4 in thickness of AC layers) equally distributed over the three daily simulation periods (as defined in Section 3.3.3.1) and for a 20-year period. This distribution translates to approximately 41,700 loadings each month or 460 loadings for each of the three daily simulation periods for the thick pavement while 4,170 loadings each month or 46 loadings for each of the three daily segments for the thin pavement. Traffic growth factors and loading distributions other than uniform distribution could have been used, but these factors were not investigated due to time and resource limitations. Each load is assumed to last for 0.1 second and, as a consequence of the uniform loading distribution, the rest period between each loading is constant and equal to approximately 62.2 seconds for thick pavement and 622 seconds for thin pavement. These loading and rest times ensure compatibility between the total simulation time and the physical time.

The representative load consists of a single axle with an 80 kN (18 kip) load and tires inflated to 689 kPa (100 psi). It was assumed that the axle would be wide enough that the damage induced by each tire would be independent of that of the other. This assumption was verified through examinations of the damage contours that revealed little damage growth at distances of 0.5 m (1.6 ft.) from the wheel center. Due to this damage independence and due to the axisymmetric nature of the current work, the simulations can take advantage of symmetry and analyze a single side of the tire load. Currently, the effect of wheel wander is not considered in the simulations.

3.4.3 : Extrapolation

The basic idea behind extrapolation is to use the damage growth law to obtain an approximate expression for the damage growth rate. The growth law is given by

$$\frac{\partial S}{\partial t} = \left(-\frac{\partial W_R}{\partial S}\right)^a = \left(-\frac{\partial C}{\partial S}\right)^a \frac{e_R^2}{2}, \tag{3-70}$$

where

W_R = pseudo strain energy density function, $W_R = \frac{1}{2}(e_R)C$,
e_R = pseudo strain,
t = total duration of a load cycle,
C = pseudo stiffness, and
S = damage.

Using a change of variables and Equation (3-70), the growth rate of the pseudo stiffness can be written as

$$\frac{\partial C}{\partial t} = \frac{\partial S}{\partial t}\frac{\partial C}{\partial S} = \left(\frac{\partial C}{\partial S}\right)^{a+1} \frac{e_R^2}{2}, \tag{3-71}$$

or equivalently as

$$\frac{\partial C}{\partial n} = \int_o^t \left(\frac{\partial C}{\partial S}\right)^{a+1} \frac{e_R^2}{2} dt. \tag{3-72}$$

The pseudo stiffness and damage parameters, C and S, are related by

$$\ln(C) = aS^b, \tag{3-73}$$

which, upon differentiation, yields

$$\frac{\partial C}{\partial S} = a^{1/b} bC\left(\ln C\right)^{1-1/b}. \tag{3-74}$$

Finally, assuming the pseudo strain, e_R, remains constant during a cycle,

$$\frac{\partial C}{\partial n} = AC^{(a+1)}\left(\ln C\right)^{(a+1)\left(1-1/b\right)}, \tag{3-75}$$

where A is the constant over the duration of the cycle.

The above relationship can be solved numerically using the results from the FEM simulation as the initial condition to obtain an approximate value of the pseudo stiffness and, hence, the damage, at the end of the extrapolation period. The equations for the numerical scheme to solve Equation (3-75) are given by

$$\begin{aligned}
C_{i+1}^{end} &= C_{i+1}^{begin} + A\left(C_{i+1}^{begin}\right)^{(a+1)}\left(-\ln\left(C_{i+1}^{begin}\right)\right)^{(a+1)(1-1/b)}, \\
C_{i+1}^{begin} &= C_i^{end} + \Delta C_i^{heal}, \\
A &= \frac{C_i^{end} - C_i^{begin}}{\left(C_i^{begin}\right)^{(a+1)} \times \left(-\ln\left(C_i^{begin}\right)\right)^{(a+1)(1-1/b)}},
\end{aligned} \tag{3-76}$$

where

C_i^{begin}	=	the pseudo stiffness at the beginning of cycle i,
C_i^{end}	=	the pseudo stiffness at the end of cycle i, and
ΔC_i^{heal}	=	the recovered stiffness due to healing in cycle i.

3.4.4 : Damage Calculation Summary

A flow chart of the total damage calculation process, including extrapolation, is shown in Figure 3-35. This flow chart outlines the combination of elements discussed previously:

traffic loading, thermal considerations, damage factor, daily divisions for damage calculation, healing, etc. To verify the accuracy of some of the simplifications, particularly the extrapolation scheme, a simulation was performed using the FEP++ software without any extrapolation. In a real pavement simulation, the number of cycles simulated in an analysis step would be closer to 13,000, but predicting this many cycles without extrapolation would require a significant amount of time. Instead, the simulation was carried out for only about 1,300 cycles, and comparisons were made at this number of cycles. The results of two different cases, (a) a healing dominant case and (b) a damage dominant case, are shown in Figure 3-36, along with the results based on the extrapolation. To compute the extrapolated value, the damage growth in the selected cell for the first cycle was extracted from the VECD-FEP++ analysis and input into a spreadsheet-implemented version of the extrapolation algorithm. The spreadsheet-based algorithm is used here for convenience only. In a full simulation, the extrapolation process is completed automatically in the VECD-FEP++ software. It is seen from Figure 3-36 that the extrapolation algorithm effectively matches the output from the complete analysis at 1,300 cycles. Also seen in Figure 3-36, the agreement between the reference simulation and the extrapolated simulation decreases as the number of cycles increases; however, coincident with this increasing disagreement is a tendency for the pseudo stiffness to approach an asymptotic value. Thus, it is expected that the differences observed in the extrapolation to 1,300 cycles would be similar to the differences observed at 13,000 cycles. Direct proof of this hypothesis could not be performed due to the time necessary to create a reference simulation for 13,000 cycles. Note that in this simulation the thermal loading is not included because the time basis of one cycle for mechanical loading and thermal loading is different, i.e., 62 second versus 1 hour, and therefore, the thermal model and its extrapolation scheme need to be separately developed and evaluated, which will be presented in Section 3.4.5.

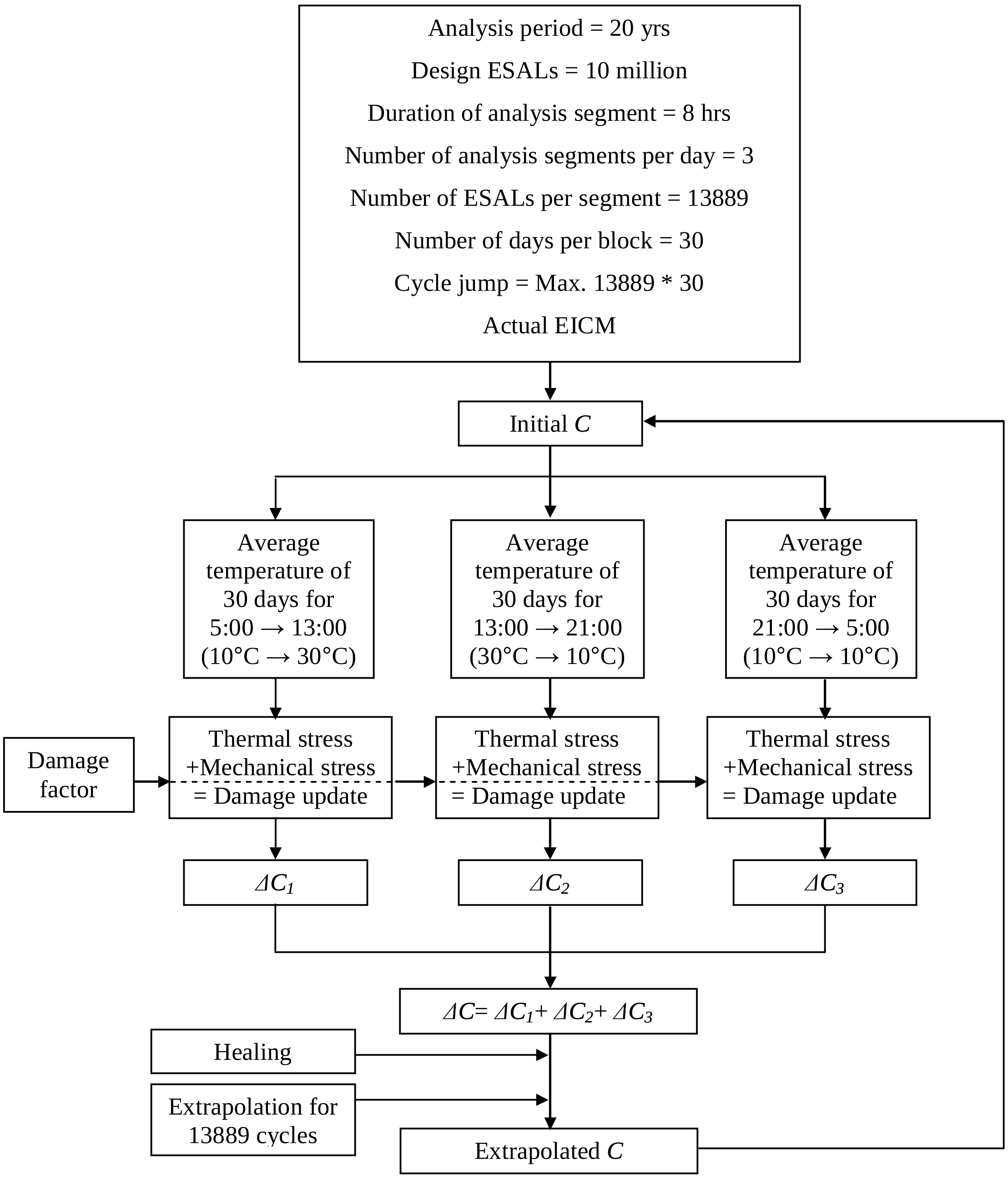

Figure 3-35. Extrapolation flow chart

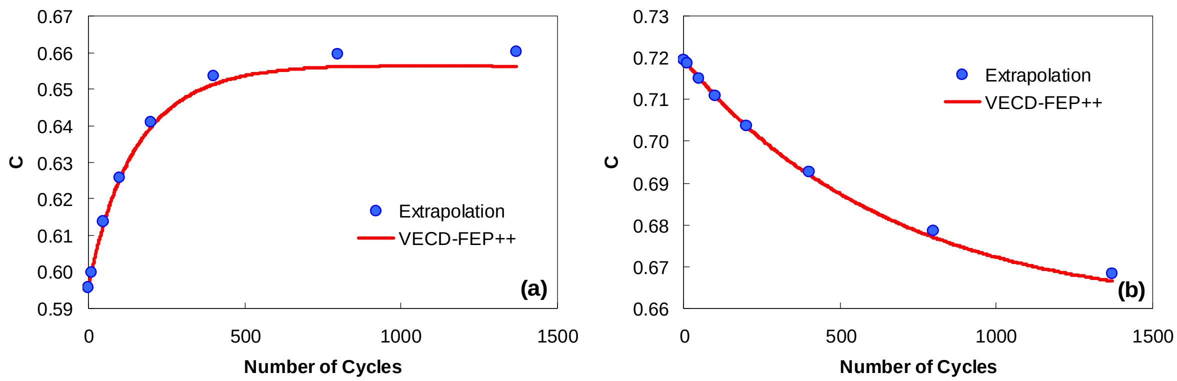

Figure 3-36. Effect of extrapolation calculation on predicted damage growth: (a) healing dominant case and (b) damage dominant case

3.4.5 : Thermal Model

The extrapolation algorithm shown in Section 3.4.4 was developed mainly to address large traffic volumes over the pavement life. Similarly, thermal loading, which is due to temperature variations according to time and depth, also occurs throughout the entire pavement life. Therefore, the extrapolation method for thermal loading needs to be developed and combined with the extrapolation algorithm for mechanical loading. This section presents the development and validation of the thermal model and the extrapolation method.

3.4.5.1 : Full-time Thermal Loading Simulation

A full-time thermal loading simulation was performed to validate the thermal extrapolation model and investigate some factors that may affect the thermal stress and damage calculations. These factors include a reference temperature (or so-called *stress-free temperature*), the reference time for which the reference temperature reaches to the actual start temperature of the simulation, and the number of time-steps for the reference time. Full-time simulation means that the actual hourly temperature obtained from the EICM is used as the input to calculate the thermal stress and damage for each time-step, which is one hour in this simulation, and no extrapolation is included.

Because there are no laboratory or field data to verify the results of the full-time thermal loading simulation, it was assumed that the cumulative damage from the full-time simulation using certain temperature profiles would be the same after a long period of time, i.e., more than a few years, regardless of whether the simulation started from noon or midnight in a day, or from June or December in a year. Therefore, eight sets of simulations were run with two extreme temperature profiles (Florida and Wyoming), two different starting seasons (June and December), and two different starting times (noon and midnight). For this simulation, thin pavements consisting of a 3-inch AC layer over infinite subgrade were used because temperature variations according to depth are not significant below 3 inches from the surface. The temperature profile and the reference temperature for each case are shown in Figure 3-37. The temperature at the starting time for each case is considered to be the reference temperature, and such reference temperature is consistent for the entire simulation.

The reference temperature, or so-called ***stress-free temperature***, is an important variable in the thermal model because the thermal strain is calculated directly based on the difference between the reference temperature and the current temperature, as defined in Equation (3-68). The reference temperature, however, is also a conceptual temperature, which is almost impossible to measure because it may vary according to time, depending on conditions that the pavement may encounter.

Figure 3-38 presents the damage accumulation due to thermal loading for the eight different cases. From the results it was found that different starting times result in different damage accumulations for the same temperature profile; in particular, the case that starts at noon in June for Florida (FL-Jun-Noon) deviates significantly from other cases with the same temperature profile. Such discrepancy proves that the reference temperature is critical in the thermal model.

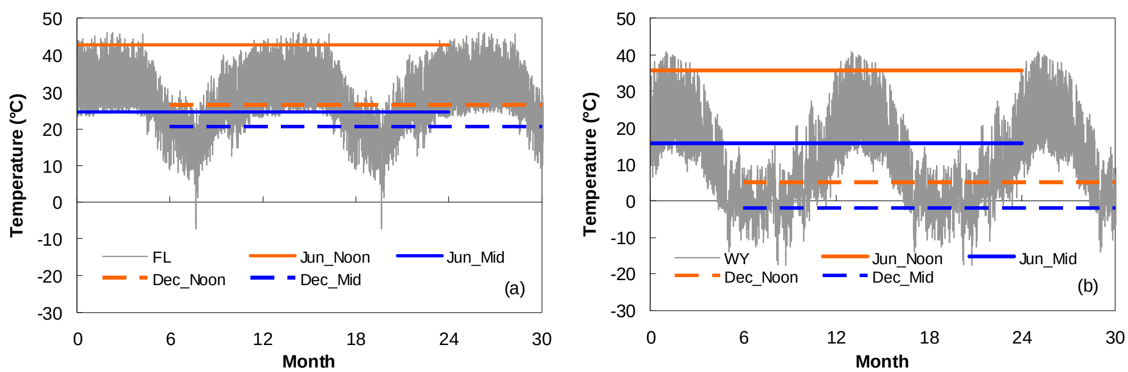

Figure 3-37. Temperature profiles and reference temperatures for: (a) FL and (b) WY

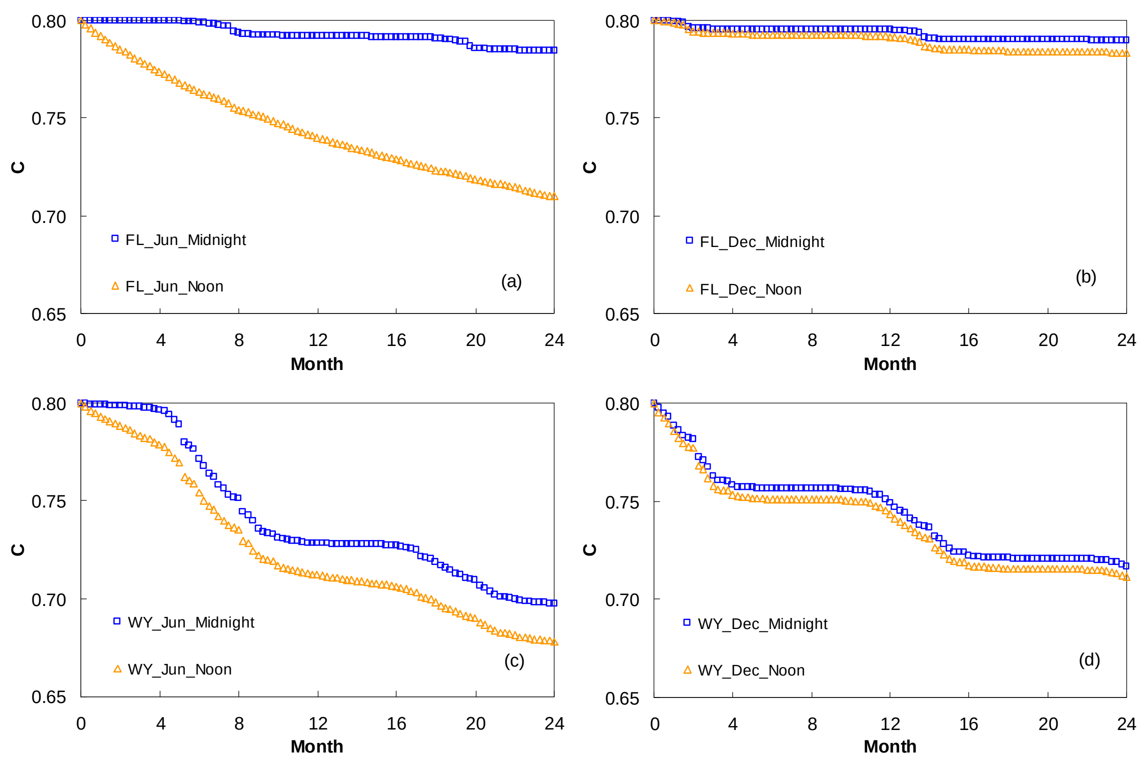

Figure 3-38. Full-time simulations of thin pavements starting from: (a) FL-Jun, (b) FL-Dec, (c) WY-Jun, and (d) WY-Dec

To reduce the time needed to run the simulations, a single element simulation was used for the thermal model development. It was expected that the single element simulation would capture the overall trend because stress and strain under thermal loading are not as complicated as under mechanical loading. Even though the single element simulation cannot capture some effects that may exist in an actual pavement structure, such as interactions between layers, boundary conditions, Poisson's ratio, and so on, it was assumed that those effects may be insensitive for the thermal loading condition.

To verify if the single element simulation could capture the overall trend of the thin pavement simulation, four cases from the thin pavement simulations were selected and run with the same temperature profile and reference temperature. The size of a single element is 1.4 cm by 1.4 cm, which is the same size of one element in the thin pavement simulation. Both of the horizontal ends are fixed, but the element is free to move up. Figure 3-39 compares the results from the single element and thin pavement simulations and, as expected, the overall trend was properly captured by the single element simulation. Therefore, it was decided to use the single element simulation to investigate the various factors.

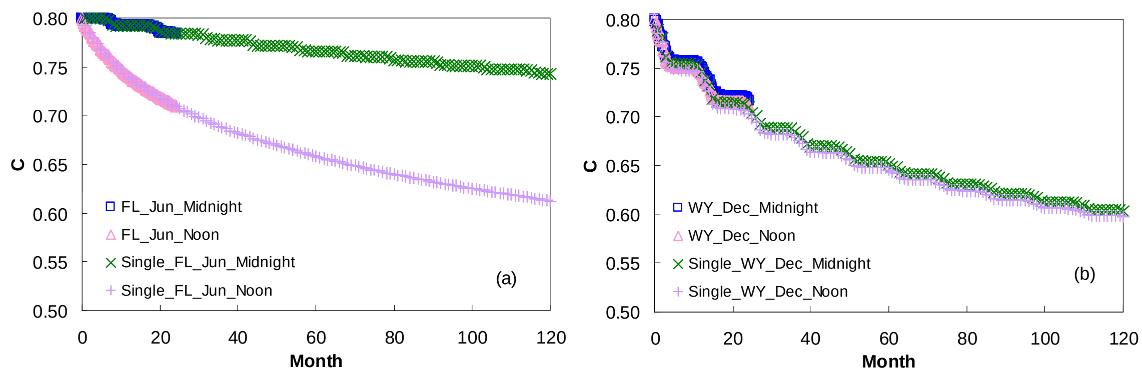

Figure 3-39. Full-time simulations of thin pavements and single elements starting from: (a) FL-Jun, (b) WY-Dec

From the results shown in Figure 3-39, it was found that the constant reference temperature for the entire pavement life is not appropriate, and therefore, the varying reference temperatures according to time required further investigation. The idea behind a varying reference temperature is that the thermal stress generated by the temperature variation should relax after a certain time, and hence, the stress-free condition is re-introduced. However, relaxation of thermal stress is completely dependent on all conditions, such as temperature, material, structure, the continuous application of thermal loading, etc.

Therefore, it is impossible to find or measure the relaxation time of the thermal stress. It could be one hour, one day, or one month, depending on the various factors.

With such uncertainty in terms of the reference temperature, a systematic analysis was performed to assess varying reference temperatures. The concept of moving averages for various periods was utilized to create varying reference temperatures, as shown in Figure 3-40 (a) and (b). In this simulation, the reference temperature was changed for each time-step, i.e., one hour; therefore, this approach was deemed impractical for implementation into the extrapolation scheme. Because the extrapolation scheme for mechanical loading is on a one-month basis, a more practical approach here is to take the average temperature for one month as the reference temperature for the next month, as shown in Figure 3-40 (c) and (d).

Figure 3-41 compares the damage accumulation for the various cases of varying reference temperatures. The results from the various approaches are not particularly sensitive as compared to those shown in Figure 3-38. Therefore, a 30-day constant average was selected as the reference temperature for the thermal model.

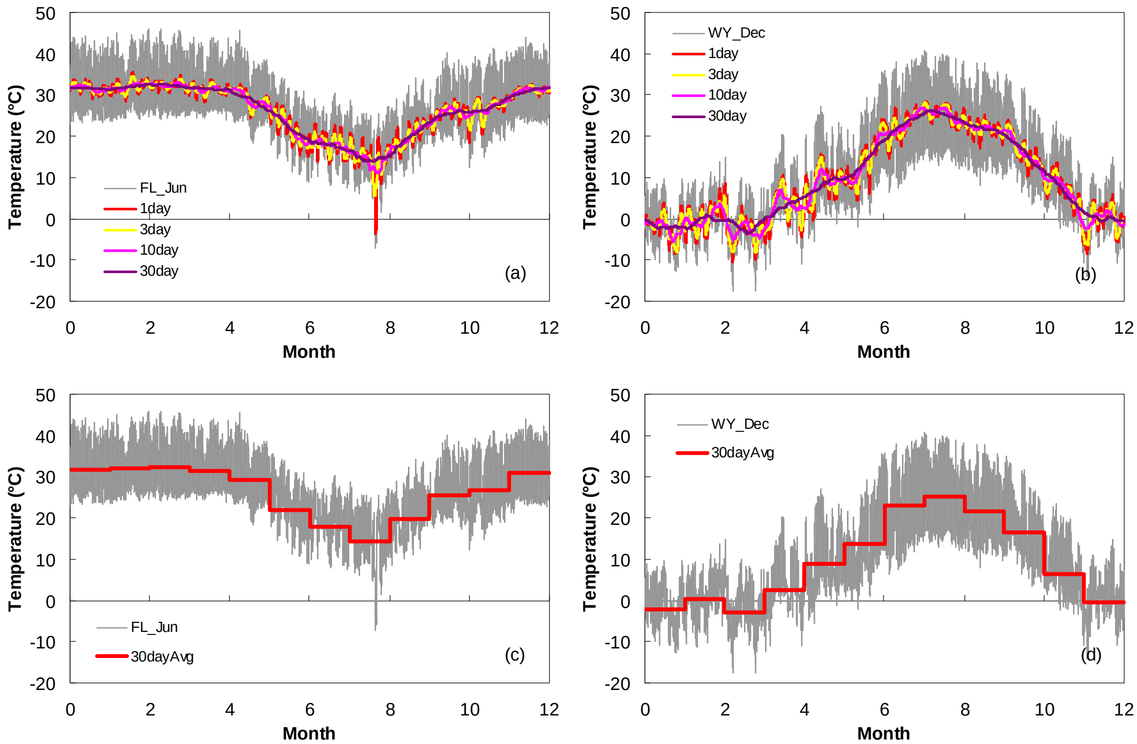

Figure 3-40. Temperature profiles and varying reference temperatures: (a) and (b) moving average for FL and WY, respectively; (c) and (d) 30-day constant average for FL and WY, respectively

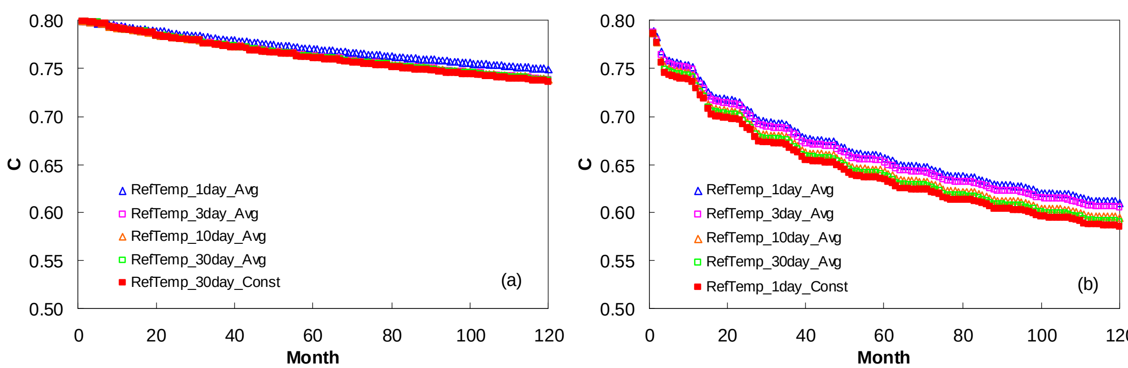

Figure 3-41. Varying reference temperature effect starting from: (a) FL-Jun and (b) WY-Dec

Other factors that need to be studied are the reference time for which the reference temperature reaches to the starting temperature of the simulation and the time-step for that reference time. In the previous simulation (Figure 3-41), the reference time was not considered, i.e., at the starting time of the simulation, there was no stress generated by the difference of the reference temperature and the starting temperature. Hence, a series of simulations with various reference times and numbers of time-steps was performed. The reference temperature for these simulations was determined using the 30-day constant average concept. As shown in Figure 3-42, the reference time appears to be slightly sensitive, and the number of time-steps needed for the damage calculation is not sensitive. This finding could be due to the fact that the temperature varies linearly from the reference temperature to the starting temperature. Based on the fact that the reference time and the time-step are not sensitive and that a 30-day constant average temperature was decided to serve as the reference temperature, a 15-day reference time and one time-step were selected for the final simulation.

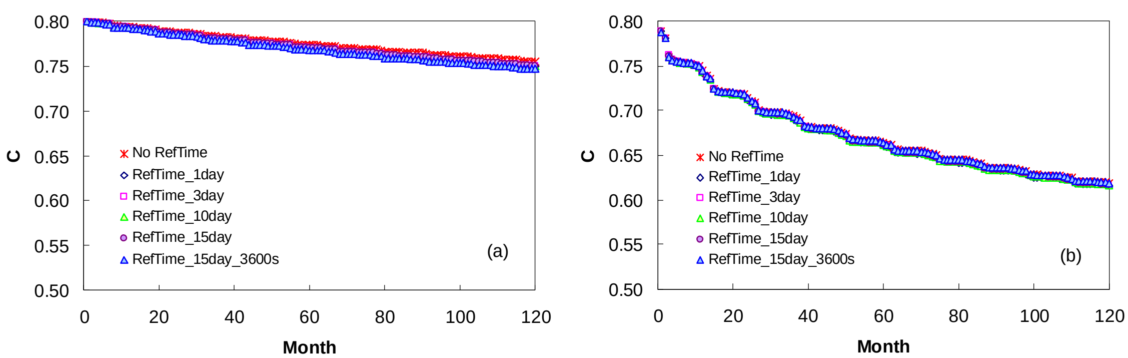

Figure 3-42. Various reference time effects using the 30-day constant average concept for the climates starting from: (a) FL-Jun and (b) WY-Dec

With the approaches determined based on the sensitivity analysis, the full-time thermal loading simulation was performed using the single element simulation and the results are shown in Figure 3-43. For these simulations, two different starting months (Jun versus Dec) for both FL and WY temperature profiles were utilized. As decided from the sensitivity studies, the reference temperature was a 30-day constant average temperature of the previous month and a 15-day reference time with one time-step was applied. As seen in Figure 3-43, especially for the Wyoming temperature profile, the damage accumulations for the different starting times are different for the initial months, but both cases (FL and WY) show almost the same damage level at the end of ten years of simulation. These results will be utilized for the validation of the thermal extrapolation model.

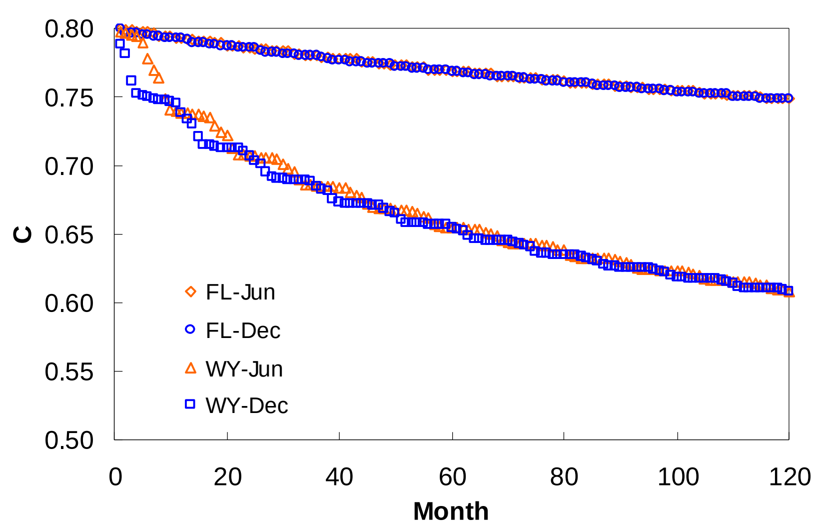

Figure 3-43. Representative full-time thermal loading simulation results

3.4.5.2 : Extrapolated Thermal Loading Simulation

Figure 3-44 shows the proposed extrapolation scheme that presents how the thermal stress and damage are calculated and how the thermal loading is combined with the mechanical loading. This schematic representation was developed based on the method shown in Figure 3-35. First, the thermal stress due to temperature change in a segment during the negative time-step is calculated. The thermal stress is combined with the mechanical stress for 0.1 second, and the combined stress is then used to calculate the damage. After 0.1 second, the mechanical stress is released, but the thermal stress still remains and accumulates the damage. In the same way, the damage from the other two segments is calculated, and the damage accumulation results for all three segments are summed and then extrapolated by the amount of traffic to obtain the damage for a month.

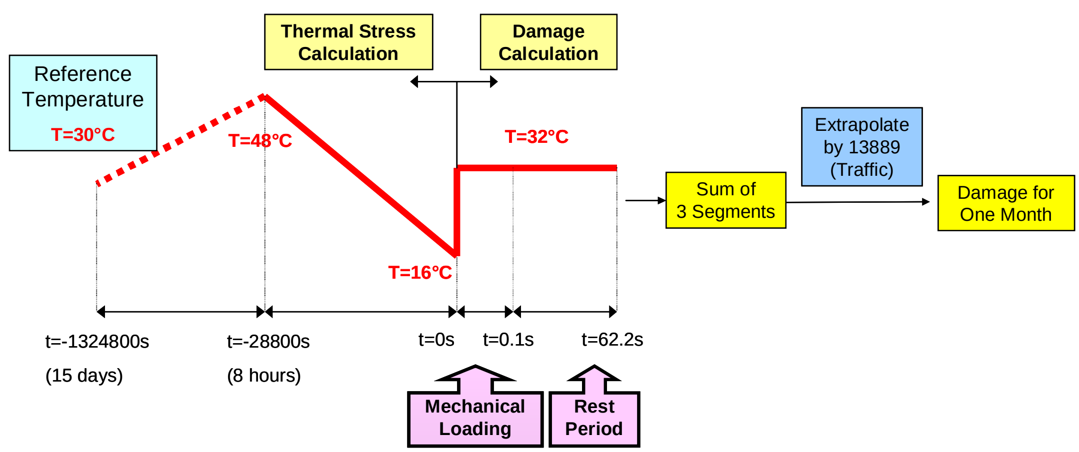

Figure 3-44. Extrapolation scheme for thermal and mechanical loading

In Figure 3-44, the temperature profile for thermal stress calculation, i.e., between t = -28800 sec and t = 0 sec, could be arithmetic average or based on the weighted average, whereas the temperature for damage calculation, i.e., between t = 0 sec and t = 62.2 sec, could be the end temperature of the temperature profile for thermal stress calculation (referred to as End) or the average temperature of the temperature profile for thermal stress calculation (referred to as Avg). These two options have been investigated to determine which approach yields the same results for the full-time simulation.

In the current simulation extrapolation scheme, the temperature for a given month is averaged for each of the time segments identified in Section 3.4.4. This method is perfectly acceptable for computing the stress and damage due to mechanical loading, but could yield erroneous thermal damage results because it effectively smoothes some of the extreme events. The thermal stress-related damage calculations are much more sensitive to changes in temperature than the mechanical stress-related damage calculation, because these damage calculations are directly proportional to the temperature raised to the VECD damage power, a. This proportionality can be observed by substituting the thermal strain, Equation (3-68), into the pseudo strain calculation, Equation (3-12), and then combining the results with the derived evolution law, which is part 1 of Equation (3-28). Conversely, the temperature dependence for mechanical damage enters indirectly into the constitutive model by changes in reduced time in the calculation of the pseudo strain. This indirect entry does not mean that the mechanical damage is not sensitive to temperature, only that it is less sensitive to temperature than is thermal damage.

To compute the thermal damage more accurately, the theoretically observed proportionality between thermal damage and temperature raised to the VECD a was used. Equation (3-77) shows the averaging function that was applied to generate the weighted average temperature. Figure 3-45 provides a comparison between the average and weighted average temperature values computed for a daily temperature cycle. In this figure, the lines represent the daily temperature cycles for the 31 days of December for Laramie, Wyoming. In Figure 3-45, the circles represent the mathematical average temperature, and the squares represent the weighted average temperature. It is seen from Figure 3-45 that the overall average temperatures are not that different from each other.

$$T_{WA} = \left(\frac{\sum_{i=1}^{N} T^a}{N} \right)^{1/a} \tag{3-77}$$

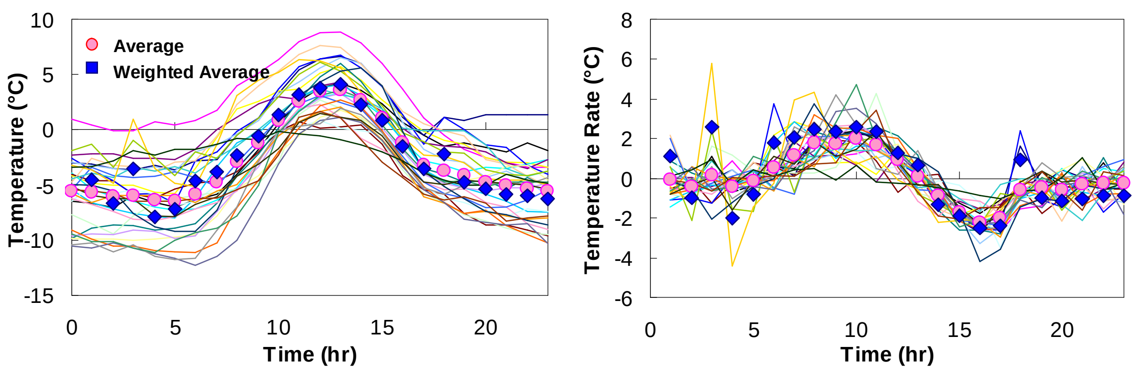

Figure 3-45. Original vs. weighted average temperature and temperature rates for WY-Dec

Based on the findings from the full-time simulation, the effects of reference temperature, time, and time-step in the extrapolated thermal loading simulation were evaluated, and the results are shown in Figure 3-46. The effects of such factors on the extrapolated simulation appear more sensitive than they do on the full-time simulation. However, considering engineering reasonableness and the practicality of the time needed to run the simulations, it was decided to employ the methods used in the full-time simulation.

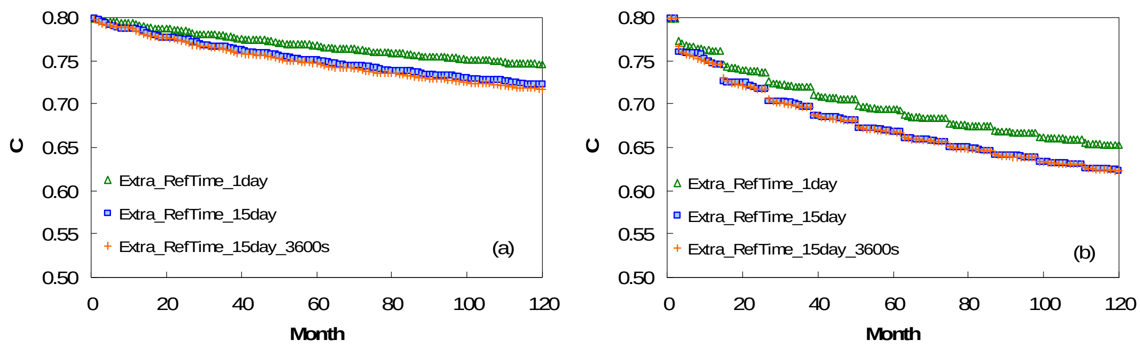

Figure 3-46. Effects of reference temperature, time, and time-step in the extrapolated thermal loading simulation starting from: (a) FL-Jun and (b) WY-Dec

To determine the appropriate thermal extrapolation model, a set of simulations was run for the Florida and Wyoming temperature profiles. Four different cases were created by using a combination of arithmetic and weighted average methods for the thermal stress calculation portion (during the negative time-steps) and using the end or average temperatures for the damage calculation portion (during the rest periods). The reference temperature used is the average temperature of the previous month, and the reference time is 15 days with one time-step. To directly compare the full-time simulation results shown in Figure 3-43, the single element simulation was utilized. Damage accumulations for the four cases are plotted together with the results of the full-time simulation in Figure 3-47. As seen in the results for the Wyoming temperature profile, the combination of the weighted average temperature for the thermal stress calculation and the average temperature for the thermal damage calculation is perfectly matched to the full-time simulation result. However, in the Florida temperature profile, the full-time simulation result is close to the combination of the arithmetic average and the end temperature method, or to the middle of the end and average temperature method using the weighted average temperature.

To discern whether certain temperature profiles cause such discrepancies in matching the combinations of the extrapolation schemes, both the Florida and Wyoming temperature profiles were shifted down or up so that new sets of temperature profiles, with different yearly average temperatures and the same daily temperature fluctuations, were created. The difference in the yearly average temperatures between Florida and Wyoming is 30°F. In other words, the original FL temperature profile was shifted down by 30°F, whereas the original WY temperature profile was shifted up by 30°F. The same sets of combinations using the newly created temperature profiles were simulated, and the results are provided in Figure 3-48. The opposite trend was found. For the FL-30°F shifted down profile, the full-time simulation was perfectly matched to the combination of the weighted average and the average temperature method, whereas for the WY-30°F shifted up profile, the full-time simulation was situated in the middle of the end and average temperature method using the weighted average temperature. This trend could be caused by different effect of errors from averaging temperature for the extrapolation in warm and cool temperature profiles. Nevertheless, it was decided that the combination of the weighted average temperature for the thermal stress calculation and the average temperature for the damage calculation is acceptable as the thermal and mechanical extrapolation methods. This combination has the following advantages: 1) overall, it is perfectly matched to the full-time simulation for the cool temperature profile (WY), which creates severe thermal damage; 2) theoretically, the weighted average temperature captures daily temperature fluctuations; and 3) the average temperature used for the damage calculation is more representative than the end temperature.

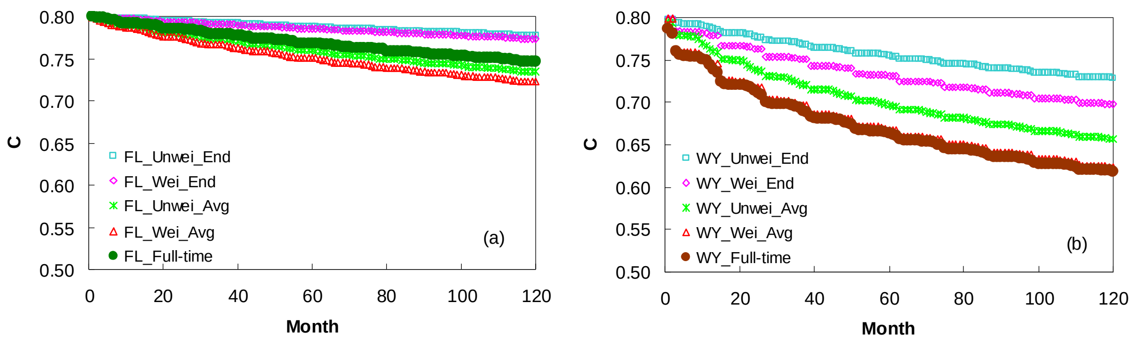

Figure 3-47. Comparison of the extrapolated simulation and the full-time simulation: (a) FL and (b) WY

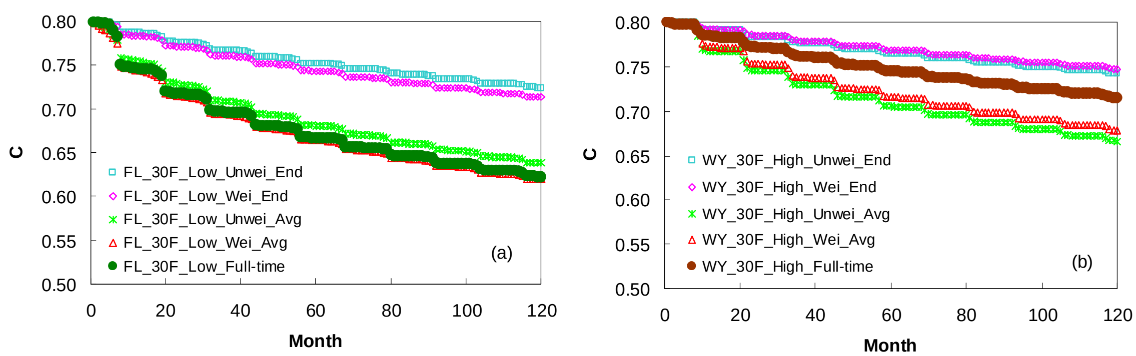

Figure 3-48. Comparison of the extrapolated simulation and the full-time simulation: (a) FL – 30°F shifted down and (b) WY – 30°F shifted up

With the thermal extrapolation scheme developed using the single element simulation, the final sets of the simulation were run for a thin pavement structure. For these simulations, two climate conditions, Florida and Wyoming, and two asphalt mixtures, Control and SBS from the ALF pavements (mixture information can be found in Section 4.1), were utilized. Figure 3-49 (a) and (b) present the comparisons between the full-time simulation and the extrapolated simulation for the Control mix and SBS mix, respectively. Note that the damage accumulation was determined from the first top layer, which shows the most significant damage due to the largest variation in temperature. The overall trends are the same for the single element simulation results. The SBS mix exhibits much less thermal damage than the Control mix, especially in the Wyoming temperature profile. This result is expected because the SBS mix is softer than the Control mix.

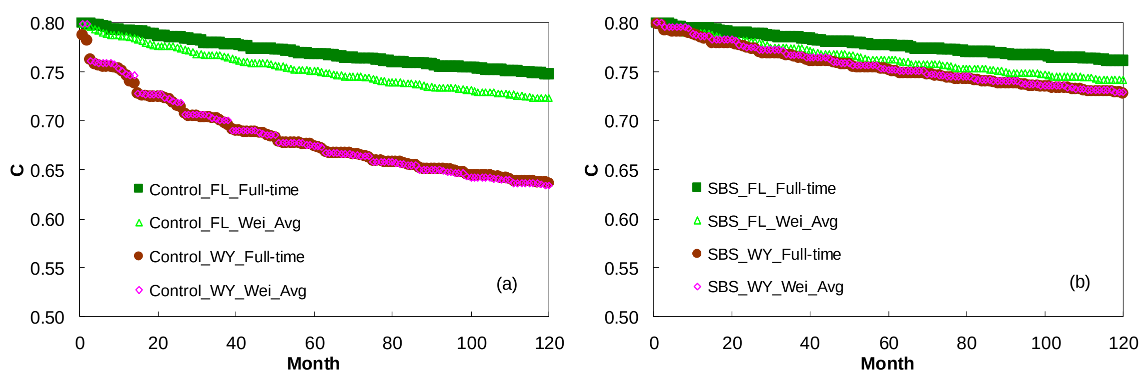

Figure 3-49. Thermal model validation for actual pavement structure for FL and WY temperature profiles using: (a) FHWA Control mix and (b) SBS mix

3.5 : OUTPUT MODULE

The output module consists of the tools and techniques necessary to view and interpret the VECD-FEP++ performance predictions. It creates a single file that can be opened, processed, and manipulated to view visual interpretations (contours) of the predicted damage, stress distribution, or other quantities of interest. This file can also be processed to extract different indices to quantify the visual observations.

3.5.1 : Output in the Form of a Contour Plot

Example contour plots and typical values are shown in Figure 3-50 (a), (b), (c), and (d) for radial stress, radial strain, pseudo stiffness and the condition index, respectively. Through qualitative observations of these contour plots, the damage distribution and evolution in the overall pavement structure can be captured easily. More importantly, because the VECD-FEP++ does not assume the location where the damage is concentrated, and usually the severe damage occurs in small areas (i.e., a few structural elements as compared to several thousands of elements within the whole pavement structure), the damage concentration needs to be tracked for the entire structure. The contour plots in Figure 3-50 show the grids that represent the elements that build the AC layers in the pavement structure. For the sensitivity analysis, the element size of 1.4 cm by 1.4 cm was determined for the AC layers in this research. Moreover, significant damage in an element of this size could be considered to be the initiation of cracking, based on field observations.

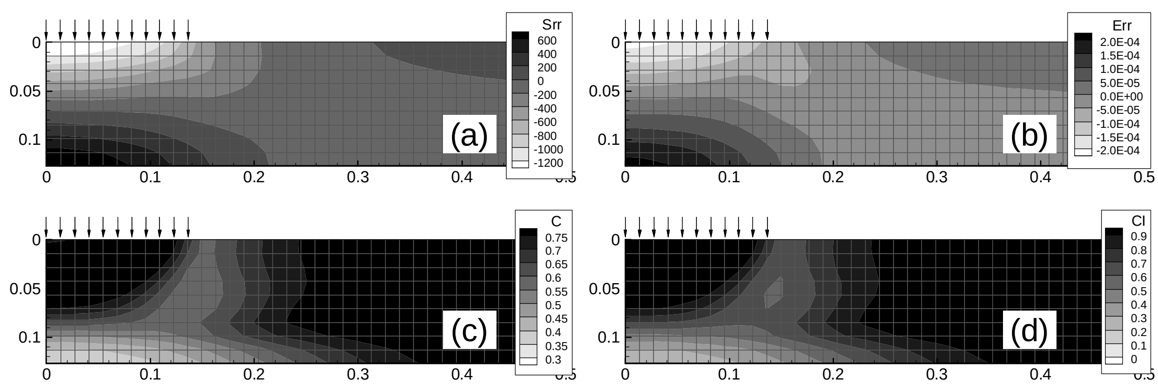

Figure 3-50. Examples of contour plots for: (a) radial stress, (b) radial strain, (c) pseudo stiffness, and (d) the condition index

3.5.2 : Quantification of Cracking Prediction

A scaled parameter, referred to as the condition index (CI) and defined by Equation (3-78), was computed for each element in the pavement structure to interpret the loss in material integrity. As this equation indicates, the CI is a variable that ranges from 0 to 1, with 0 being failure according to the material level criteria discussed in Section 3.2.5.3 (see Figure 3-19), and 1 representing a completely intact body.

$$CI = \frac{C_i - C_{f,i}}{C_{intact} - C_{f,i}}, \tag{3-78}$$

where

CI	=	the condition index,
C_{intact}	=	the intact pseudo stiffness value,
C_i	=	pseudo stiffness at instant i, and
$C_{f,i}$	=	failure pseudo stiffness at instant i.

4. MODEL INTEGRATION

4.1 : INTRODUCTION

Reasonableness and sensitivity studies were carried out by a series of FEP++ simulations to show whether or not the framework development and integration into the VECD-FEP++ were performed correctly. First, a reasonableness check was performed to verify the proper implementation of the VECD model, and hence, the sub-models (healing, aging, thermal damage, etc.) were not included. Second, a sensitivity check was conducted to investigate the effect of each analytical sub-model on pavement performance. From the sensitivity studies it was revealed that the sub-models affect pavement performance in different ways and to varying degrees. Finally, the example simulation was run with two purposes: 1) to assess whether the enhanced VECD-FEP++ which includes all sub-models works properly without any erroneous result and 2) to present how the damage contour in the pavement changes along the months and evolves until the pavement fails.

Two pavement structures, as shown in Figure 4-1, were investigated: thin (127 mm or 5 in.) and thick (304.8 mm or 12 in.). Two AC mixes, the Control and SBS mixes used in the FHWA ALF research, were selected for the simulation because all the necessary model data for both mixes were available, and it has been reported that both mixes show significantly different performance behavior (17). The aggregate gradation, asphalt content, and target air void levels are the same for both mixtures, as shown in Table 4-1.

Table 4-1. Volumetric Properties of Laboratory Mixtures for ALF Pavements

	ALF	
Mix Designation	Control	SBS
Binder Type	Unmodified	Styrene Butadiene Styrene
Binder Grade	PG 70-22	PG 70-28
Binder Content	5.30%	
NMSA*	12.5 mm	
Target Air Voids	4%	
Sieve Size	Gradation, % Passing	
37.5 mm	100.0	
25.0 mm	100.0	
19.0 mm	100.0	
12.5 mm	93.8	
9.5 mm	85.2	
4.75 mm	56.0	
2.36 mm	35.6	
1.18 mm	25.1	
0.600 mm	18.4	
0.300 mm	13.1	
0.150 mm	9.3	
0.075 mm	6.7	

* Nominal Maximum Size Aggregate

Results from the material characterization also show large differences in the material responses, as shown in Figure 4-2. The base layer for the thin pavement structure was 203 mm (8 in.) thick, and the subgrade for both structures was considered to be semi-infinite. The AC layers were modeled using the VECD model and additional analytical models to include such factors as aging, healing, damage factors, and thermal stress. The unbound material layers were assumed to be linear elastic at three different levels of modulus values (weak, moderate, strong), as presented in Table 4-2. The modulus values of both the base layer and subgrade materials were varied to yield either a weak, moderate, or strong support condition. Depending on the purpose of the simulation, the appropriate pavement temperature was selected from the five regional temperature profiles generated from the

EICM. The temperatures varied in accordance with time and depth within a given AC layer. To simulate the variations in temperature with depth, each row of elements in the FEM mesh was assigned a different temperature consistent with the EICM output at the average depth of the row. A moving load was simulated by applying a 0.1 second haversine loading pulse with a magnitude of 40 kN (9 kip) and contact pressure of 689 kPa (100 psi) on the pavement surface, followed by 62.2 seconds or 622 seconds of rest for thin and thick pavement respectively.

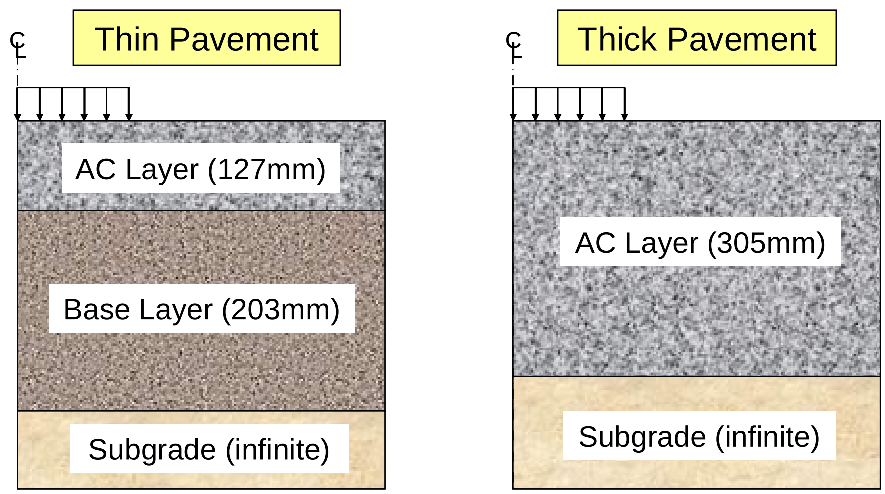

Figure 4-1. Pavement structures for FEP++ simulation

Table 4-2. Elastic Modulus used for Unbound Layers

Layer	Elastic Modulus, MPa (ksi)		
	Weak	Moderate	Strong
Base Layer	138 (20)	276 (40)	552 (80)
Subgrade	41 (6)	83 (12)	166 (24)

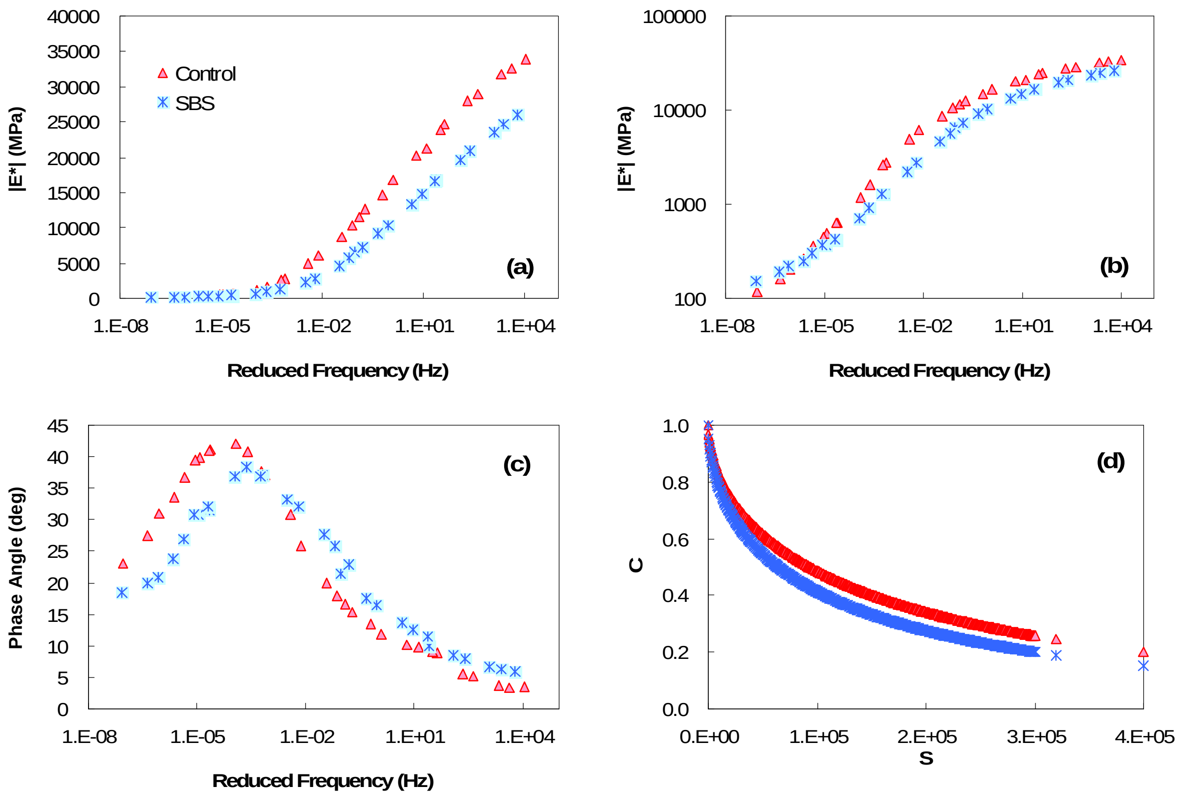

Figure 4-2. Characteristics of Control and SBS mixtures for FEP++ simulation: (a) |*E| mastercurve in semi-log scale; (b) |*E**| mastercurve in log-log scale; (c) phase angle mastercurve; and (d) damage characteristic curve**

4.2 : REASONABLENESS

To verify the modeling framework, first a reasonableness check is performed. Because the purpose here is to verify that the VECD model is implemented correctly, the analytical sub-models (healing, aging, thermal damage, etc.) are not included. Table 4-3 summarizes the simulation details for the analysis to verify reasonableness. Three factors were chosen based on the general effects that are expected of such factors from experience. Four temperature profiles were selected to represent the critical conditions: Tallahassee, Florida in the summer (FL-Jun) at 5:00 AM (5:00) and at 2:00 PM (14:00), and Laramie, Wyoming in the winter (WY-Dec) at 5:00 AM and at 2:00 PM. The temperature profiles for these four conditions are shown in Figure 4-3. For both geographical locations, the 5:00 AM temperature profile shows a low temperature at the top of the pavement and a high temperature at the bottom. Due to heat from the sun, the opposite trend occurs for both locations at 2:00 PM. Differences between the average temperatures for the two locations are also evident from Figure 4-3. The two pavement structures shown in Figure 4-1 and the two asphalt mixtures from the ALF study (Control and SBS) were utilized in these simulations.

Table 4-3. Simulation Details for Reasonableness Check

Item	Number of Cases	Detail
Region	4	FL-Jun-5:00, FL-Jun-14:00, WY-Dec-5:00, WY-Dec-14:00
Structure	2	Thin (127 mm or 5 in.), Thick (304.8 mm or 12 in.)
AC Material	2	ALF Control, ALF SBS
Support Condition	1	Moderate
Aging	1	No Aging
Healing	1	None
Thermal Stress	1	None
DF	1	None
Total Number of Cases	16	

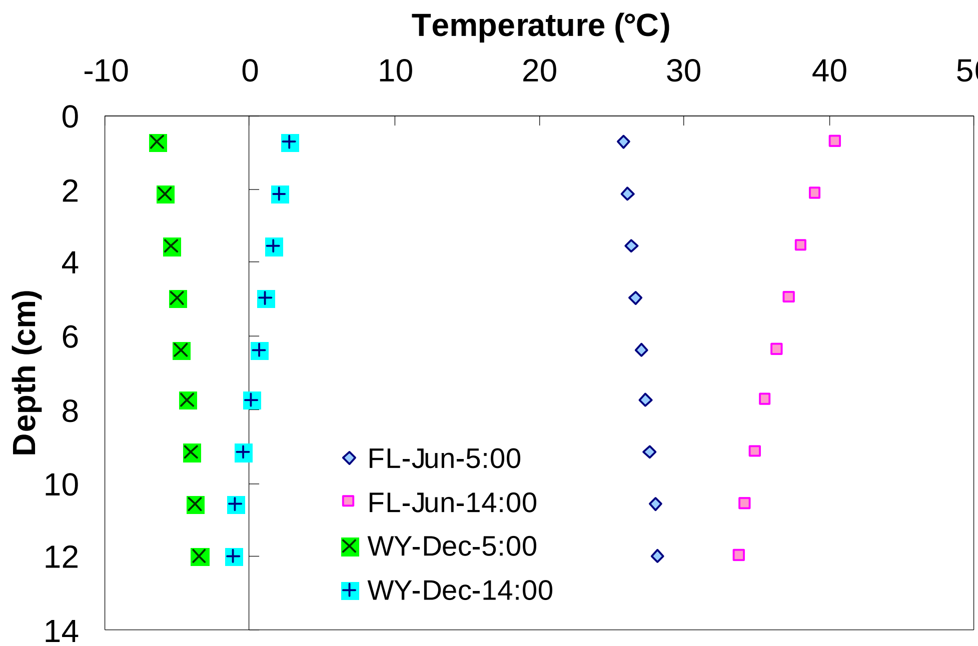

Figure 4-3. Temperature profile for reasonableness check

Simulation results are presented in Table 4-4 to Table 4-6 in terms of the radial stress and strain at the peak loading time (0.05 second) for all 16 test cases. For easier comparisons, all contours for the same variables (stress or strain) are plotted using the same scale. From the contours shown in Table 4-4 to Table 4-6, the following comparisons can be made:

- Highest versus lowest temperature profile by region (Florida and Wyoming)
- Florida versus Wyoming by time of day (5:00 AM or 2:00 PM)
- Control versus SBS mixtures under the same condition(s)
- Thin versus thick structure under the same condition(s)

A key observation from the plots shown in Table 4-4 to Table 4-6 is that the tensile strain at the pavement bottom is greater at higher temperatures. The magnitude of stress also shows a change, a decrease, with increasing temperatures. This effect is expected because the support conditions are constant for all cases, and the modulus value of the asphalt layer increases with reductions in temperature. However, it is interesting that daily temperature variations have little effect on the stress distribution. Instead, a large difference in the mean temperature is needed in order to change the stress distribution noticeably. This effect is more obvious in the thin pavements than in the thick pavements, and results from increased bending-related stress in the thin pavements. Of course, because the stress distribution changes very little due to temperature variations, the strain magnitude increases with the temperature because the material is softer at higher temperatures. Unlike the stress distributions, though, these changes in strain magnitude may be noticeably different during daily temperature fluctuations.

Comparisons of material type reveal that when the SBS materials are used, higher strain magnitudes result. If the temperatures shown in Figure 4-3 are combined with the data shown in Figure 4-2, i.e., the mastercurve, appropriate time temperature shift factors, and a quasi-approximate time-frequency conversion (37), it can be seen that the most extreme temperature in the simulations, 41°C, and the loading time of 0.1 second, correspond approximately to a reduced frequency of 6.0×10^{-5} Hz. At this reduced frequency, the SBS material shows a softer LVE response than the Control mixture, as seen in Figure 4-2. If, on the other hand, the simulation is performed at the high temperature PG grade (continuous grade-based) of the two mixtures, 72°C, then the approximate equivalent reduced frequency would be 1.5×10^{-7} Hz. At this reduced frequency, the SBS mixture is stiffer (in terms of linear viscoelasticity) than the Control mixture, and it should be expected that the radial strain would be less for the SBS mixture than for the Control mixture. Table 4-7 shows the contours for a thin pavement at 0.05 second and at 72°C for both the SBS and the Control mixtures. From this table it is seen that the SBS mixture shows less total strain than the Control mixture, which, along with the data in Table 4-4 to Table 4-6 and Figure 4-2, confirms the reasonableness of the response predictions with regard to material type.

Finally, comparisons between the thin and thick pavements show that the magnitude of the tensile strain at the bottom of the thin pavement is always greater than the strain in the equivalent thick pavement case. The difference is more noticeable in the Wyoming simulations because of the scaling used in the contours and because the Wyoming conditions result in a mixture with a high modulus. The Florida simulations show similar gray scale patterns of the thick and thin pavements, which is a result of setting a scale capable of delineating strain under all of the conditions shown. These cases are thus misleading; in reality, the strain in the thin pavement case is greater than in the simulations. It is also observed that the approximate pavement shear center, as indicated by a bulb of radial strain extending near the loading edge, is relatively higher in the thick pavement (at 20% of total depth) than it is in the thin pavement case (at 40% of total depth). This behavior is to be expected in layered analysis.

Table 4-4. Radial Stress and Strain Contours for Reasonableness Check: Thin Pavements – Florida and Wyoming

Case	Radial Stress at t = 0.05 sec (kPa)	Radial Strain at t = 0.05 sec
FL-Jun-5:00 Thin-Control	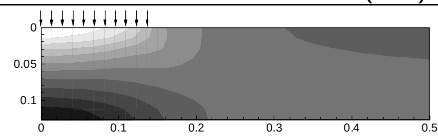	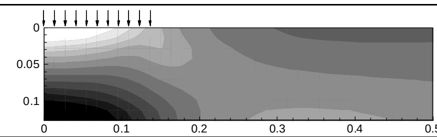
FL-Jun-5:00 Thin-SBS	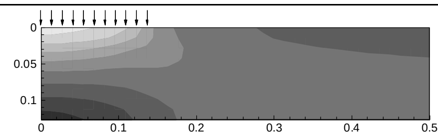	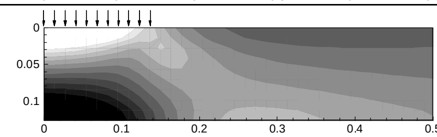
FL-Jun-14:00 Thin-Control	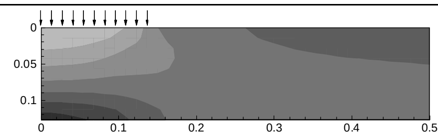	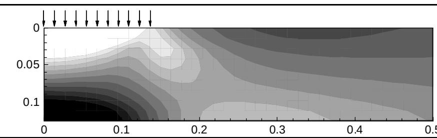
FL-Jun-14:00 Thin-SBS	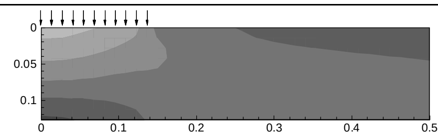	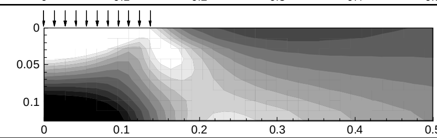
WY-Dec-5:00 Thin-Control	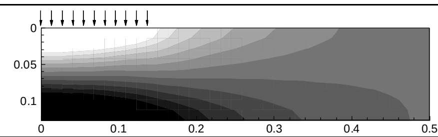	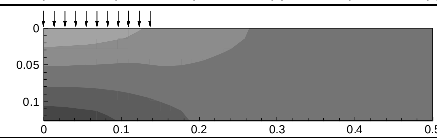
WY-Dec-5:00 Thin-SBS	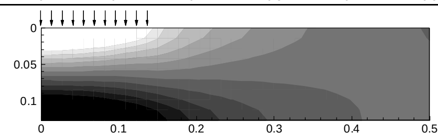	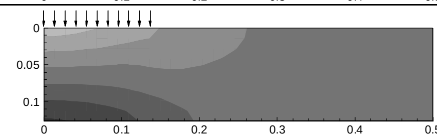
WY-Dec-14:00 Thin-Control	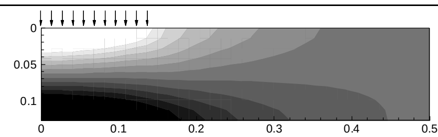	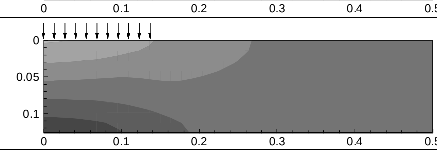
WY-Dec-14:00 Thin-SBS	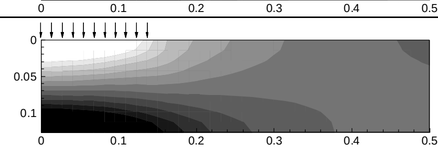	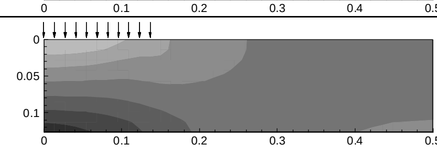
Contour Legend	Srr: -1200 -1000 -800 -600 -400 -200 0 200 400 600 800 Err: -1.6E-04 -1.3E-04 -1.0E-04 -7.0E-05 -4.0E-05 -1.0E-05 2.0E-05 5.0E-05 8.0E-05 1.1E-04 1.4E-04	

Table 4-5. Radial Stress and Strain Contours for Reasonableness Check: Thick Pavements - Florida

Case	Radial Stress at t = 0.05 sec (kPa)	Radial Strain at t = 0.05 sec
FL-Jun-5:00 Thick-Control	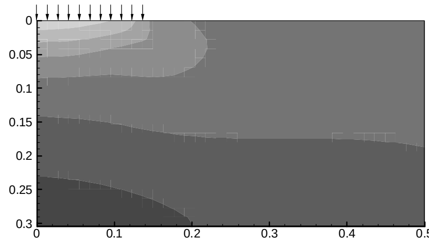	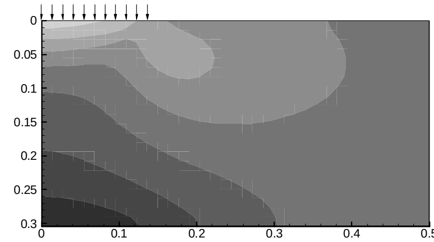
FL-Jun-5:00 Thick-SBS	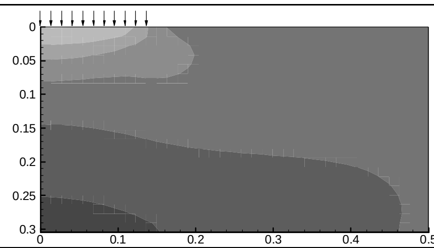	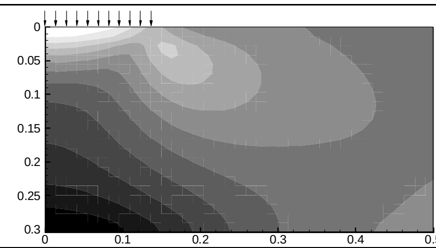
FL-Jun-14:00 Thick-Control	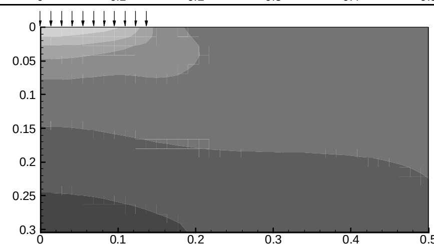	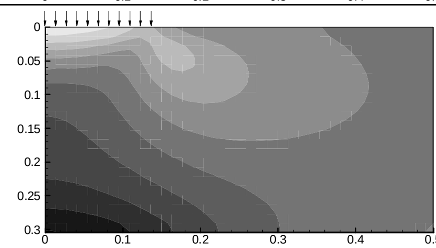
FL-Jun-14:00 Thick-SBS	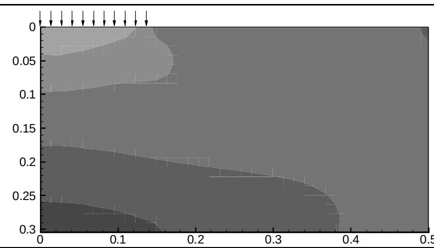	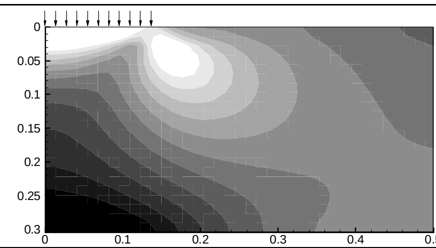
Contour Legend	Srr: -1200 -1000 -800 -600 -400 -200 0 200 400 600 800 Err: -1.6E-04 -1.3E-04 -1.0E-04 -7.0E-05 -4.0E-05 -1.0E-05 2.0E-05 5.0E-05 8.0E-05 1.1E-04 1.4E-04	

Table 4-6. Radial Stress and Strain Contours for Reasonableness Check: Thick Pavements - Wyoming

Case	Radial Stress at t = 0.05 sec (kPa)	Radial Strain at t = 0.05 sec
WY-Dec-5:00 Thick-Control	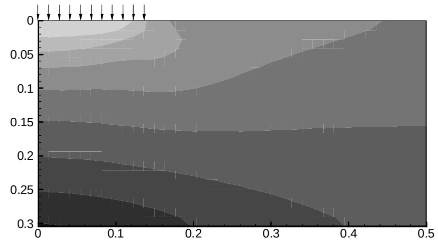	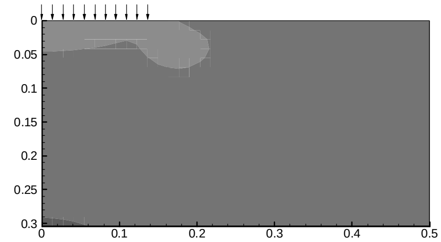
WY-Dec-5:00 Thick-SBS	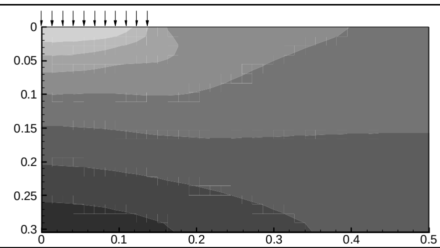	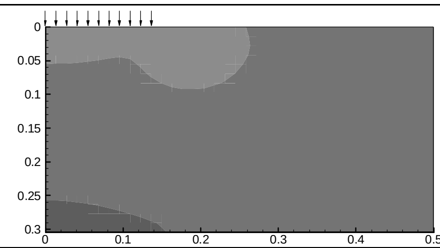
WY-Dec-14:00 Thick-Control	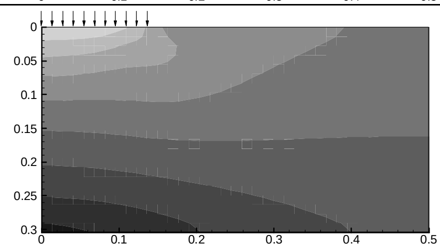	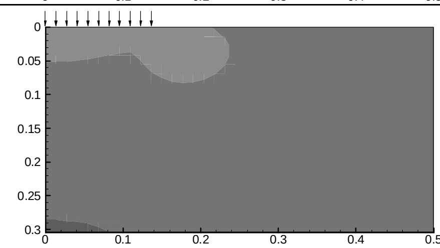
WY-Dec-14:00 Thick-SBS	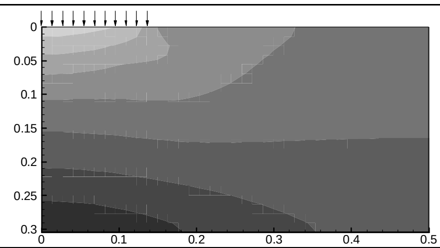	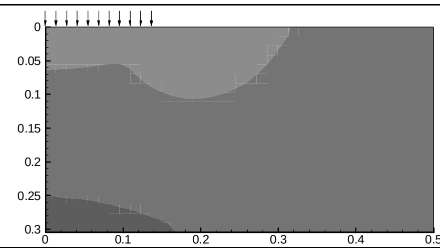
Contour Legend	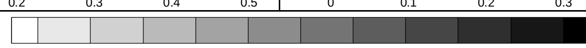 Srr: -1200 -1000 -800 -600 -400 -200 0 200 400 600 800  Err: -1.6E-04 -1.3E-04 -1.0E-04 -7.0E-05 -4.0E-05 -1.0E-05 2.0E-05 5.0E-05 8.0E-05 1.1E-04 1.4E-04	

Table 4-7. Radial Stress and Strain Contours for Reasonableness Check: Thin Pavements – Full Depth 72°C

Case	Radial Stress at t = 0.05 sec (kPa)	Radial Strain at t = 0.05 sec
HighTemp. 72ºC Thin-Control	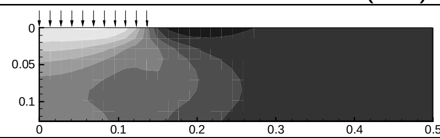	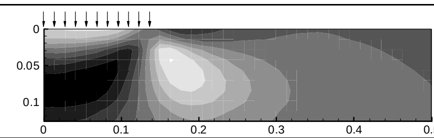
HighTemp. 72ºC Thin-SBS	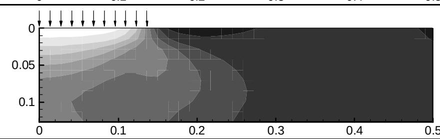	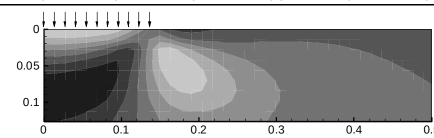
Contour Legend	 Srr: -400 -350 -300 -250 -200 -150 -100 -50 0 50  Err: -1.0E-03 -8.0E-04 -6.0E-04 -4.0E-04 -2.0E-04 0.0E+00 2.0E-04 4.0E-04 6.0E-04	

4.3 : SENSITIVITY

This section discusses in detail the effect of each analytical sub-model on pavement performance. Simulation details are shown in Table 4-8. Here, the pavement structure and asphalt material are fixed as the thick pavement and Control mix, respectively. Temperature data for two regions (Florida and Wyoming) are utilized for 1 year or 20 years, depending on the purpose. It was decided that the DF should be included in all cases, because this factor has a significant effect, especially in Florida, which experiences relatively higher temperatures than Wyoming. For the support condition, sensitivity is evaluated independently of the other factors, but a specific condition was chosen for the sensitivity analysis of each variable (i.e., a weak support condition was used to assess the DF, and a moderate support condition was used to assess aging). The rationale behind selecting which support condition to use for which variable is to amplify the effect of the variable under investigation; i.e., the support condition is chosen to represent the worst case scenario. Note that the sensitivity of the healing model was not investigated in this research because the effect of the healing model cannot be properly captured in a simple simulation and thus, simulations performed for this research will utilize only one type of healing model coefficients regardless AC materials due to limited resource.

Table 4-8. Simulation Details for Sensitivity Check

Item	Number of Cases	Details
Region	2	FL, WY
Structure	1	Thick (304.8 mm or 12 in.)
AC Material	1	ALF Control
Support Condition	3	Weak, Moderate, Strong
Aging	2	No Aging, Aging
Healing	0	None
Thermal Stress	2	High vs. Low Thermal Coefficient
DF	2	1-yr EICM or 10-yr EICM
Total Number of Cases	32	

4.3.1 : Support Condition Effect

Table 4-9 displays a comparison of the damage contours for Florida and Wyoming to show the effects of varying the support condition. From this table it is evident that a strong support condition leads to an overall reduction in damage distribution. The effect is most significant for the top-down damage, but also affects the damage at the bottom of the pavement. It is also seen that the effect of the support condition is most noticeable in the case of the Florida climatic condition.

Table 4-9. Support Condition Effect in Florida and Wyoming

Conditions	FL	WY
Control Mix **SC – Weak** DF No Aging No Healing No Thermal	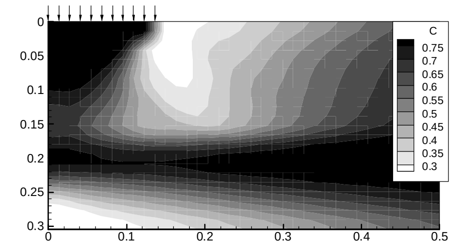	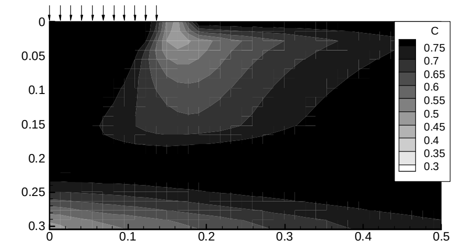
Control Mix **SC – Moderate** DF No Aging No Healing No Thermal	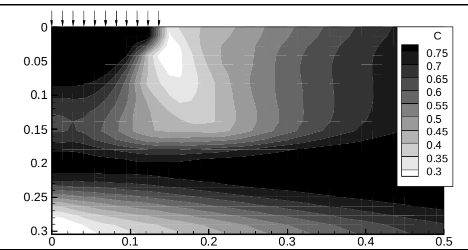	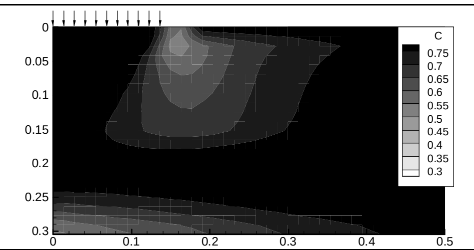
Control Mix **SC – Strong** DF No Aging No Healing No Thermal	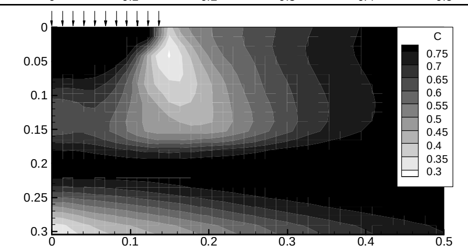	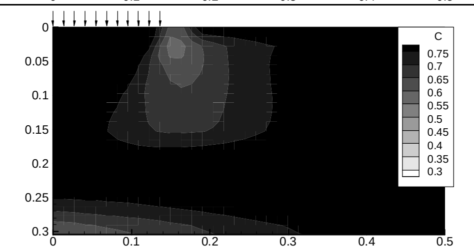

4.3.2 : Aging Effect

To investigate the effect of aging, FEP++ simulations were conducted, and the results are shown in Table 4-10 and Table 4-11. In the simulations a single year run was performed, but the input material properties correspond to either the un-aged properties (denoted as No Aging) or the 20 year-aged properties (denoted as Aging). Because the amount of field aging is related directly to environmental conditions, two extreme cases, Laramie, Wyoming and Tallahassee, Florida, were used in this sensitivity analysis. The ALF Control mixture was used for both cases. Note that, because the purpose of the first simulation runs was to assess only the sensitivity of the aging model, the healing and thermal damage models were not active. The following observations can be made from the contours shown in Table 4-10 and Table 4-11:

- Aging can have a noticeable effect on the damage growth in a pavement, particularly at the pavement surface;
- The effects of aging are more significant in climates with higher annual pavement temperatures (Florida) than in cooler climates (Wyoming);
- Although the effects of aging are most noticeable at the pavement surface, aging affects the way stress distributes throughout the pavement and, thus, the way that damage accumulates throughout the whole pavement structure.
- Aging also increases the C at failure and thus, this increased C_f maximizes the aging effect as can be seen in Table 4-11.

Table 4-10. Aging Effect in Florida and Wyoming - *C* Contours

Conditions	FL	WY
Control Mix SC – Moderate DF **No Aging** No Healing No Thermal	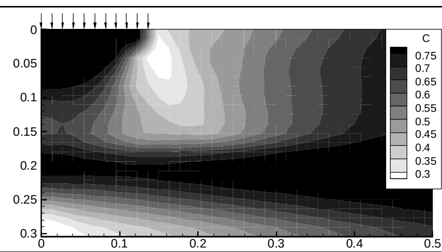	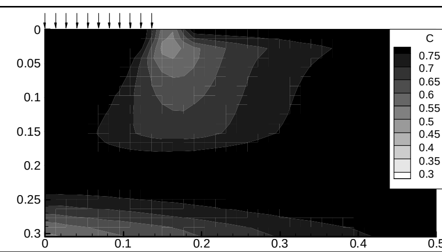
Control Mix SC – Moderate DF **Aging** No Healing No Thermal	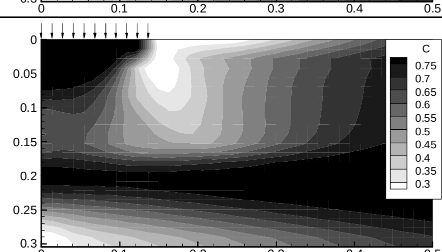	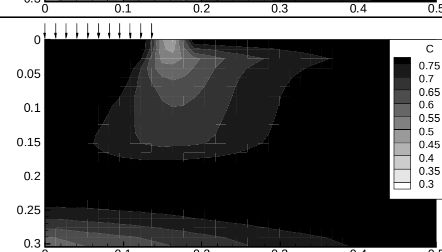

Table 4-11. Aging Effect in Florida and Wyoming - *CI* Contours

Conditions	FL	WY
Control Mix SC – Moderate DF **No Aging** No Healing No Thermal	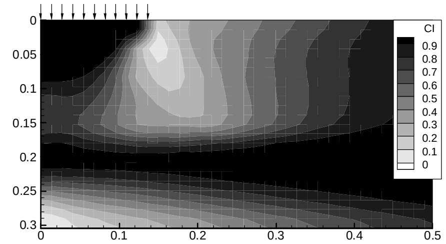	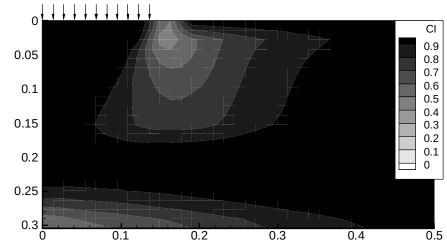
Control Mix SC – Moderate DF **Aging** No Healing No Thermal	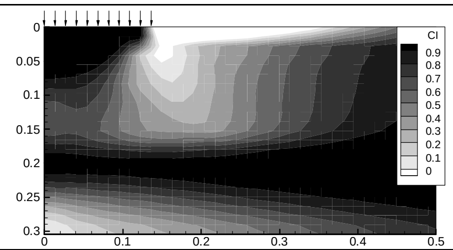	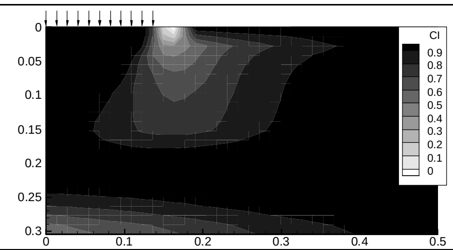

4.3.3 : Thermal Stress Effect

Thermal stress is the direct result of structural constraints on material expansion. When a material is heated or cooled it tends to expand or contract by an amount directly proportional to the change in temperature. The constant of proportionality is known as the *thermal coefficient*, and for the purposes here is assumed to be a material constant. This parameter is not typically measured for AC, but it can be estimated from Equation (4-1) (19). A parametric study using this equation with typical in-service input values shows that this property may range from 1.3 x 10^{-5} to 2.5 x 10^{-5} $e/°C$. For the sensitivity analysis two a_{mix} values of the minimum and maximum from the range, 1.3 x 10^{-5} and 2.5 x 10^{-5} $e/°C$, were used.

$$a_{mix} = \frac{VMA * a_{AC} + V_{AGG} * a_{agg}}{3 * V_{Total}}, \qquad (4\text{-}1)$$

where

a_{mix}	=	thermal coefficient of the mixture,
a_{AC}	=	thermal coefficient of the asphalt cement (3.45 x 10^{-4} $e/{}^{o}C$),
a_{agg}	=	thermal coefficient of the aggregate particles (6.5 x 10^{-6} $e/{}^{o}C$),
VMA	=	percentage of voids in the mineral aggregate,
V_{AGG}	=	percentage of aggregate in the mixture, by volume, and
V_{Total}	=	percentage of total volume, 100.

Laramie, Wyoming and Tallahassee, Florida are the regions selected for these simulations and one year simulation was performed starting from October. The results are shown in Figure 4-4 for the four different conditions. From this figure it is clearly observed that the damage is greater with the larger thermal coefficient. The effect of the thermal coefficient varies by region because the modulus is affected by the mean temperature. In the case of the Florida simulation, the material is much more viscous than it is in the Wyoming case. As a result, the material is more likely to relax and absorb thermally-induced dimensional changes and, therefore, experience less damage. Because the overall effect of thermal damage is reduced, the apparent effect of the thermal coefficient is also reduced for Florida.

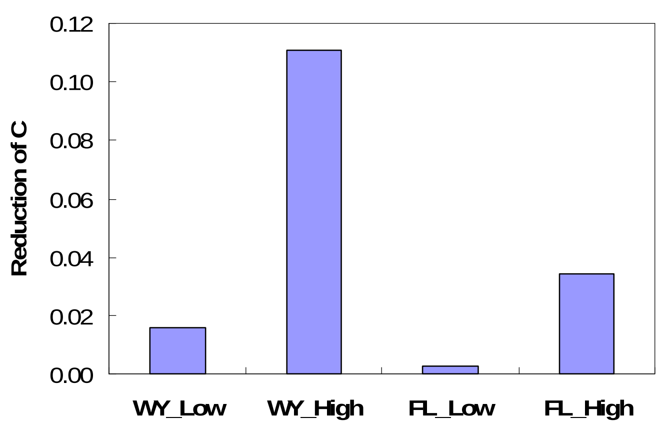

Figure 4-4. Sensitivity of thermal damage growth to selected thermal coefficients

4.3.4 : Viscoplastic Effect

The effect of viscoplasticity on pavement performance, especially cracking, could be significant, depending on the material, structure, and/or temperature. As described in Section 3.3.2, the effect of viscoplasticity on the pavement performance can be handled through the Damage Factor (DF).

To evaluate the viscoplastic effect, simulations were conducted by making only the DF analytical model active. The other sub-models – healing, aging and thermal – were inactive. Some typical results are shown in Table 4-12. To amplify the effects of the DF, the support conditions for the contours are all weak, as shown in Table 4-12. These simulations were run for one year with and without the DF. As is clearly seen in Table 4-12, the DF noticeably reduces the total damage growth for both the Wyoming and Florida regions. The effects of the DF are somewhat more pronounced in the Florida case and much more pronounced near the pavement base.

Table 4-12. Viscoplastic Effect in Two Extreme Regions: Florida and Wyoming

Conditions	FL – 1 year	WY – 1 year
Control Mix SC – Weak **No DF** No Aging No Healing No Thermal	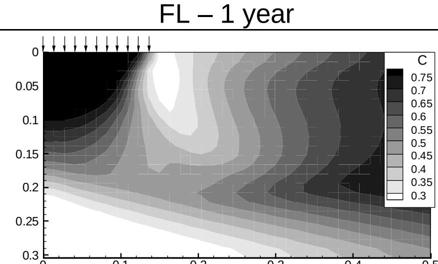	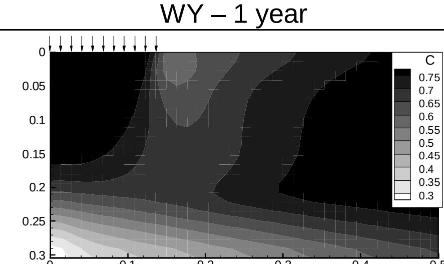
Control Mix SC – Weak **DF** No Aging No Healing No Thermal	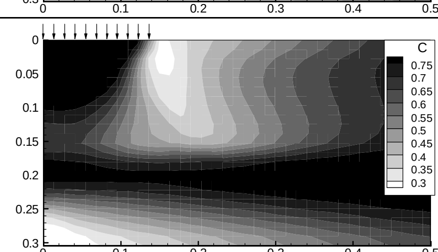	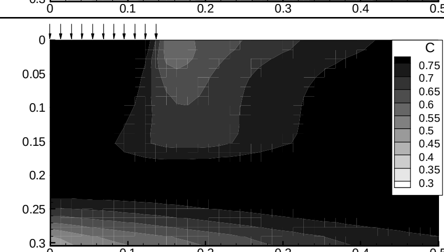

Another important aspect of the DF that should be examined is the temperature used in the computations. This issue is important because most of the temperature data compiled in the EICM are less than 10-year data, and to simulate a pavement condition requires repeating the data. The effect of sequential year temperature data on the DF calculation was evaluated. Two methods to calculate the DF were chosen:

- Calculate the DF using 1-year EICM data and repeat both the temperature profiles and the DF 20 times.
- Calculate the DF year by year and use annual specific temperature profiles by repeating the 10-year EICM data.

As with the other DF sensitivity analysis, no other analytical sub-models were active in these simulations. For simulation purposes, the D.C. temperature data were selected as representative for all regions. The ALF Control mix and a moderate modulus were utilized for the asphalt layer and subgrade, respectively. As shown in Table 4-13, the two methods generate similar results. As a result of the analysis shown in Table 4-13, it is concluded that the DF calculation is not sensitive to yearly temperature fluctuations and, as a result, only a single annual temperature profile needs to be used in computing its value. Because thermal effects were considered by sequentially repeating five years of EICM data, the DF was computed based on the average of five years of EICM data.

Table 4-13. Sensitivity of the Damage Factor Calculation

<table>
<tr><th>Conditions</th><th>Method</th><th>DC -20 years</th></tr>
<tr><td rowspan="2">Control Mix
SC – Moderate
DF
No Aging
No Healing
No Thermal</td><td>EICM-1 yr
DF-1 yr</td><td>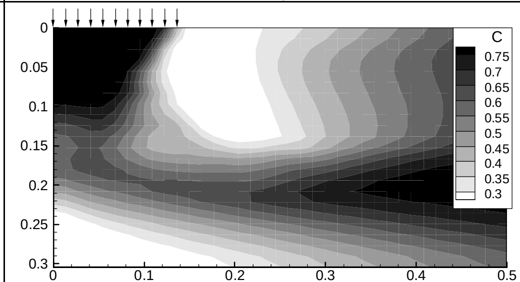</td></tr>
<tr><td>EICM-10 yr
DF-20 yr</td><td>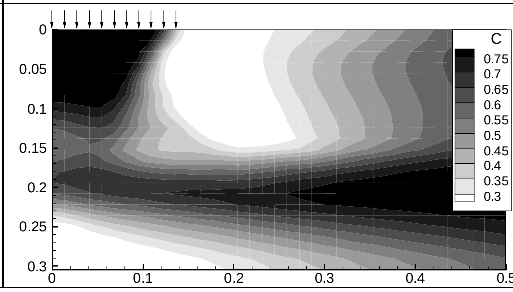</td></tr>
</table>

4.4 : EXAMPLE SIMULATION

4.4.1 : Simulation Details

An example simulation of the FEP++ using the VECD model and all accompanying analytical sub-models was carried out to demonstrate the capabilities of the modeling approach. For this example problem, a single region – wet, freeze-thaw cycling for Washington, D.C. – was chosen. Only a single support condition, *moderate*, was used for this example, and all other factors were fixed except the pavement thickness, which was evaluated at the 101.6 mm (4 in.) and 304.8 mm (12 in.) levels. All of the sub-models were active for these simulations. The simulation details are summarized in Table 4-14.

Table 4-14. Simulation Details for Example Simulation

Item	Number of Cases	Details
Region	1	DC
Structure	2	Thin (101.6 mm or 4 in.), Thick (304.8 mm or 12 in.)
AC Material	1	ALF Control
Support Condition	1	Moderate
Aging	1	Yes
Healing	1	Yes
Thermal Stress	1	High Thermal Coefficient
Damage Factor	1	5-yr Average EICM
Climate	1	5-yr EICM Repeated
Load Level	1	40 kN (9 kip)
Contact Pressure	1	689 kPa (100 psi)
Total Number of Cases	2	

4.4.2 : Simulation Results and Discussion

Results from the simulations are shown as a series of contour plots. The variable of interest in these contours is the condition index (CI). The resulting contour plots for this simulation condition are summarized in Table 4-15. In this table, the month column contains two items of information: the cumulative number of months (all simulations began in October) and the corresponding month. Simulations were performed until any element reached a condition index (CI) value of 0. As a result, the thin pavement was failed after 14 months while the thick pavement was failed after 75 months. Table 4-15 shows the contours for the months of January through November of the first simulation year for both the thin pavement and the thick pavement. In addition, the contours for the months of the final year for the thick pavement simulation are shown in the far right column of the table. All contours could be interpreted in terms of the extent and severity of the damage.

Table 4-15. Condition Index (CI) Contours for Example Simulations

Mon.	t-C-M-DC	T-C-M-DC (1st Year)	Mon.	T-C-M-DC (6th Year)
4 (Jan)	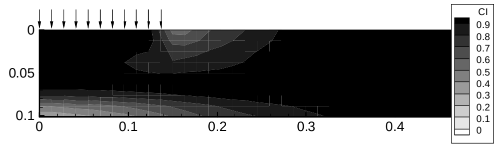	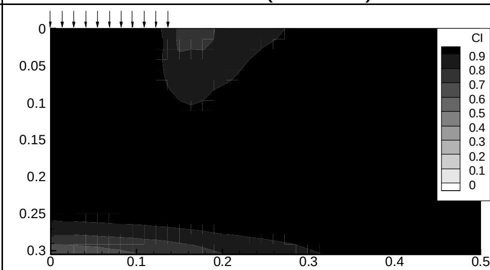	64 (Jan)	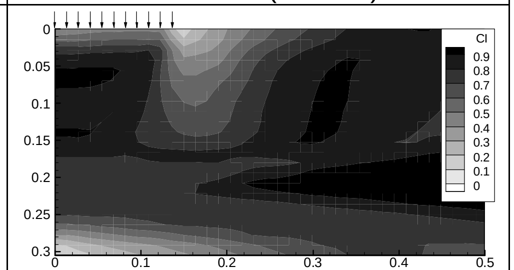
6 (Mar)	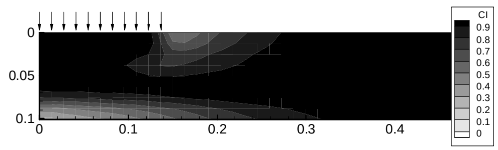	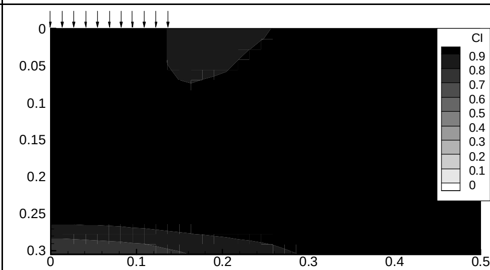	66 (Mar)	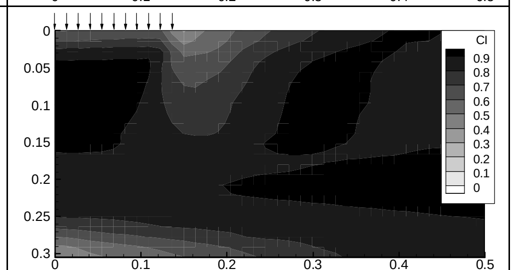
8 (May)	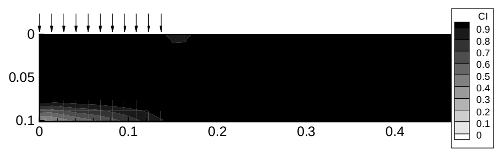	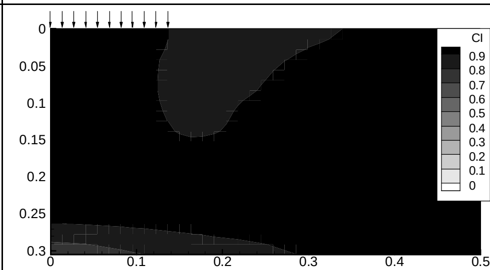	68 (May)	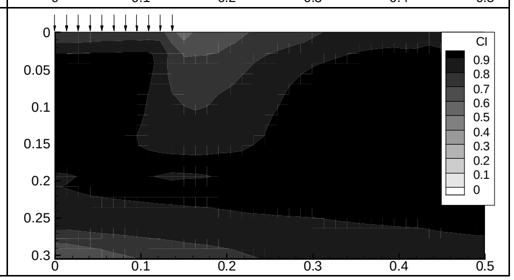

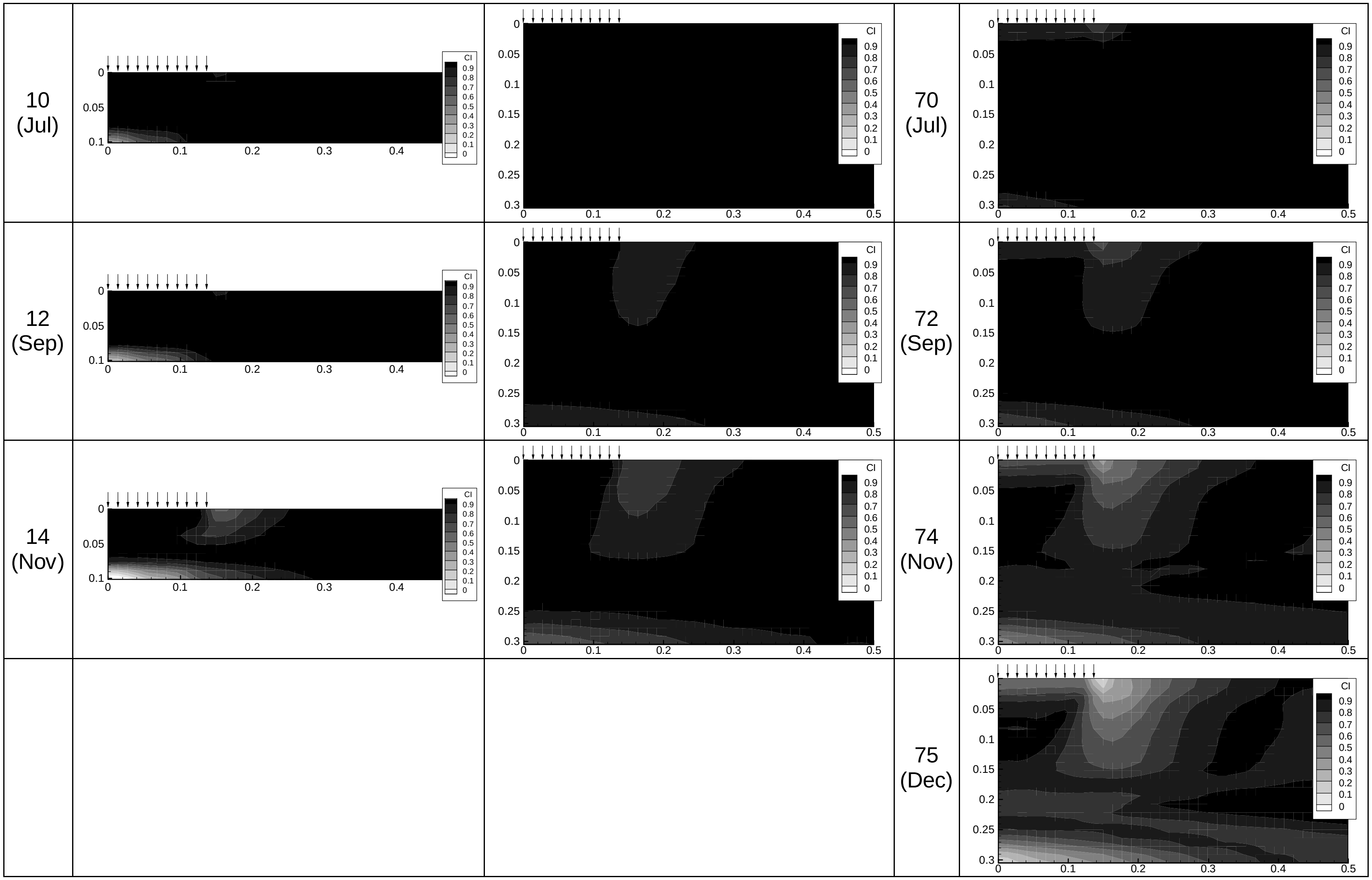
10
(Jul)
70
(Jul)
12
(Sep)
72
(Sep)
14
(Nov)
74
(Nov)
75
(Dec)
Cl

A few observations can be made from Table 4-15. The thin pavement was failed at the bottom and center of the AC layer while the thick pavement was failed at the top and wheel load edge of the AC layer. Such results follow the generally accepted knowledge, e.g., thin pavement tends to show the bottom-up cracking whereas thick pavement tends to show the top-down cracking. It was also observed from examining the damage evolution between the months of May and July that pavement healing may constitute a major component of a pavement’s total fatigue performance. However, it is seen, through the mechanisms associated with repeated loading, healing and aging, that the thick pavement shows an area of concentrated damage at the pavement surface near the wheel load edge. Therefore, it appears that healing is more effective near the pavement surface of a thin pavement than that of a thick pavement; i.e., the thick pavement appears to heal better at the bottom of the pavement than does the thin pavement.

Another observation was that the thick pavement shows relatively significant thermal damage at the surface of AC layer, especially right under the wheel load, while the thin pavement does not show any noticeable damage due to the thermal loading. Thermal stress generated by temperature variation is not sensitive to the structure and the same magnitude of mechanical loading results in relatively higher stresses in the thin pavement than in the thick pavement. Thus, the effect of thermal stress generated by the same temperature profile is much less in the thin pavement than in the thick pavement.

5. MODEL EVALUATION

5.1 : PARAMETRIC STUDY

5.1.1 : Introduction

A systematic evaluation using the VECD-FEP++ code was carried out to gain insight into the parameters most responsible for the development and/or dominance of TDC. Combinations of three regions (FL, DC, and WY), two structures (thin and thick pavements), two materials (Control ALF and SBS ALF) and three support conditions (weak, moderate, and strong) were investigated in order to study the simple and interactive variables. The factorial levels are summarized in Table 5-1.

Table 5-1. Simulation Details for the Parametric Study

Item	Number of Cases	Details
Region	3	FL, DC, WY
Structure	2	Thin (101.6 mm or 4 in.), Thick (304.8 mm or 12 in.)
AC Material	2	ALF Control, ALF SBS
Support Condition	3	Weak, Moderate, Strong
Aging	1	Yes
Healing	1	Yes
Thermal Stress	1	High Thermal Coefficient
Damage Factor	1	5-yr Average EICM
Climate	1	5-yr EICM Repeated
Load Level	1	40 kN (9 kip)
Contact Pressure	1	689 kPa (100 psi)
Total Number of Cases	36	Combination of all Cases

The most important factors identified, for which all the necessary inputs are available, are: material type (modified versus unmodified), pavement thickness (thin versus thick), climate (wet, freeze-thaw cycling versus wet, no freeze versus dry, hard freeze, spring thaw), and support condition (weak versus moderate versus strong). Both asphalt content and air void content are known to be important factors that affect the cracking performance of HMA pavements; however, sufficient experimental data were not available for which the only independent variables were asphalt content and air void content.

5.1.2 : Simulation Results and Discussion

Table 5-2 summarizes the simulation results for the parametric study, including the cumulative number of months to failure for each case. Simulations for all cases were run until any element reached a condition index (CI) value of 0 or until 20 years had been simulated. Some cases, especially those with the Florida climate, did not fail after 20 years. The simulated CI contours are shown for the thin pavements in Table 5-3 and for the thick pavements in Table 5-4 and Table 5-5. Note that the contours show the pavement condition at failure, except for six cases that did not fail in 20 years. For those six cases, the contours were determined for January of the 20th year because those contours represent the maximum damage. The cumulative number of months to failure and the corresponding month are shown below each contour. One finding that is derived from the month at failure is that most cases fail during the cold season, i.e., from October to February, except for four cases that failed during the warm season, i.e., from April to July, and those four cases are under the Florida climate condition. Failure during the cold season in most cases was caused by a combination of low healing potential, thermal damage, and a high failure criterion. Also, it can be seen from the contours of the four cases that failed during warm months that the damage is highly concentrated at the top and load edge.

Table 5-2. Simulation Results for the Parametric Study

Structure	AC	Sublayer	Climate	ID	Cumulative number of months to failure	
					Top	Bottom
Thin (4 in.)	Control	Weak	FL	t-C-W-FL		16
			DC	t-C-W-DC		5
			WY	t-C-W-WY		3
		Moderate	FL	t-C-M-FL		51
			DC	t-C-M-DC		14
			WY	t-C-M-WY		13
		Strong	FL	t-C-S-FL	-[a]	-
			DC	t-C-S-DC		27
			WY	t-C-S-WY		26
	SBS	Weak	FL	t-S-W-FL	34	
			DC	t-S-W-DC	3	3
			WY	t-S-W-WY	2	2
		Moderate	FL	t-S-M-FL	115	
			DC	t-S-M-DC		3
			WY	t-S-M-WY		3
		Strong	FL	t-S-S-FL	-	-
			DC	t-S-S-DC		41
			WY	t-S-S-WY		40
Thick (12 in.)	Control	Weak	FL	T-C-W-FL	100	
			DC	T-C-W-DC		27
			WY	T-C-W-WY	26	26
		Moderate	FL	T-C-M-FL	116	
			DC	T-C-M-DC	75	
			WY	T-C-M-WY	28	
		Strong	FL	T-C-S-FL	220	
			DC	T-C-S-DC	122	
			WY	T-C-S-WY	28	
	SBS	Weak	FL	T-S-W-FL	115	
			DC	T-S-W-DC	39	
			WY	T-S-W-WY	26	
		Moderate	FL	T-S-M-FL	-	-
			DC	T-S-M-DC	123	
			WY	T-S-M-WY	38	38
		Strong	FL	T-S-S-FL	-	-
			DC	T-S-S-DC	-	-
			WY	T-S-S-WY		38

[a] Pavement did not fail in 20 years.

In Figure 5-1 to Figure 5-4, the cumulative number of months to failure is plotted for each parameter, i.e., the structure, AC mix, sublayer, and climate, in order to investigate the effect of each parameter, and each point is taken from the same condition except the main parameter that is under consideration. In addition, in some of these figures, the points are distinguishable by a different mark that is indicated in legend. Note that the left side figures are in arithmetic scale and the right side figure are in logarithmic scale for the same data.

The naming convention used for the different simulations is by letter and in the following order: pavement type, thick (T) or thin (t); material type, ALF Control (C) or ALF SBS (S); and support condition, weak (W) or moderate (M) or strong (S). For example, t-C-W indicates a thin pavement with an ALF Control material layer over a weak supporting layer.

Table 5-3. Parametric Study Simulations for Thin (t) Pavements

Condition	FL	DC	WY
t-C-W	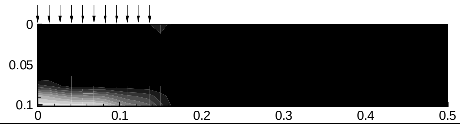 16[a] (Jan)	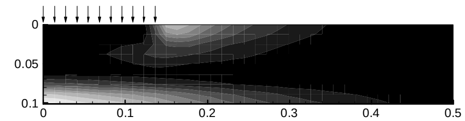 5 (Feb)	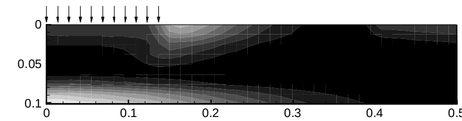 3 (Dec)
t-C-M	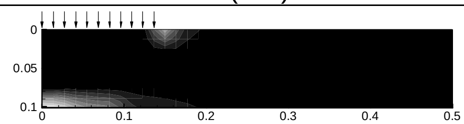 51 (Dec)	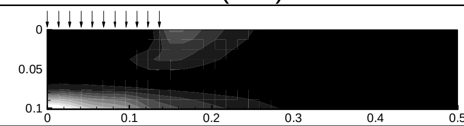 14 (Nov)	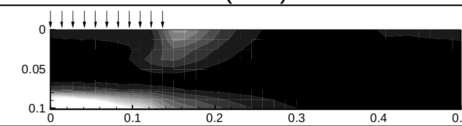 13 (Oct)
t-C-S	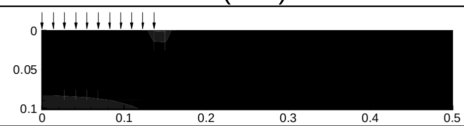 232 (Jan) – Not Failed	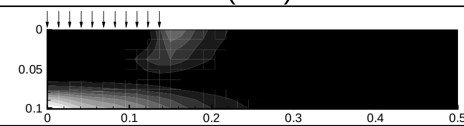 27 (Dec)	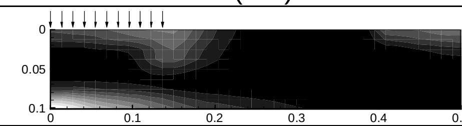 26 (Nov)
t-S-W	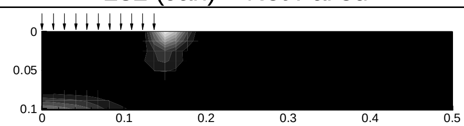 34 (Jul)	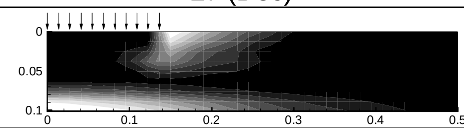 3 (Dec)	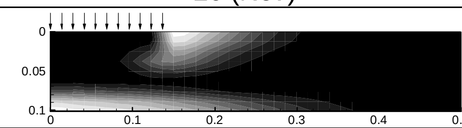 2 (Nov)
t-S-M	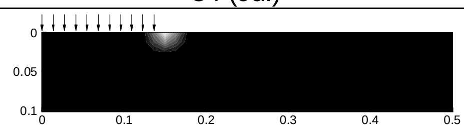 115 (Apr)	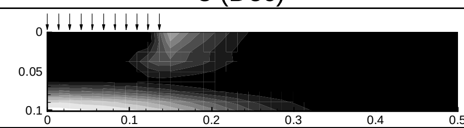 3 (Dec)	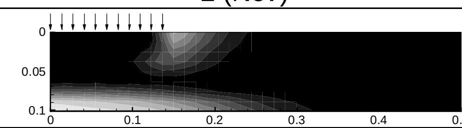 3 (Dec)
t-S-S	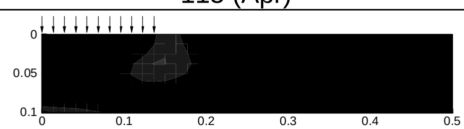 232 (Jan) – Not Failed	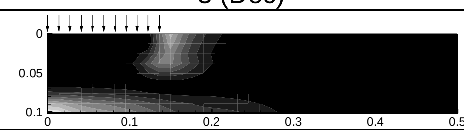 41 (Feb)	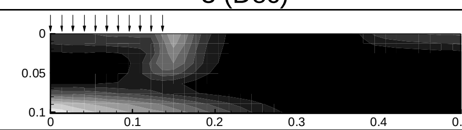 40 (Jan)

[a] Cumulative number of months to failure.

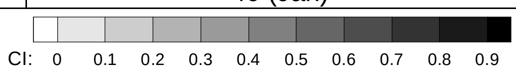

Table 5-4. Parametric Study Simulations for Thick (T) Pavements: Control Mix

Condition	FL	DC	WY
T-C-W	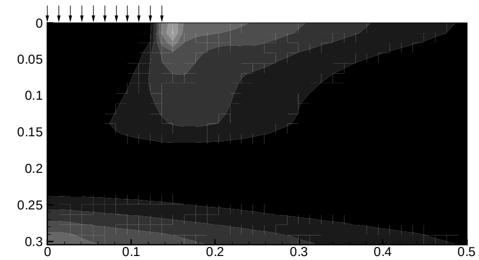	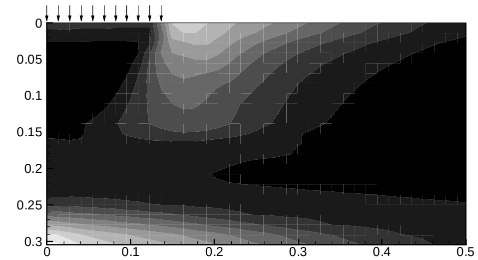	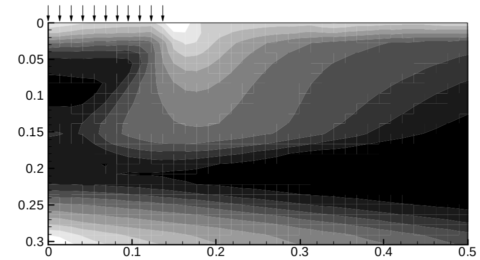
	100 (Jan)	27 (Dec)	26 (Nov)
T-C-M	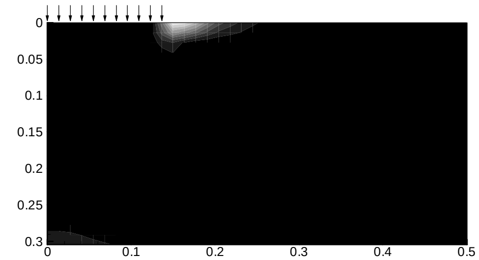	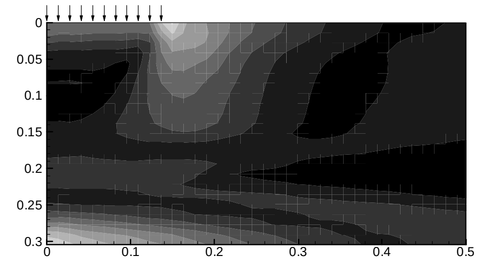	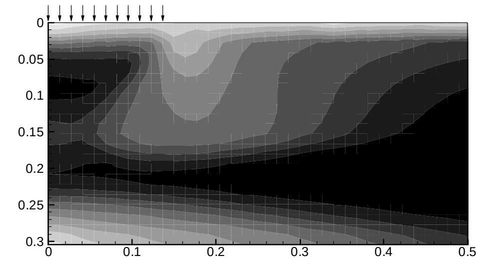
	116 (May)	75 (Dec)	28 (Jan)
T-C-S	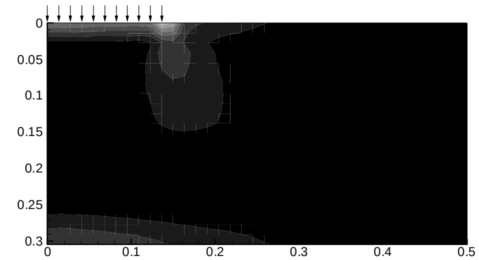	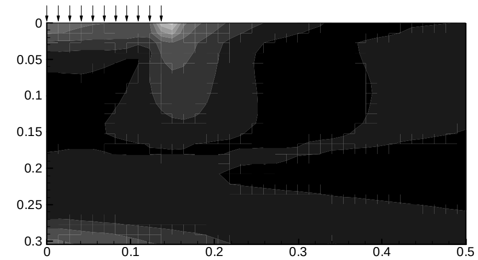	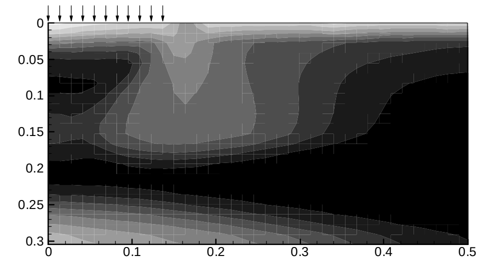
	220 (Jan)	122 (Nov)	28 (Jan)

CI: 0 0.1 0.2 0.3 0.4 0.5 0.6 0.7 0.8 0.9

Table 5-5. Parametric Study Simulations for Thick (T) Pavements: SBS Mix

Condition	FL	DC	WY
T-S-W	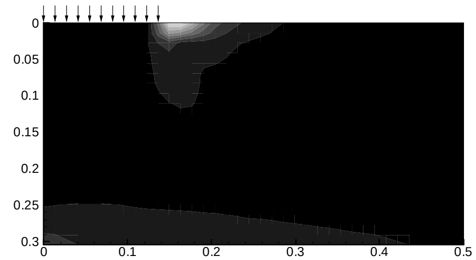	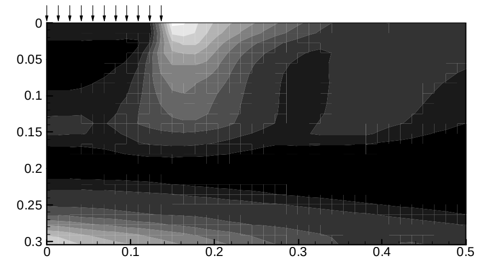	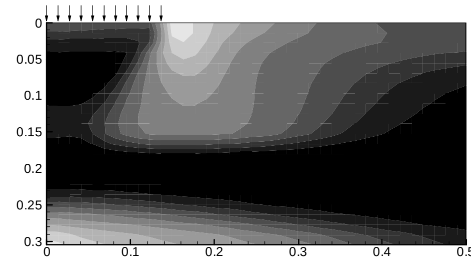
	115 (Apr)	39 (Dec)	26 (Nov)
T-S-M	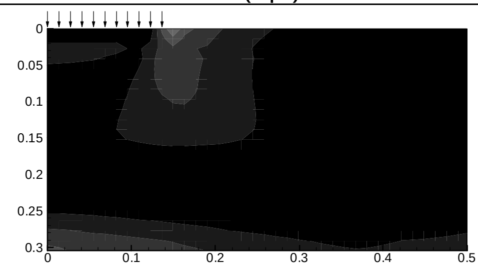	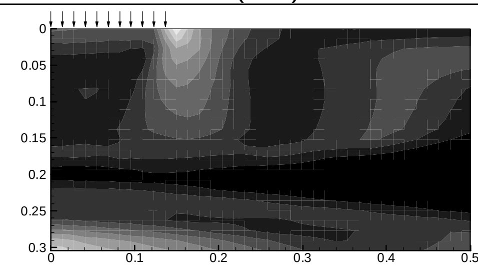	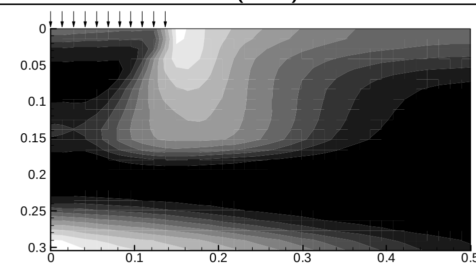
	232 (Jan) – Not Failed	123 (Dec)	38 (Nov)
T-S-S	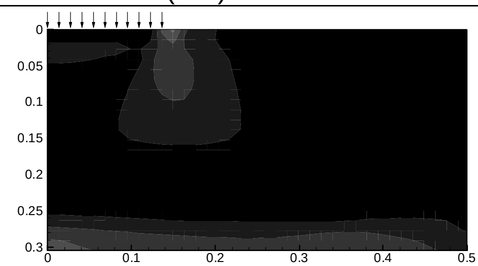	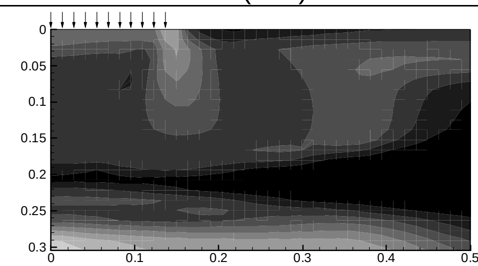	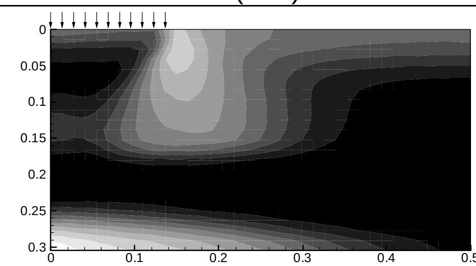
	232 (Jan) – Not Failed	232 (Jan) – Not Failed	38 (Nov)

5.1.2.1 : Effect of Structure

Overall, as shown in Figure 5-1, a thin pavement shows much earlier failure than a thick pavement, even though the amount of traffic for a thin pavement is ten times less than for a thick pavement. This phenomenon could be caused by using the same ESAL loading for both pavements. In general, a thin pavement is used for local roads that tend to serve relatively light vehicles, whereas a thick pavement is used for highways that serve relatively heavy vehicles. For the same magnitude of loading, as can be seen in Table 4-4 to Table 4-6, the stress and strain levels in a thin pavement are much higher than those in a thick pavement, and as a result, the degree of damage produced by one loading is much more severe in a thin pavement than in a thick pavement. Such high stress and strain levels in a thin pavement make the effect of thermal stress relatively small, because thermal stress is not affected too much by the thickness of the AC layer, and as a result, more bottom failure occurs in a thin pavement and more top failure occurs in a thick pavement.

The structural effect does not clearly show any differentiated trend for the interactions with other parameters. From the contour plots at failure, shown in Table 5-3 to Table 5-5, the damage area is narrow for a thin pavement whereas the damage area is wide for a thick pavement.

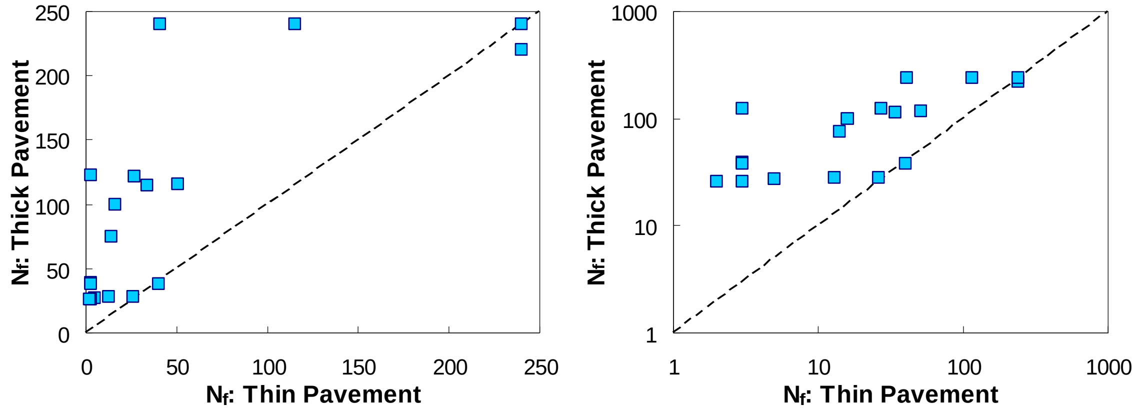

Figure 5-1. Comparison of number of cycles to failure for thin pavements and thick pavements

5.1.2.2 : Effect of Asphalt Mixture Properties

From the thick pavement simulations, it is clear that the SBS material results in much improved performance with regard to the cumulative number of months to failure for all of the sublayer and climate conditions. It also shows that with a strong sublayer and warm climate, the difference in the cumulative number of months to failure between the Control and SBS mixes is large. This difference occurs because the damage in the SBS pavements tends to slow considerably during the summer months due to the overall lower modulus of the SBS mix relative to the Control mix and the tendency of the SBS pavement to exhibit more viscoplastic behavior at high temperatures, and thus, to have a more favorable damage factor than the Control pavement. It is also expected that the difference between them is large if the mix specific healing potential is applied, because based on other research (33), the SBS mix is generally expected to exhibit a more favorable healing potential than the Control mix.

The same basic mechanisms that are active in the thick pavement also apply to the thin pavement, except for the four cases with weak sublayers and cold climates. Those four cases failed in only two to three months, which may be because the soft SBS mix under the worse conditions could not endure the ESAL load during the first winter season.

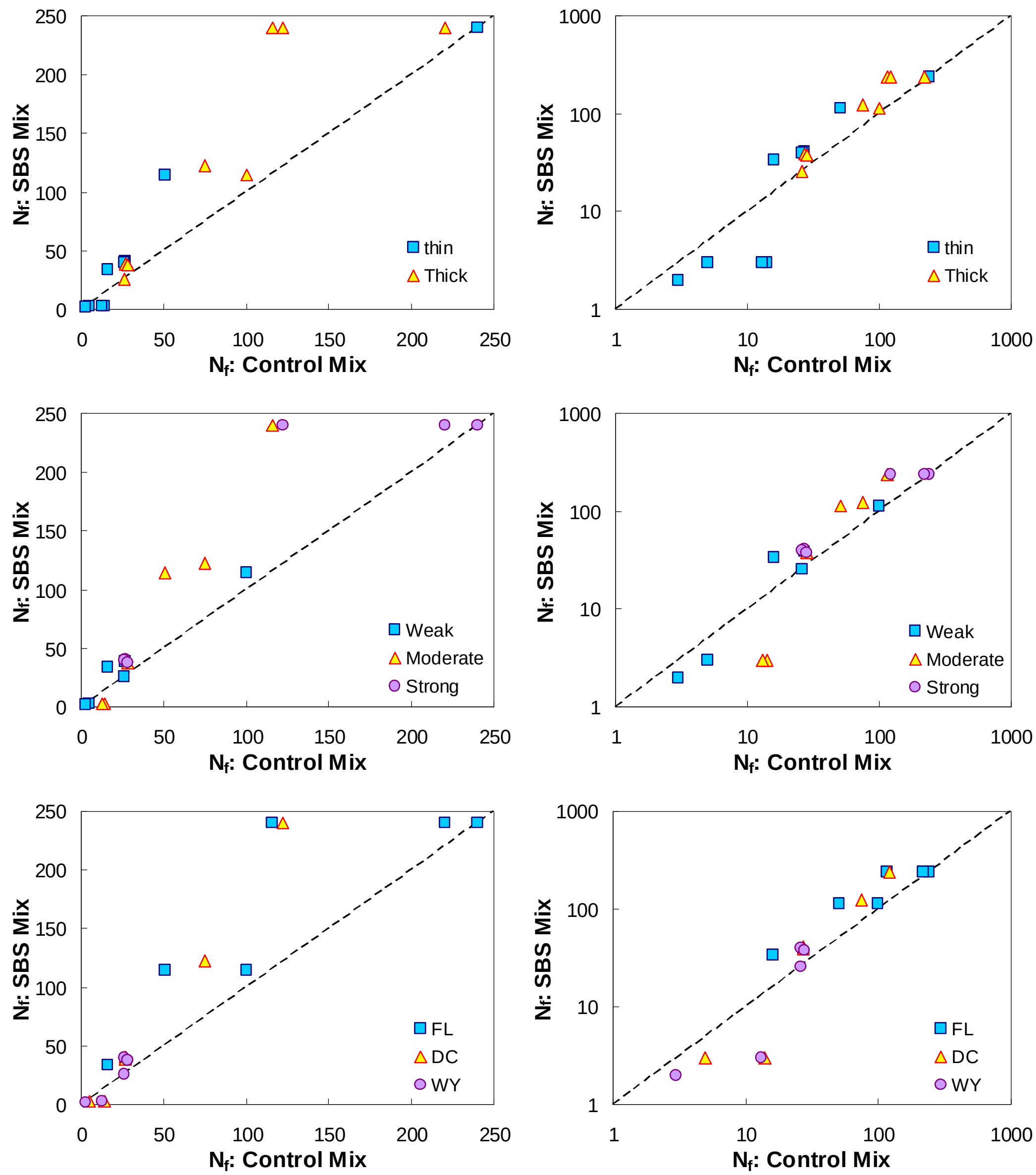

Figure 5-2. Comparison of number of cycles to failure for Control and SBS mixes

5.1.2.3 : Effect of Unbound Layer Property

From Figure 5-3, the effect of the sublayer stiffness clearly indicates, as was expected, that strong sublayers always result in a long pavement life in cases that have the same parameters. This effect is more pronounced in thin pavements than thick pavements. When weak sublayers interact with the soft SBS mix, the damage tends to be significant at the top of thin pavements and results in top failure, as is shown in Table 5-2.

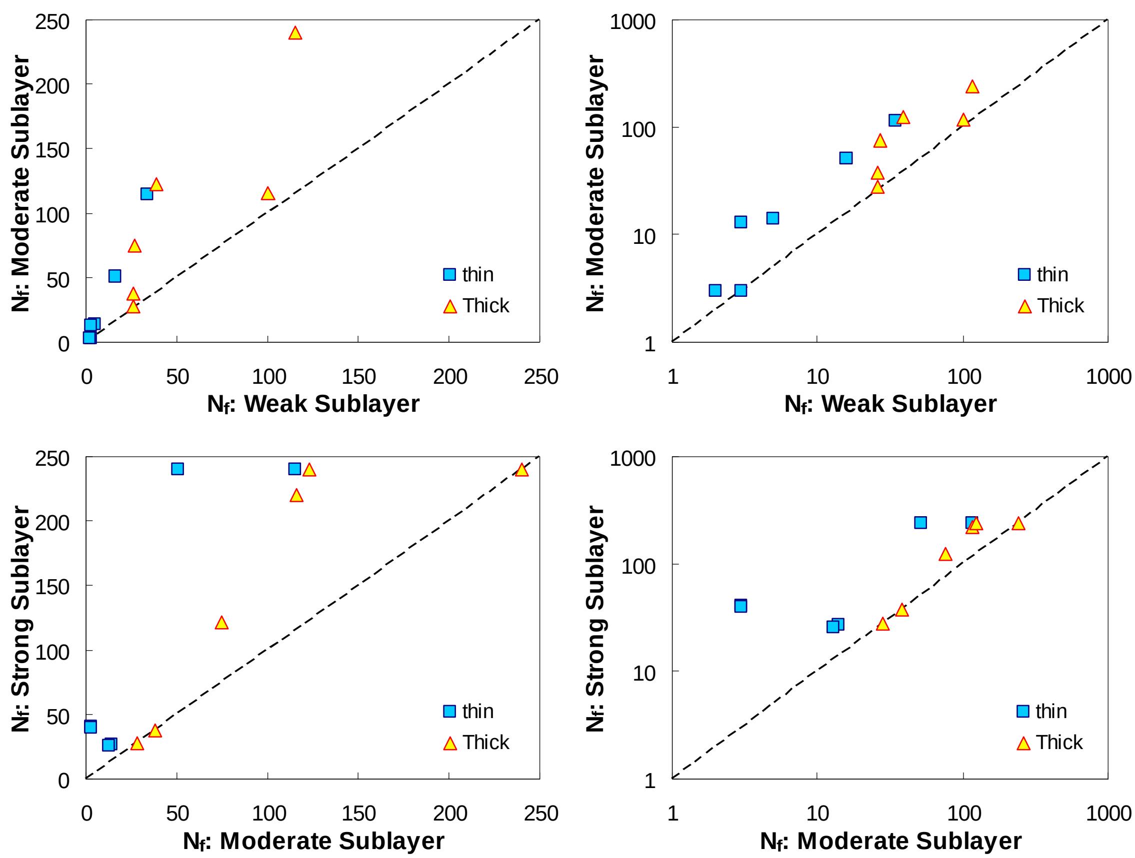

Figure 5-3. Comparison of number of cycles to failure for weak, moderate, and strong sublayers

5.1.2.4 : Effect of Region

As indicated in the contour plots, the colder climates, as compared to warmer climates, tend to show a higher damage distribution at both the top and bottom of both thin and thick pavements. This phenomenon could be due to the relatively stiff PG70-22 binder that is used in the mixtures. Thus, mixtures with these binders are not likely to be used in a climate such as that of Wyoming, and as Figure 5-4 shows, failure occurs much more quickly in cold climates than in warm climates. The key factors that may lead to this early failure are: 1) increased thermal damage potential, 2) decreased healing potential, and 3) a high failure criterion. The results of these factors can intensify due to large temperature variations and due to generally low temperatures. The regional effect does not exhibit any specific trend with regard to the interaction of other parameters.

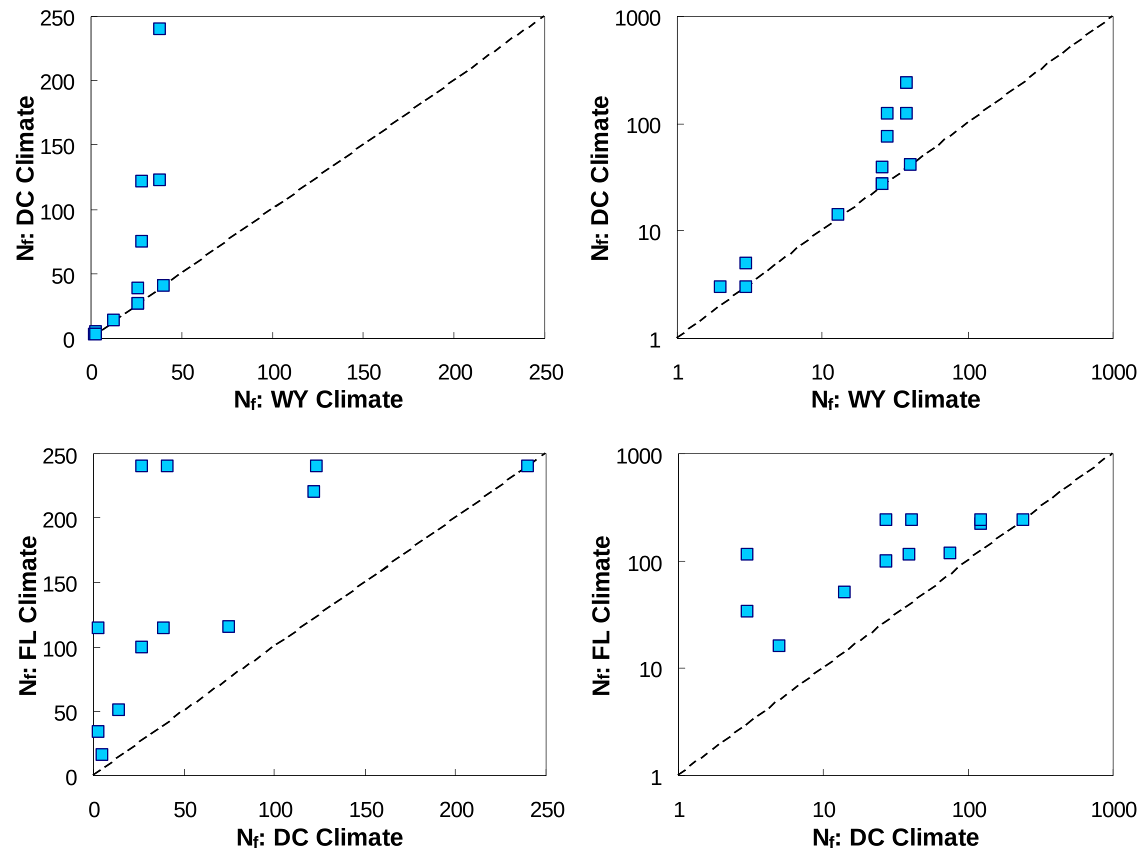

Figure 5-4. Comparison of number of cycles to failure for FL, DC, and WY climates

5.2 : SIMULATION OF FHWA ALF PAVEMENTS

The ultimate evaluation of the VECD-FEP++ is its ability to predict the performance of real pavements that show TDC and to have all of the necessary input parameters available. Currently, no such real pavement exists; instead, in this research, FHWA ALF pavement data are utilized for the model evaluation. In the FHWA ALF research, twelve asphalt pavement lanes (that use various binders) were constructed at the FHWA Turner-Fairbank Highway Research Center to rapidly collect data on pavement performance under conditions in which axle loading and climatic conditions are controlled. The controlled FHWA ALF experiment allows a direct comparison between measured and predicted fatigue performance because all the necessary inputs and field measurements are available.

5.2.1 : FHWA ALF Pavements

The current experiment at the FHWA ALF consists of twelve lanes of unmodified, polymer-modified, air-blown and fiber-reinforced asphalt concrete mixtures. Each lane is large enough to contain four different test sites: two for rutting, one for fatigue, and one currently unassigned. The fatigue tests and rutting tests are performed on both 100 mm and 150 mm test sections, as shown in Figure 5-5 (26). Also from Figure 5-5 it is seen that each asphalt concrete layer rests on top of 560 mm or 510 mm of crushed aggregate base, which, in turn, is on top of an AASHTO A-4 subgrade. For the fatigue tests on the 100 mm thick sections, the pavement is loaded with a 425/64R22.5 (super-single) tire moving at 17 km/hr (10.5 mph), a load of 73.8 kN (16.6 kip), a contact pressure of 827 kPa (120 psi), and a temperature of 19°C (66.2°F). The fatigue test lanes are instrumented using both transverse and longitudinal strain gauges, as illustrated schematically in Figure 5-6. During loading, the percentage of cracked area is measured at regular intervals; the results of these measurements are shown in Figure 5-7. For the purposes of this study, lanes 2, 4, 5, and 6 are of primary importance because the materials for these lanes have been characterized for all the parameters necessary to run the VECD-FEP++ model, as shown in Figure 5-8.

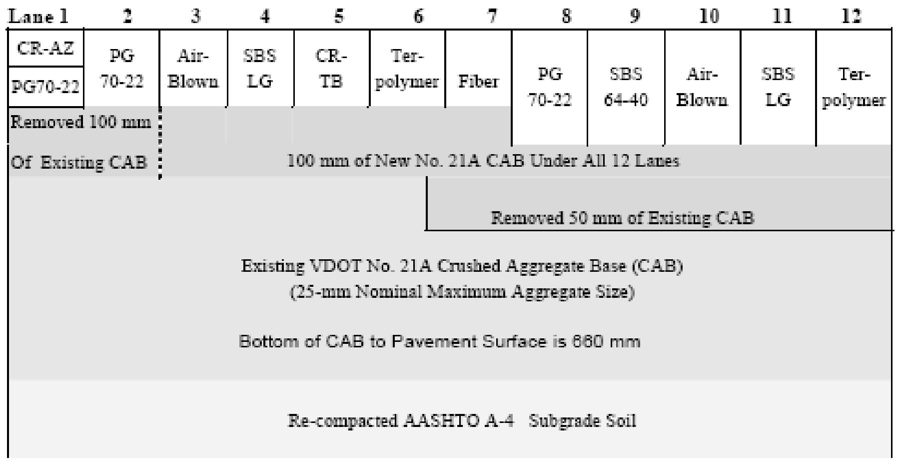

Lane 1: CR-AZ = Crumb Rubber Asphalt Binder, Arizona DOT Wet Process
Lane 2 & 8: PG 70-22 = Unmodified Asphalt Binder Control (Intermediate Grade Temperature T_{IS} = 26.1°C)
Lane 3 & 10: Air-Blown = Air-Blown Asphalt Binder (T_{IS} = 22.6°C)
Lane 4 & 11: SBS LG = Styrene-Butadiene-Styrene Modified Asphalt Binder with Linear Grafting (T_{IS} = 18.1°C)
Lane 5: CR-TB = Crumb Rubber Asphalt Binder, Terminal Blend (T_{IS} =17.9°C)
Lane 6 & 12: Terpolymer = Ethylene Terpolymer Modified Asphalt Binder (T_{IS} = 14.3°C)
Lane 7: Fiber = Unmodified PG 70-22 Asphalt Binder with 0.2 Percent Polyester Fiber by Mass of the Aggregate.
Lane 9: SBS 64-40 = Styrene-Butadiene-Styrene Modified Asphalt Binder Graded PG 64-40 (T_{IS} =8.6°C)

Figure 2. Layout and cross-section of the 12 as-built pavement lanes.

Figure 5-5. FHWA ALF layout and cross-section of the 12 as-built pavement lanes (Qi et al. [26])

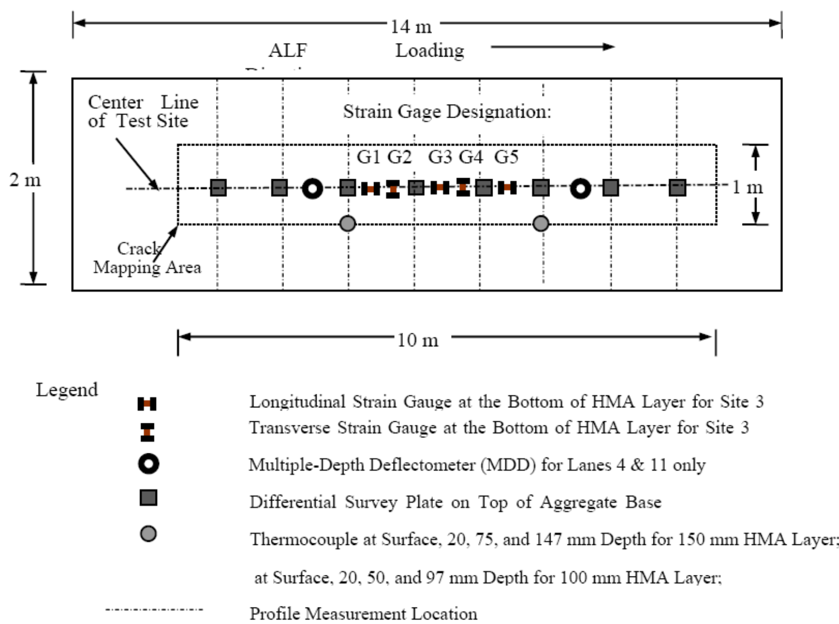

Figure 5-6. Instrumentation for fatigue test sections (Qi et al. [26])

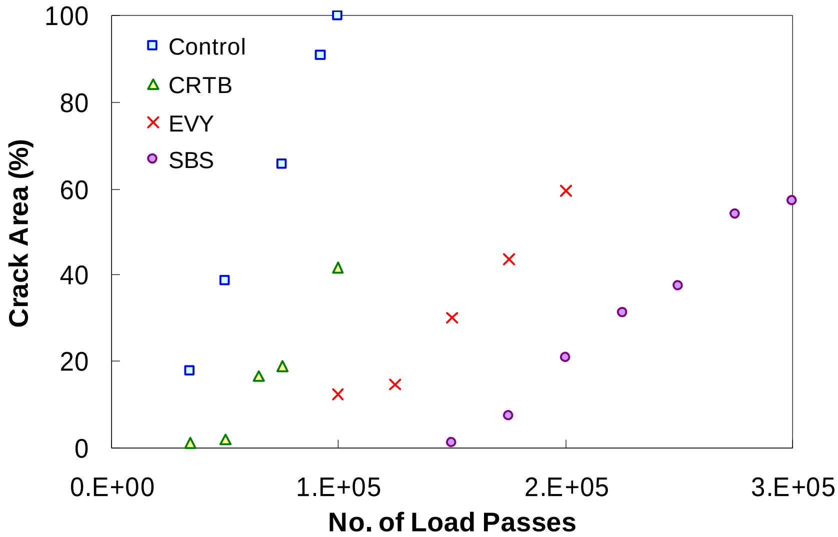

Figure 5-7. Crack area as a function of load passes in ALF experiment

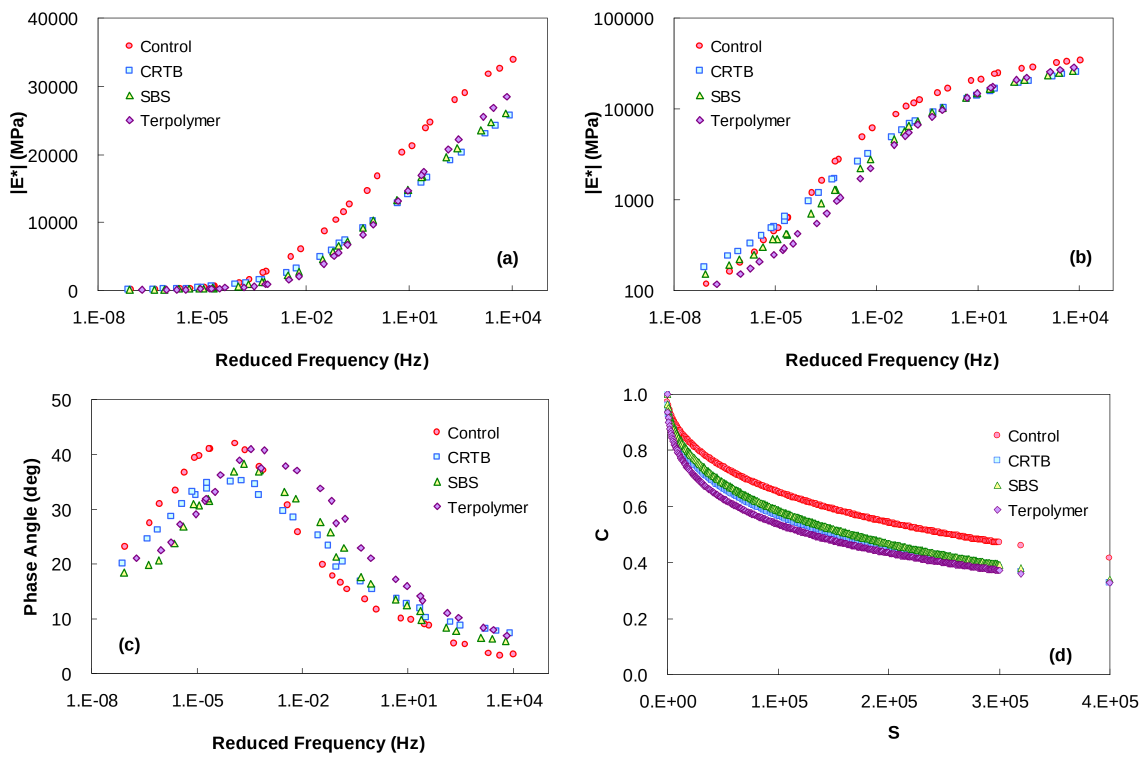

Figure 5-8. VECD characterization of FHWA ALF mixtures: (a) |*E| in semi-log space, (b) |*E**| in log-log space, (c) phase angle, and (d) damage characteristic curves**

The modulus values of the base and subgrade layers were determined via backcalculation from falling weight deflectometer (FWD) tests performed on the surface of the base layer at different load levels and locations for each test site. Table 5-6 summarizes the lane-specific modulus values for each lane and the averaged modulus values of all four lanes. During the backcalculation process, it was found that the variation in modulus values is somewhat large even within the same lane. Therefore, both lane-specific modulus values and average modulus values were utilized for the ALF simulation, and then each result was compared with the field measurement.

Table 5-6. Backcalculated Modulus Values of Base and Subgrade Layers for ALF Pavements

ALF Lane	Mixture	Backcalculated Modulus, MPa (ksi)	
		Base	Subgrade
2	Control	160.0 (23.2)	46.0 (6.7)
4	SBS	132.0 (19.1)	42.0 (6.1)
5	CRTB	105.0 (15.2)	37.0 (5.4)
6	Terpolymer	108.0 (15.7)	36.0 (5.2)
Average		126.3 (18.3)	40.3 (5.9)

5.2.2 : Simulation Details

A series of VECD-FEP++ simulations using ALF pavement inputs was performed to investigate how each sub-model affects the fatigue performance. Four sets of simulations were run with: 1) only mechanical loading, 2) mechanical loading and healing, 3) mechanical loading and damage factor, and 4) mechanical loading and damage factor and healing. The aging model and thermal model were not included because the ALF experiments were conducted within a fairly short period and the temperature was constant at 19°C. Extrapolation of 1,000 cycles which was determined by conducting a simple sensitivity simulation was applied after each single loading. All simulations were run until the C of any element reached 0.25, which is defined as the failure point for the ALF simulation.

Simulation conditions, such as structure, load amplitude, and temperature, were the same for the ALF experiments, except for the moving load. To simulate the moving load, 0.6 second of haversine loading followed by 10.4 second of rest period were applied. The loading time and rest period were determined based on the strain responses from the ALF measurements and from the three-dimensional FEP++ simulation that uses the ALF moving load (38).

5.2.3 : Simulation Results and Comparison with Field Data

The number of cycles to failure (N_f) for all simulations is summarized in Table 5-7. Example damage contour plots at the failure are shown in Table 5-8 for the case in which all three sub-models are included and average sublayer modulus values are used. From these results, several observations can be made regarding the effect of each factor and overall trend:

- The damage factor significantly improves the fatigue performance for all cases. This effect could be due to the relatively long loading times and weak sublayer moduli (comparing to those in Table 4-2). Both conditions can make the pavement more sensitive to structural and material viscoplastic effects.

- Healing is not dominant, mainly due to the moderate temperature.
- The inclusion of sub-models does not change overall rankings, which could be due to; 1) structural viscoplastic effect is more dominant than material viscoplastic effect and thus, the damage factors for each asphalt mix are similar and 2) applying the same healing potential to all mixes. For instance, it is known that the SBS-modified mix has more healing potential than the unmodified mix (33).
- Sublayer moduli can change the pavement performance ranking, as seen in, for example, the Control versus CRTB mixes. In addition, relatively small differences in sublayer moduli can more than double the pavement life.
- It should be noted that all simulations failed at the bottom of the AC layer, even though some damage occurred at the top as well. Such bottom-up cracking could be expected for thin pavements under the moderate temperature condition and, in fact, the ALF findings reported that all fatigue lanes showed bottom-up cracking (26).

Table 5-7. Number of Cycles to Failure from VECD-FEP++ Simulations for ALF Pavements

Lane	Mix	Lane-specific Sublayer				Average Sublayer			
		M[a]	M+H[b]	M+D[c]	M+D+H	M	M+H	M+D	M+D+H
2	Control	20,000	22,000	48,000	52,000	9,000	11,000	23,000	25,000
5	CRTB	7,000	7,000	30,000	32,000	13,000	14,000	70,000	75,000
4	SBS	35,000	38,000	167,000	185,000	29,000	31,000	135,000	149,000
6	Terpolymer	64,000	70,000	256,000	292,000	134,000	148,000	540,000	652,000

[a] Mechanical loading: [b] Healing: [c] Damage factor

Table 5-8. Damage Contours of ALF Pavements using Average Sublayer Modulus Values

Mixture	Damage Contours at Failure	N_f
Control	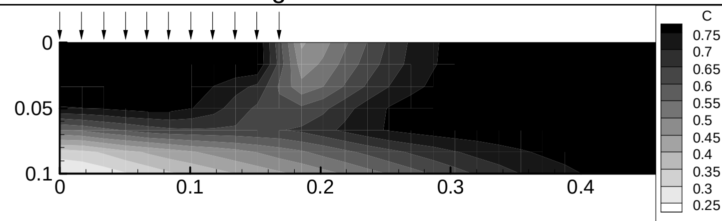	25,000
CRTB	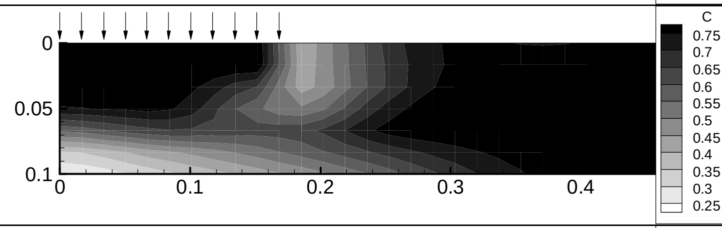	75,000
SBS	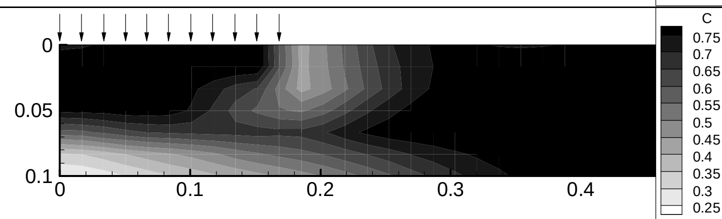	149,000
Terpolymer	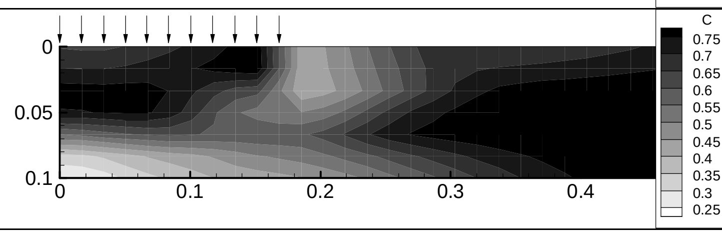	652,000

Comparisons of the fatigue performance results between the ALF measurements and VECD-FEP++ simulations are shown in Figure 5-9. Failure in the ALF experiments is defined as the cycle at which 20% of the lane has cracked, based on the results of Kutay et al. (17). Additionally, Kutay et al. noted that certain problems relating to the distribution of hydrated lime throughout the Terpolymer test lane may have affected the ALF test results. Therefore, two comparisons are shown in Figure 5-9: one that includes Terpolymer and one that does not include Terpolymer. Note that the comparisons are drawn using the predictions of the VECD-FEP++ simulation that includes the damage factor and healing. It was found that the comparison by predictions without the damage factor and/or healing shows the same trend.

Overall, in a comparison of field measurements, the prediction that uses lane-specific sublayer modulus values is worse than the prediction that uses average sublayer modulus values. This result is somewhat unexpected because lane-specific sublayer moduli are considered to be similar to those found under actual field conditions. However, given that the variation in the backcalculated moduli was fairly large, even within each lane, using the average moduli may be more appropriate for this simulation because the sublayer modulus values seem to be sensitive in predicting the pavement life and even the ranking. Figure 5-9 (a) shows that the predictions do not match well with the measurements, regardless of whether Terpolymer is included. However, from Figure 5-9 (b), it is clearly seen that if Terpolymer is not included, the comparison is much better.

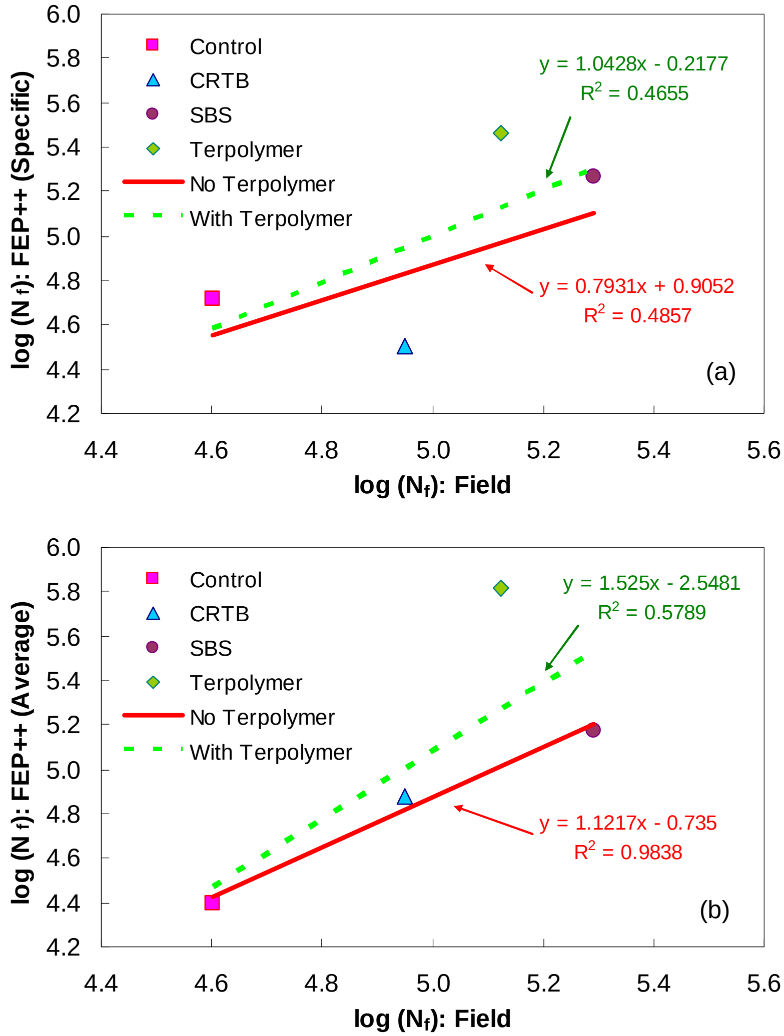

Figure 5-9. Comparisons of cycles to failure between ALF measurements and VECD-FEP++ predictions with damage factor and healing for: (a) lane-specific sublayer modulus values and (b) average sublayer modulus values

Underwood et al. (38) developed a simplified modeling scheme for predicting the ALF pavement fatigue performance. In short, this scheme takes advantage of the three-dimensional FEP++ that is capable of predicting the viscoelastic response under a moving load. Then, the viscoelastic response, which is the tensile strain at the bottom of the AC layer, becomes an input for the simplified VECD model to predict the fatigue performance. In this approach, all conditions and input parameters, except the moving load, are the same as those of the VECD-FEP++ simulation, but the Underwood approach does not include any viscoplastic effects and healing. Note that the Underwood approach utilizes the lane-specific sublayer modulus values.

The results of this simplified model are compared with the ALF field measurements, as shown in Figure 5-10. It can be seen that the simplified model predictions are similar to the VECD-FEP++ predictions that use the average sublayer modulus values, even though the magnitude is different.

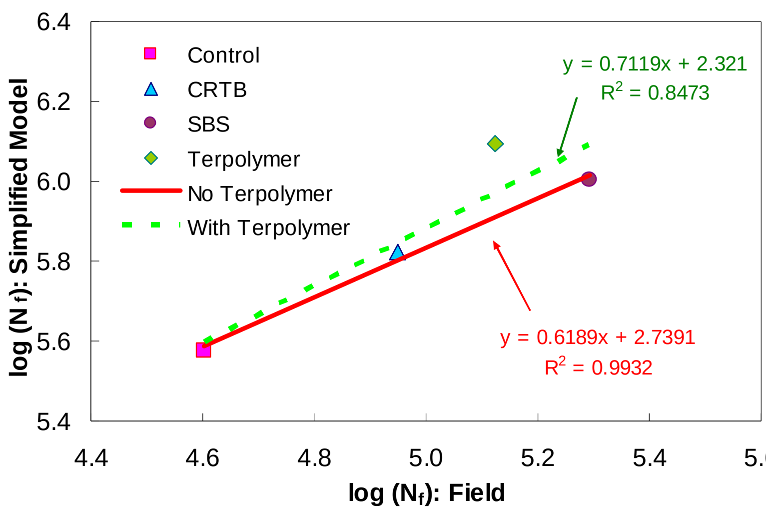

Figure 5-10. Comparison of number of cycles to failure between ALF measurements and simplified model predictions

Therefore, comparisons were made between the VECD-FEP++ predictions and the simplified model predictions, as shown in Figure 5-11. It was found that the VECD-FEP++

prediction that uses the average sublayer modulus values agrees very well with the simplified model prediction that uses the lane-specific sublayer modulus values, even including the Terpolymer pavement. It should be noted that the simplified model scheme applies the initial strain inputs over the entire pavement life so that the different sublayers affect only the initial strains. On the other hand, in the VECD-FEP++ model, the different sublayers play an important role in overall pavement life by affecting the stress and strain redistribution for each time-step.

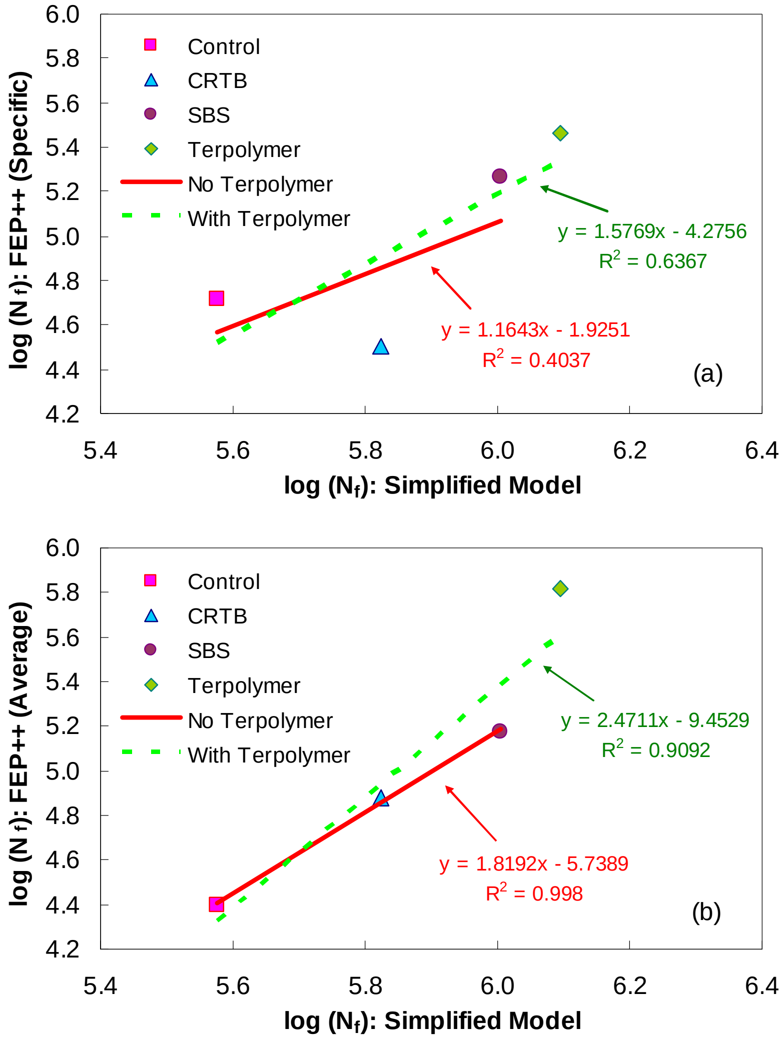

Figure 5-11. Comparison of number of cycles to failure between the simplified model predictions and VECD-FEP++ predictions using: (a) lane-specific sublayer modulus values and (b) average sublayer modulus values

6. CONCLUSIONS AND RECOMMENDATIONS FOR FUTURE RESEARCH

6.1 : CONCLUSIONS

An enhanced VECD-FEP++ model for predicting the TDC in HMA layers has been established in this research. This effort was accomplished by developing, modifying, and/or investigating several important material property models, such as an aging model, healing model, failure criteria, viscoplasticity, and thermal stress, and then finally incorporating these sub-models into the existing VECD model. The material models were converted to and/or combined with the structural models. These sub-models were implemented into the VECD-FEP++, and an extrapolation method for TDC prediction was developed.

Reasonableness and sensitivity studies were undertaken to verify that the framework development and implementation into the VECD-FEP++ were performed correctly. A sensitivity study to investigate the effect of each sub-model on pavement performance reveals that each sub-model affects pavement performance in different ways and to varying degrees. To demonstrate the full capabilities of the VECD-FEP++, two example simulations were carried out, and the results indicate that the interactions among the sub-models and overall trends in terms of pavement behavior were captured successfully.

A systematic evaluation using the VECD-FEP++ was carried out to gain insight into the parameters most responsible for the development and/or dominance of TDC. In general, more damage at both the top and bottom of the pavement was observed in the case of a cold climate, thin structure, weak support layer, and the use of the Control mixture. It was also found that thin pavements tend to fail at the bottom of the pavement, whereas thick pavements tend to show a higher concentration of damage at the top of the pavement and eventually turn in the TDC.

FHWA ALF pavements were predicted and the fatigue performance was compared against the field measurements and the simplified model scheme prediction that was done by other researcher. It was found that VECD-FEP++ captured the overall trend established from field and/or the simplified model scheme.

It should also be noted that the material property sub-models developed for each of the two models should be regarded as place-holders only. Further development and evaluation of the material property place-holder relationships are highly recommended for future work, particularly for models developed to predict fracture energy, damage rate, damage characteristic curves, healing potential and aging.

6.2 : RECOMMENDATIONS FOR FUTURE RESEARCH

Further developments associated with VECD-FEP++ model are summarized as follows.

- The relationship between the laboratory aging method and field aging: The laboratory aging method used for this research follows the SHRP method whose aging levels roughly match those of field aging. However, such a relationship may be heavily dependent on material type, environmental conditions, traffic conditions, pavement structure, etc. In addition, the extent to which the laboratory aging levels used in this research age the asphalt mixtures has not yet been proven.

- Healing model: A simplified version of the phenomenological-mechanical healing model was used in this research; hence, an empirical adjustment has been made to improve the engineering reasonableness. This model should be characterized and verified using data under various conditions that are needed for the FEP++ simulations.
- Advanced material models using the FEP++: Currently, the FEP++ code includes modules for linear elastic unbound paving materials. For more accurate predictions, enhancements are needed to: include a nonlinear elastic material model, consider the effects of moisture gradients in pavement systems, and incorporate anisotropy of the HMA and slip elements at the pavement/base interface.
- Refinement of analysis program: The current VECD modeling is aided by a research grade software package that is still in the development stage. The VECD-FEP++, therefore, cannot be used for rapid pavement assessment due mainly to the many variables (sub-models) that have been incorporated into the analysis framework. However, these sub-models have not been implemented for complexity's sake; rather, after thorough review and improved understanding of the TDC phenomenon, it was determined that these models are necessary. As many studies have reported, TDC appears in various patterns and occurs in various conditions due to various causes. This finding is in opposition to the phenomenon of bottom-up cracking, which is more easily understood and, as a result, can be predicted using simpler means by considering the tensile strain at the bottom of the asphalt layer. Currently, it is impossible to simplify the mechanism to predict TDC by selecting universally

applicable critical scenarios (e.g., the tire edge at the surface, pavement thickness, climatic region, traffic loading, thermal loading, asphalt materials, other pavement materials, etc.). This complexity arises because it is found that the TDC phenomenon is sensitive to all of these properties. It is believed that the approach taken in this research, wherein all of these sub-models are included in the analysis framework, is the most appropriate course of action. It is also expected that through the improvement, refinement, and calibration of these sub-models, the required time to reliably predict TDC will be significantly reduced.

- Model calibration and/or validation using field data: In this research, the simulations were performed using simplified pavement structures. In the field, however, it is unlikely that the pavement structure has the same asphalt mix in the entire bound layer – especially for the thick pavement. The VECD-FEP++ is generic enough that different layers can contain different AC materials. However, it is expect that some modifications may be necessary to the structural aging model and healing and damage factors. Additionally, constant ESAL loading distribution was used in this research. It would be more realistic to use an equivalent daily loading history that has a more representative load spectra and distribution (i.e., more trucks during certain times of the day). As mentioned in the Introduction, the KEC test road would be a good candidate for the validation of the enhanced VECD-FEP++ because the KEC test road consists of various pavement structures subjected to real conditions, and all measured field data, such as traffic, climatic, and performance data, are available.

REFERENCES

1. American Association of State Highway Transportation Officials. *AASHTO Guide for Design of Pavement Structures*. AASHTO, Washington, D.C., 1993.
2. American Association of State Highway Transportation Officials. *AASHTO R30 – 02: Standard Practice for Mixture Conditioning of Hot-Mix Asphalt (HMA)*. AASHTO, Washington, D.C., 2008.
3. Bell, C. A., A. J. Wieder, and M. J. Fellin. *Laboratory Aging of Asphalt-Aggregate Mixtures: Field Validation*. SHRP-A-390, Strategic Highway Research Program. National Research Council, Washington, D.C., 1994.
4. Brown, E. R., R. Collins, J. R. Brownfield. Investigation of Segregation of Asphalt Mixtures in the State of Georgia. In *Transportation Research Record: Journal of the Transportation Research Board*, No. 1217, Transportation Research Board of the National Academies, Washington, D.C., 1989, pp. 1-8.
5. Chehab, G. R., Y. R. Kim, R. A. Schapery, M. Witczack, and R. Bonaquist. Characterization of Asphalt Concrete in Uniaxial Tension Using a Viscoelastoplastic Model. *Journal of the Association of Asphalt Paving Technologists*, AAPT, Vol. 72, 2003, pp. 315-355.
6. Chehab, G. R. and Y. R. Kim. Viscoelastoplastic Continuum Damage Model Application to Thermal Cracking of Asphalt Concrete. *ASCE Journal of Materials in Civil Engineering*, Vol. 17, No. 4, 2003, pp. 384-392.

7. Daniel, J. S. and Y. R. Kim. Laboratory Evaluation of Fatigue Damage Growth and Healing of Asphalt Concrete Mixtures Using the Impact Resonance Method. *ASCE Journal of Materials in Civil Engineering*, Vol. 13, No. 6, 2001, pp. 434-440.
8. Freitas, E. F., P. Pereira, and L. Picado-Santos. Assessment of Top-Down Cracking Causes in Asphalt Pavements. *Proceedings*, 3rd International Symposium on Maintenance and Rehabilitation of Pavements and Technological Control, Guimarães, Portugal, 2003, pp. 555-564.
9. Freitas, E. F., P. Pereira, L. Picado-Santos, and A. T. Papagiannakis. Effect of Construction Quality, Temperature, and Rutting on Initiation of Top-Down Cracking. In *Transportation Research Record: Journal of the Transportation Research Board*, No. 1929, Transportation Research Board of the National Academies, Washington, D.C., 2005, pp. 174-182.
10. Guddati, M. N., S. Savadatti, and S. Thirunavukkarasu. *FEP++: An Object Oriented Finite Element Program in C++ for Nonlinear Dynamic Analysis*. North Carolina State University / University of Texas at Austin, 1995- current.
11. Hinterhoelzl, R. M. and R. A. Schapery. FEM Implementation of a Three-Dimensional Viscoelastic Constitutive Model for Particulate Composites with Damage Growth. *Mechanics of Time Dependent Materials*, Vol. 8, 2004, pp. 65-94.
12. Hou, T., B. S. Underwood, and Y. R. Kim. Fatigue Performance Prediction of North Carolina Mixtures Using the Simplified Viscoelastic Continuum Damage Model. *Journal of the Association of Asphalt Paving Technologists*, AAPT, Vol. 77, 2010, In press.

13. Houston, W. M., M. W. Mirza, C. E. Zapata, and S. Raghavendra. *Environmental Effects in Pavement Mix and Structural Design Systems.* NCHRP 9-23 Project, National Cooperative Highway Research Program. National Research Council, Washington, D.C., 2005.

14. Kim, Y. R., D. N. Little and R. L. Lytton. Use of Dynamic Mechanical Analysis (DMA) to Evaluate the Fatigue and Healing Potential of Asphalt Binders in Sand Asphalt Mixtures. *Journal of the Association of Asphalt Paving Technologists*, AAPT, Vol. 71, 2002, pp. 176-206.

15. Kim, Y. R., D. N. Little, and R. L. Lytton. Fatigue and Healing Characterization of Asphalt Mixtures. *ASCE Journal of Materials in Civil Engineering*, Vol. 15, No.1, 2003, pp. 75-83.

16. Kim, Y. R., C. Baek, B. S. Underwood, V. Subramanian, M. N. Guddati, and K. Lee. Application of Viscoelastic Continuum Damage Model Based Finite Element Analysis to Predict the Fatigue Performance of Asphalt Pavements. KSCE, *Journal of Civil Engineering,* Vol. 12, No. 2, 2008, pp. 109-120.

17. Kutay, M. E., N. Gibson, and J. Youtcheff. Conventional and Viscoelastic Continuum Damage (VECD) - Based Fatigue Analysis of Polymer Modified Asphalt Pavements. *Journal of the Association of Asphalt Paving Technologists,* AAPT, Vol. 77, 2008, pp. 395-434.

18. Lee, H. J. and Y. R. Kim. A Viscoelastic Continuum Damage Model of Asphalt Concrete with Healing. *ASCE Journal of Engineering Mechanics,* Vol. 124, No. 11, 1998, pp. 1224-1232.

19. Lytton, R. L., J. Uzan, E. G. Fernando, R. Roque, D. Hiltumen, and S. M. Stoffels. *Development and Validation of Performance Prediction Models and Specifications for Asphalt Binders and Paving Mixes.* SHRP-A-357, Strategic Highway Research Program, National Research Council, Washington, D.C., 1993.

20. Matsuno, S. and T. Nishizawa. Mechanism of Longitudinal Surface Cracking in Asphalt Pavement. *Proceedings*, 7th International Conference on the Structural Design of Asphalt Pavements, 1992.

21. Meyers, L. A., R. Roque, and B. E. Ruth. Mechanisms of Surface-Initiated Longitudinal Wheel Path Cracks in High-Type Bituminous Pavements. *Journal of the Association of Asphalt Paving Technologists*, AAPT, Vol. 67, 1998, pp. 401-432.

22. Myers, L. N. *Development and Propagation of Surface Initiated Longitudinal Wheel Path Cracks in Flexible Highway Pavements*. Ph.D. dissertation, University of Florida, FL., 2000.

23. Mirza, M. W. and M. W. Witczak. Development of a Global Aging System for Short and Long Term Aging of Asphalt Cements. *Journal of the Association of Asphalt Paving Technologists*, AAPT, Vol. 64, 1995, pp. 393-430.

24. Nesnas, K. and M. Nunn. A Model for Top-down Reflection Cracking in Composite Pavements. *Proceedings,* 5th International RILEM Conference, 2004.

25. Park, S. W. and R. A. Schapery. Methods of Interconversion between Linear Viscoelastic Material Functions. Part I – A Numerical Method based on Prony Series. *International Journal of Solids and Structures*, Vol. 36, 1999, pp. 1653-1657.

26. Qi, N. Gibson and J. Youtcheff. Strain Responses and Fatigue Performances from the FHWA ALF Modified Binder Pavements. *Advanced Characterization of Pavement and Soil Engineering Materials: Proceedings of the International Conference on Advanced Characterization of Pavement and Soil Engineering*. Athens, Greece, 2007.

27. Raghavendra, S., C. E. Zapata, M. W. Mirza, W. N. Houston, and M. W. Witczak. Verification of the Rate of Asphalt Mix Aging Simulated by AASHTO PP2-99 Protocol. CD-ROM. Transportation Research Board of the National Academies, Washington, D.C., 2006.

28. Reese, R. Properties of Aged Asphalt Binder Related to Asphalt Concrete Fatigue Life. *Journal of the Association of Asphalt Paving Technologists*, AAPT, Vol. 66, 1997, pp. 604-632.

29. Schapery, R. A. *A Simple Collocation Method for Fitting Viscoelastic Models to Experimental Data.* GALCIT SM 61-23A. California Institute of Technology, Pasadena, CA., 1961.

30. Schapery, R. A. Correspondence Principles and a Generalized J-integral for Large Deformation and Fracture Analysis of Viscoelastic Media. *International Journal of Fracture*, Vol. 25, 1984, pp. 195-223.

31. Schapery, R. A. Nonlinear Viscoelastic and Viscoplastic Constitutive Equations with Growing Damage. *International Journal of Fracture*, Vol. 97, 1999, pp. 33-66.

32. Schorsch, M., C. Chang, and G. Y. Baladi. Effects of Segregation on the Initiation and Propagation of Top-Down Cracks. CD-ROM. Transportation Research Board of the National Academies, Washington, D.C., 2003.

33. Shen, S., H. Chiu, and H. Huang. Fatigue and Healing in Asphalt Binders. CD-ROM. Transportation Research Board of the National Academies, Washington, D.C., 2009.

34. Svasdisant, T., M. Schorsch, G. Y. Baladi, and S. Pinyosunun. Mechanistic Analysis of Top-Down Cracks in Asphalt Pavements. In *Transportation Research Record: Journal of the Transportation Research Board*, No. 1809, Transportation Research Board of the National Academies, Washington, D.C., 2002, pp. 126-136.

35. Thirunavukkarasu, S. *Performance Prediction Module*. Internal Report, North Carolina State University, NC., 2009.

36. Underwood, B. S., Y. R. Kim and M. N. Guddati. Characterization and Performance Prediction of ALF Mixtures Using a Viscoelastoplastic Continuum Damage Model. *Journal of the Association of Asphalt Paving Technologists,* AAPT, Vol. 75, 2006, pp. 577-636.

37. Underwood, B. S. and Y. R. Kim. Determination of the Appropriate Representative Elastic Modulus for Asphalt Concrete. *International Journal of Pavement Engineering,* Vol. 10, No. 2, 2009, pp. 77-86.

38. Underwood, B. S., Y. R. Kim, S. Savadatti, S. Thirunavukkarasu, and M. N. Guddati. Response and Fatigue Performance Modeling of ALF Pavements Using 3-D Finite Element Analysis and a Simplified Viscoelastic Continuum Damage Model. *Journal of the Association of Asphalt Paving Technologists,* AAPT, Vol. 78, 2009, pp. 743-776.

39. Underwood, B. S. *Simplified Healing Model Development*. Internal Report, North Carolina State University, NC., 2009.

40. Uzan, J., M. Perl, and A. Sides. Viscoelastoplastic Model for Predicting Performance of Asphalt Mixtures. In *Transportation Research Record: Journal of the Transportation Research Board*, No. 1043, Transportation Research Board of the National Academies, Washington, D.C., 1985, pp. 78-79.

41. Uhlmeyer, J. S., K. Willoughby, L. M. Pierce, and J. P. Mahoney. Top-down Cracking in Washington State Asphalt Concrete Wearing Courses. In *Transportation Research Record: Journal of the Transportation Research Board*, No. 1730, Transportation Research Board of the National Academies, Washington, D.C., 2000, pp. 110-116.

42. Wang, L. B., L. A. Myers, L. N. Mohammad, and Y. R. Fu. Micromechanics Study on Top-Down Cracking. In *Transportation Research Record: Journal of the Transportation Research Board*, No. 1853, Transportation Research Board of the -National Academies, Washington, D.C., 2003, pp. 121-133.

43. Wistuba, M., R. Lackner, R. Blab, and M. Spiegl. Low-temperature Performance Prediction of Asphalt Mixtures Used for LLP-New Approach Based on Fundamental Test Methods and Numerical Modeling. *International Journal of Pavement Engineering* 7 (2), 2006, pp. 121–132.